Characterizing Nanomaterials and Protic Ionic Liquids Utilizing Nuclear Magnetic Resonance Spectroscopy

by

Stephen Davidowski

A Dissertation Presented in Partial Fulfillment
of the Requirements for the Degree
Doctor of Philosophy

Approved September 2015 by the
Graduate Supervisory Committee:

Jeffery L. Yarger, Co-Chair
Gregory P. Holland, Co-Chair
C. Austen Angell
Daniel A. Buttry

ARIZONA STATE UNIVERSITY

December 2015

ABSTRACT

Structural details of phosphonic acid functionalized nanomaterials and protic ionic liquids (PILs) were characterized using nuclear magnetic resonance (NMR) spectroscopy. It is well known that ligands play a critical role in the synthesis and properties of nanomaterials. Therefore, elucidating the details of ligand-surface and ligand-ligand interactions is crucial to understanding nanomaterial systems more completely.

In an effort to further the understanding of ligand-surface interactions, a combination of multi-nuclear (^{1}H, ^{29}Si, ^{31}P) and multi-dimensional solid-state NMR techniques were utilized to characterize the phosphonic acid functionalization of fumed silica nanoparticles using methyl phosphonic acid (MPA) and phenyl phosphonic acid (PPA). Quantitative ^{31}P MAS solid-state NMR measurements indicate that ligands favor a monodentate binding mode. Furthermore, ^{1}H-^{1}H single quantum-double quantum (SQ-DQ) back-to-back (BABA) 2D NMR spectra of silica functionalized with MPA and PPA indicate that the MPA and PPA are within 4.2±0.2 Å on the surface of the nanomaterial.

The ligand capping of phosphonic acid (PA) functionalized CdSe/ZnS core-shell quantum dots (QDs) was investigated with a combination of ligand exchange, solution and solid-state ^{31}P NMR spectroscopy. In order to quantify the ligand populations on the surface of the QDs, ligand exchange facilitated by PPA resulted in the displacement of the PAs, and allowed for quantification of the free ligands using ^{31}P liquid state NMR.

In addition to characterizing nanomaterials, the ionicity and transport properties of a series of diethylmethylamine (DEMA) based protic ionic liquids (PILs) were characterized, principally utilizing NMR. Gas phase proton affinity was shown to be a

better predictor for the extent of proton transfer, and in turn the ionicity of the PIL, than using ΔpK_a. Furthermore, pulsed field gradient (PFG) NMR was used to determine that the exchangeable proton diffuses with the cation or the anion based on the strength of the acid used to generate the PILs.

DEDICATION

To my family

To Jason C. Jarkes

ACKNOWLEDGMENTS

First, I would like to thank my advisors Prof. Jeffery Yarger and Prof. Gregory Holland. They have always challenged me to be a better scientist and without their guidance and support none of this work would have been possible. I would also like to acknowledge Professor C. Austen Angell, for his guidance and support on the ionic liquids project. I would also like to acknowledge Brian Cherry, the lab manger in the magnetic resonance research center (MRRC), for all the time he spent helping me learn NMR spectroscopy. Furthermore, I am thankful to my undergraduate research advisor Prof. Cliff J. Timpson for helping ignite my interest in research and for all of his guidance over the years. I am grateful for the support provided by Life Technologies and the supply of quantum dot materials for the ligand exchange project. Further, I would like to thank the National Science Foundation (NSF) for providing funding for the nanoparticle projects with the grants (CHE-1011937 and DMR-1264801). Also, I would like to acknowledge the Army Research Office for their support of the protic ionic liquids project.

Additionally, I would like to thank all of the members of the Yarger research group here at ASU for their scientific discussions, advice, and guidance. Further, I acknowledge specifically the help of Forrest Thompson, Tom Osborn Popp, and Justin Hillsten for their tireless efforts, which contributed to this work.

Finally, I would like to thank my family and friends for all of their moral and emotional support throughout my graduate studies. Without their help this work would not have been possible.

TABLE OF CONTENTS

Page

LIST OF TABLES vii

LIST OF FIGURES viii

CHAPTER

1 SOLID-STATE NMR CHARACTERIZATION OF MIXED PHOSPHONIC ACID LIGAND BINDING AND ORGANIZATION ON SILICA NANOPARTICLES 1

1.1 Introduction 1

1.2 Experimental 4

1.3 Results and Discussion 6

1.4 Conclusions 18

1.5 Supplementary Material 19

1.6 References 21

2 CHARACTERIZING MIXED PHOSPHONIC ACID LIGAND CAPPING ON CdSe/ZnS QUANTUM DOTS USING LIGAND EXCHANGE AND NMR SPECTROSCOPY 28

2.1 Introduction 28

2.2 Experimental 30

2.3 Results and Discussion 33

2.4 Conclusions 39

2.5 References 41

CHAPTER Page

3 NMR CHARACTERIZATION OF IONICITY AND TRANSPORT PROPERTIES FOR A SERIES OF DIETHYLMETHYLAMINE BASED PROTIC IONIC LIQUIDS 46

3.1 Introduction 46

3.2 Experimental 48

3.3 Results and discussion 53

3.4 Conclusions 62

3.5 Supplementary Material 63

3.5 References 65

4 EXPERIMENTAL & COMPUTATIONAL MEASUREMENTS OF MOLECULAR DIFFUSION USING NMR SPECTROSCOPY AND MOLECULAR DYNAMICS SIMULATIONS: A PHYSICAL OR BIOPHYSICAL CHEMISTRY EXPERIMENT 69

4.1 Introduction 69

4.2 Experimental 72

4.3 Results and Discussion 74

4.4 Conclusions 78

4.5 References 80

REFERENCES 82

LIST OF TABLES

Table Page

1.1 Summary of ^{31}P Chemical Shift Assignments for Phosphonic Acids Binding to Silica 12

2.1 Comparison of the Ratios of the Phosphonic Acid Ligands Used to Stabilize the QDs 36

2.2 Ratios of the Ligands Used During the Ligand Exchange Reactions and the Ratios Observed 39

3.1 Results of Diffusion and Conductivity Measurements 60

4.1 Diffusion Coefficients for the Listed Small Molecules Diffusing Through Water Obtained Using MD and PFG-NMR 79

LIST OF FIGURES

Figure Page

1.1 A TEM Image of 7nm Fumed Silica and the Structures of Methyl Phosphonic Acid and Phenyl Phosphonic Acid 4

1.2 $^{1}H \rightarrow ^{29}Si$ CP-MAS Spectra of Fumed Silica and PPA Functionalized Fumed Silica 7

1.3 $^{1}H \rightarrow ^{31}P$ CP-MAS Spectra of Phosphonic Acid Functionalized Fumed Silica....9

1.4 ^{31}P MAS Spectra of Phosphonic Acid Functionalized Fumed Silica 11

1.5 $^{1}H \rightarrow ^{31}P$ HETCOR NMR Spectrum for MPA Functionalized SiO_2 13

1.6 ^{1}H-DEPTH NMR Spectra of Phosphonic Acid Functionalized Fumed Silica 15

1.7 ^{1}H-^{1}H SQ-DQ NMR Spectrum for the MPA:PPA Capped Fumed Silica 17

1.8 ^{31}P MAS NMR Spectrum of SiO_2 Functionalized With Equimolar MPA:PPA Deconvoluted Using DMFit....19

1.9 ^{1}H EXSY NMR Data for 1:1 MPA:PPA Functionalized Fumed Silica 19

1.10 ^{1}H-^{1}H BABA-DQ Spectra of Phosphonic Acid Functionalized Fumed Silica....20

1.11 $^{1}H \rightarrow ^{31}P$ HETCOR NMR Spectrum of 1:1 MPA:PPA Functionalized Silica 20

2.1 TEM Images of the CdSe/ZnS QDs....30

2.2 ^{31}P CP-MAS Solid-State NMR of CdSe/ZnS QDs....34

2.3 Ligand Exchange $^{31}P\{^{1}H\}$ Liquid State NMR of CdSe/ZnS QDs....35

2.4 $^{31}P\{^{1}H\}$ Liquid-State NMR of CdSe/ZnS QDs 37

2.5 ^{31}P Solid-State MAS NMR Spectra for Dried PA Functionalized QDs 38

3.1 ^{1}H NMR Spectra for DEMA Based Ionic Liquids....52

3.2 Exchangeable Proton Chemical Shift as a Function of ΔpK_a 54

Figure Page

3.3 Exchangeable Proton Chemical Shift as a Function of Proton Affinity 55

3.4 ^{15}N NMR Spectra for an Array of DEMA Based Ionic Liquids.....57

3.5 Example Stejskal-Tanner Plot Obtained From PFG-NMR 59

3.6 Summary of the Characterization of the Ionicity of a Subset of the DEMA Based Ionic Liquids 62

3.7 Gas Phase Proton Affinity Values Obtained Via Electronic Structure Calculations Compared to Literature Values.....63

3.8 Plot Relating the Exchangeable Proton Chemical Shift in DEMA and DMI Based PILs to Their Proton Affinities 64

4.1 Schematic Diagrams of the Pulse Sequences Used to Collect PFG-NMR Data ...71

4.2 Molecular Dynamics Trajectory for Acetone Diffusing Through Water 74

4.3 Molecular Dynamics Trajectories for 20 Simulations of Acetone in TIP3P Water.....75

4.4 Average of 20 Molecular Dynamics Trajectories for Each of the Solutes in Water.....76

4.5 ^{1}H NMR Spectrum of the Mixture of Solutes in D_2O 77

4.6 Stejskal-Tanner Plot for the Small Molecules Diffusing Through D_2O 78

Chapter 1

Solid-state NMR Characterization of Mixed Phosphonic Acid Ligand Binding and Organization on Silica Nanoparticles

1.1 Introduction

As the study of nanostructures and their applications continues becoming prevalent and more complex, the need for a further understanding of the nature of surface phenomena in multi-ligand systems is apparent. Most studies involving nanostructures focus on characterizing the inorganic core through the utilization of techniques such as transmission electron microscopy (TEM) and X-ray diffraction (XRD) methods. However, an area of continuing focus has been characterizing the details of the organic ligand environment surrounding these nanostructures.[1-3] Understanding the ligand interactions is crucial because many of the interesting properties of nanomaterials originate from surface phenomena. For example, it is well known that the ligand chemistry at the interface of the nanoparticles influences the size, shape, solubility, and optical properties.[4-6] In one interesting example, it was shown that in two ligand systems phase separation is possible. The phase separation of two types of ligands into domains in self-assembled monolayers (SAMs) on the surface of gold was first observed via scanning tunneling microscopy (STM) over 20 years ago.[7-9] This phase separation of ligands was considered to be enthalpically driven by the ligand-ligand hydrogen bonding and van der Waals' interactions.[8] Shortly after that, similarly ordered domains of ligands in SAMs on the surface of metal nanoparticles were observed, in various patterns and arrangements.[10-15] The formation of striped patterns of ligands on surfaces has been described as an entropically driven process and has been further examined via

simulations.[16-18] The organization of ligands on the surface of nanoparticles, and understanding ligand-ligand interactions is imperative to the rational design of multi-functional nanomaterials with complex ligands and ligand mixtures.

Phosphonic acid ligands have been a focus in a more general sense recently due to their robustness[7-9,19-22] and versatility as a ligand for a range of nanoparticle systems including metal oxides, [1,8,23-29] silica,[10-15,30-35] and semiconductors.[36-40] The phosphonic acid moiety is also routinely used to anchor dye molecules to TiO_2 nanoparticles for solar applications.[41-44] Phosphonic acids have found applications in more complex systems; such as, functionalizing indium doped tin oxide (ITO) to facilitate more evenly dispersed polymer coatings for organic electric systems.[23] Additionally, phosphonic acid head groups attached to alkyl thiols have been used to tether gold nanoparticles to oxide surfaces.[45,46] As the functionalization of nanomaterials continues to become more complex, the need to fully characterize the nature of the ligand environment is imperative to understanding subsequent chemistry, particularly in more challenging multi-ligand systems.

Although phosphonic acid binding to silica was demonstrated over 20 years ago,[30,47] a complete understanding of silica functionalization with phosphonic acids is still lacking.[34,35] While much effort has been put forth in understanding the details of phosphonic acid binding to metal oxides,[1,28,29,48-51] significantly less work has been done studying the specifics of phosphonic acid binding to silica. This is likely due to some reports that phosphonic acids do not readily bind with silica without being treated with a layer of some other metal/oxide first.[48,52] This appears to be true in situations where aqueous solvent systems are used, implying that phosphonic acid binding to silica is more

susceptible to hydrolysis than phosphonic acid binding to other oxides.[35] This difference can be attributed to the fact that that the silica surface has a lower point of zero charge (PZC) than most of the other commonly studied oxides.[53]

Fumed silica nanoparticles are a commercially available nanostructured material generated by the high temperature hydrolysis of $SiCl_4$ in a hydrogen/oxygen flame.[54] The resulting material is a branching structure of silica nanoparticles generated by the fusing of dispersed SiO_2 particles prior to cooling. This process leads to a very high surface area, non-porous amorphous material. Fumed silica nanoparticles have been the focus of many studies about the surface of silica due to the low cost and high surface area,[54-56] and provide a nice model system to develop advanced solid-state NMR methods for elucidating ligand binding and ligand-ligand interactions in multi-ligand systems.

Fumed silica nanoparticles can be functionalized with phosphonic acids using a facile method described here using a non-aqueous solvent system, and is a good model system for understanding the binding of mixed phosphonic acid ligand systems to the surface of oxide nanostructures. In the presented work, one and two dimensional multinuclear, multidimensional solid-state NMR are applied to study the functionalization of fumed silica with methyl phosphonic acid (MPA) and phenyl phosphonic acid (PPA).

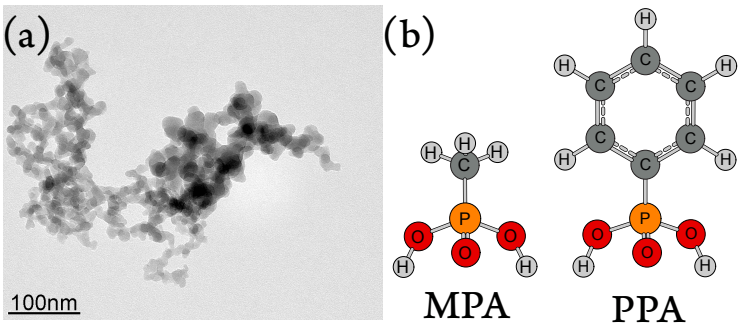

Figure 1.1. A TEM image of 7nm fumed silica (a). The structure of methyl phosphonic acid (MPA) and phenyl phosphonic acid (PPA) (b).

1.2 Experimental

Materials. The fumed silica (7 nm), MPA (98%), PPA (98%) and anhydrous acetonitrile were all purchased from Sigma-Aldrich. The surface area of the obtained fumed silica is reported to be 395±25 m^2/g by the manufacturer. The acetonitrile used in these experiments was freshly distilled from calcium hydride before each synthesis. All other materials were used as received.

Functionalization of fumed silica. In a typical functionalization procedure, a 100 mL round bottom flask was charged with 3 mmoles phosphonic acid in 45 mL of dry acetonitrile under a blanket of nitrogen. This solution was brought to reflux and subsequently a 300 mg sample of 7 nm fumed silica that had been dried at 500 ^oC for 24 hours was added into the flask. This mixture was heated at reflux for 2 hours under a slight flow of nitrogen, after which time it was allowed to cool to room temperature while stirring. The resultant solid was separated from solution via centrifugation, and washed 5 times with 25-mL portions of acetonitrile. This solid was then dried under vacuum for 12 hours at 60 ^oC to remove any excess solvent, and stored in a desiccator or nitrogen glove box until analysis.

Solid-state NMR. Solid-state NMR data was collected with a 400 MHz Varian VNMRS wide-bore spectrometer equipped with a 3.2 mm triple resonance probe operating at 399.74 MHz for ^{1}H, 161.81 MHz for ^{31}P and 79.40 MHz for ^{29}Si. The ^{1}H→^{31}P CP-MAS NMR spectra were collected using a 2.5 μs ^{1}H 90º degree pulse, a 2.5 ms ramped (~10%) ^{1}H spin-lock pulse and a ^{31}P contact pulse with a radio frequency field (rf) strength of 85 kHz, and 10 kHz MAS. The rf field strength of the ^{1}H channel during the contact time was matched to the -1 spinning side band of the ^{1}H→^{31}P Hartmann-Hahn profile (75 kHz). ^{1}H→^{31}P CP-MAS spectra were collected with a recycle delay of 2 seconds and 8k scans for functionalized silica samples and with a 30 to 120 second recycle delay and 16 scans for the pure ligands. The 2D ^{1}H→^{31}P heteronuclear correlation (HETCOR) NMR spectra were collected using similar CP conditions to the CP-MAS spectra, except due to the faster spinning speed of 20 kHz the ^{1}H spin-lock pulse had an rf strength of 65 kHz. Furthermore, HETCOR NMR spectra were collected with a 20 kHz sweep width and 64 complex points in the indirect dimension, 512 scans per point, and 20 kHz MAS. The ^{31}P direct detection (DD-) MAS spectra were collected using a 3.0 μs ^{31}P 90º degree pulse, a recycle delay of 15 seconds, 1024 scans, and 10 kHz MAS. ^{1}H→^{29}Si CP-MAS NMR spectra were collected using a 2.5 μs ^{1}H 90º pulse, a 5 ms ramped (~10%) ^{1}H spin-lock pulse with a ^{29}Si contact pulse with a rf field strength of 62.5 kHz, and 5 kHz MAS. The rf field strength of the ^{1}H channel during the contact time was matched to the -1 spinning side band of the ^{1}H→^{29}Si Hartmann-Hahn profile (57.5 kHz.) The ^{1}H→^{29}Si CP-MAS spectra were typically collected with a recycle delay of 1 second and 32k scans. High power two-pulse phase modulated[57] (TPPM) ^{1}H decoupling (83-100 kHz) was used during the data acquisition for each of the ^{31}P and ^{29}Si experiments. The ^{1}H spectra were

collected using the DEPTH pulse sequence[58] to eliminate background signals from outside the coil, with a recycle delay of 5 seconds and 32 transients. The 2D ^{1}H-^{1}H dipolar DQ/SQ spectra were collected using the back-to-back (BABA) pulse sequence,[59,60] with a 2.5 μs ^{1}H 90º pulse, a recycle delay of 2 seconds, a sweep width of 20 kHz and 128 complex points in the indirect dimension, 64 transients, and a MAS speed of 20 kHz. The 2D EXSY NMR spectra were collected using All ^{31}P chemical shifts were indirectly referenced to 85% phosphoric acid in the solid state by using monobasic ammonium phosphate (δ=0.80 ppm).[61] All ^{29}Si chemical shifts were indirectly referenced to TMS in the solid state by using tetrakis(trimethylsilyl)silane (TTSS) (δ=-9.70 ppm). All ^{1}H chemical shifts were indirectly referenced to TMS in the solid state using adamantane (δ=1.63 ppm). To minimize the signal from residual adsorbed water, the samples were dried under vacuum at 60 ºC for 12 hours immediately prior to NMR analysis. The direct phosphorus spectra were deconvoluted using the software package DMfit;[62] see Figure 1.8. The double quantum build-up curves were calculated using the SIMPSON[63] software package. A simplified ^{1}H-^{1}H two-spin system was used for the calculations, which has been shown to be a valid approximation when moderate MAS speeds are used.[60]

1.3 Results and discussion

A typical TEM image of the as received 7 nm fumed silica nanoparticles is shown in Figure 1.1. This image exemplifies the branching structure of the material, which gives rise to its large surface area. The lack of any lattice structure apparent for the particles is consistent with their inherent amorphous structure. The structures of the two phosphonic acids used to functionalize the fumed silica, methyl phosphonic acid (MPA) and phenyl

phosphonic acid (PPA), are shown in Figure 1.1(b). One of the key factors that differentiates these two phosphonic acids is a notable difference in acidity. The aqueous acid disassociation constant (pK_a) for MPA is 2.38,[64] and the pKa for PPA is 1.83.[65] The effect this difference in acidity has on the binding of the phosphonic acids to silica will be discussed further below.

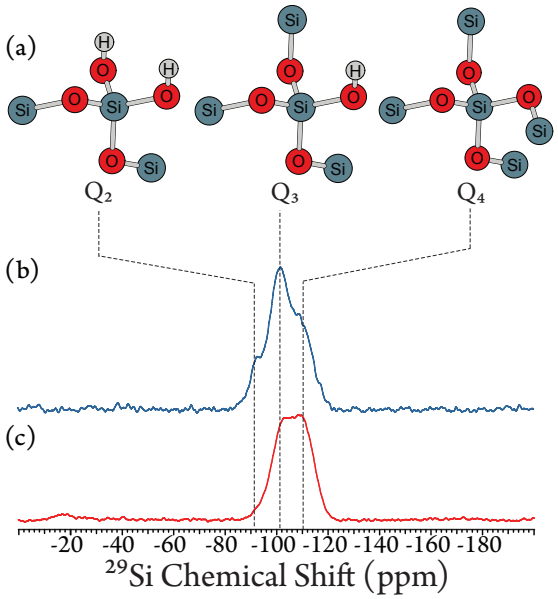

Figure 1.2. $^{1}H \rightarrow ^{29}Si$ CP-MAS spectra for the 7 nm fumed silica starting material dried for 24 hours at 500 ºC (a) and PPA functionalized 7 nm fumed silica (b). The data was collected with a 5 ms contact time and 5 kHz MAS.

The CP-MAS pulse sequence was used for the collection of ^{29}Si NMR because it avoids the inherently long T_1 relaxation time of ^{29}Si in the solid state. Furthermore, the CP pulse sequence will only be sensitive to ^{29}Si sites that are spatially close to silanols, highlighting the surface of the material.[54,66-68] In the ^{29}Si CP-MAS spectrum for the dried silica starting material, there are 3 spectral features observed centered at approximately -90 ppm, -100 ppm and -110 ppm, see Figure 1.2. The peak with a chemical shift of approximately -90 ppm is associated with silicon atoms that have 2 hydroxyl groups

attached to them, often labeled as Q_2 or geminal silanols. The peak with a chemical shift of approximately -100 ppm is associated with silicon atoms with only one hydroxyl group attached, and are often referred to as Q_3 silanols and the peak located at approximately -110 ppm is associated with siloxanes referred to as Q_4.[54,68] The schematic representations of Q_2, Q_3, and Q_4 are shown in Figure 1.2(a) along with the ^{29}Si CP-MAS spectrum. Although quantitative information can be difficult to elucidate from data collected with CP pulse sequences, it is apparent that upon functionalization of the fumed silica with the phosphonic acid ligand, the peak associated with Q_2 silicon environment is severely diminished, leaving only Q_3 silanols and Q_4 sites. This result implies that Q_2 silicon atoms sites are preferentially depleted during synthesis via the reaction with the phosphonic acids. This could mean that the accessibility of the Q_2 silanols is superior to that of the Q_3 silanols. Alternatively, a difference in reactivity of the two types of silanols could be the explanation. Recent ab initio calculations of deprotonation energies involving the silica surface, have indicated that Q_2 silanols are expected to be more acidic than Q_3 silanols by approximately 2.5 pK_a units.[69] This difference in acidity would seem to indicate that the Q_2 silanols would be less reactive. However, the preferential depletion of the Q_2 silanols is observed, which implies that a difference in accessibility of the silanols is likely the cause. This is consistent with the observation of "internal silanols" which are inaccessible to solvent in similar SiO_2 based materials.[70,71]

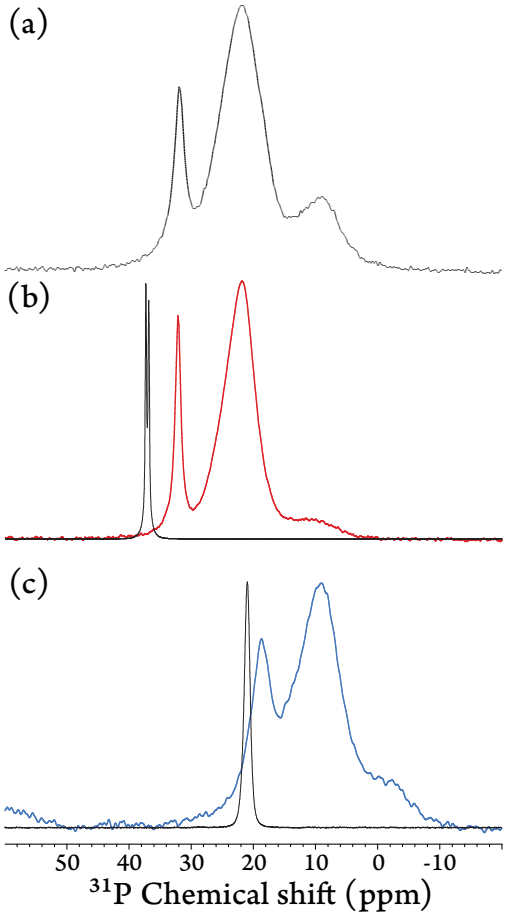

Figure 1.3. $^{1}H \rightarrow ^{31}P$ CP-MAS NMR spectra of (a) fumed silica functionalized with a 1:1 ratio of MPA:PPA, (b) MPA (black) and fumed silica functionalized with MPA (red), and (c) PPA (black) and PPA functionalized 7 nm fumed silica (blue). The spectra were collected with a contact time of 2.5 ms and a sample spinning speed of 10 kHz.

The ^{31}P CP-MAS NMR results, shown in Figure 1.3, display the ligand capped fumed silica along with corresponding spectra of the free ligands. For each of the spectra collected for the ligand-capped silica, there are 3 distinct spectra features, that are all broadened and shifted upfield (lower ppm) with respect to the native ligand. The lack of resonances for the pure ligands in these spectra indicates that the functionalized silica samples have been washed well, and that none of the free ligand remains. An upfield shift (lower ppm) and broadening of peak width compared to free ligand is consistent with

phosphonic acid ligands bound to oxide surfaces, as seen previously in systems of silica,[30,35] SnO_2[1] and TiO_2.[50,51] The observation of 3 distinct resonances can be attributed to the formation of physisorbed, monodentate, and a combination of bidentate and tridentate ligands. Since each condensation of a phosphonic acid should result in a ^{31}P chemical shift upfield (lower ppm), the following assignments can be made: the sharpest, least shifted upfield (lower ppm) of the peaks is associated with the physisorbed ligands, the central moderately broad peak is associated with monodentate ligands, and the furthest shifted broadest peak can be attributed to the bidentate/tridentate ligands. The chemical shifts for the resonances associated with each of the binding modes and phosphonic acids are summarized in Table 1.1. As the ligand interacts more strongly with the surface (going from physisorbed to bidentate) the change in chemical shift relative to the crystalline ligand increases. However, there is a larger change in chemical shift from the crystalline form for each binding mode for MPA than for PPA. This difference indicates a stronger interaction with the silica surface in the case of MPA.

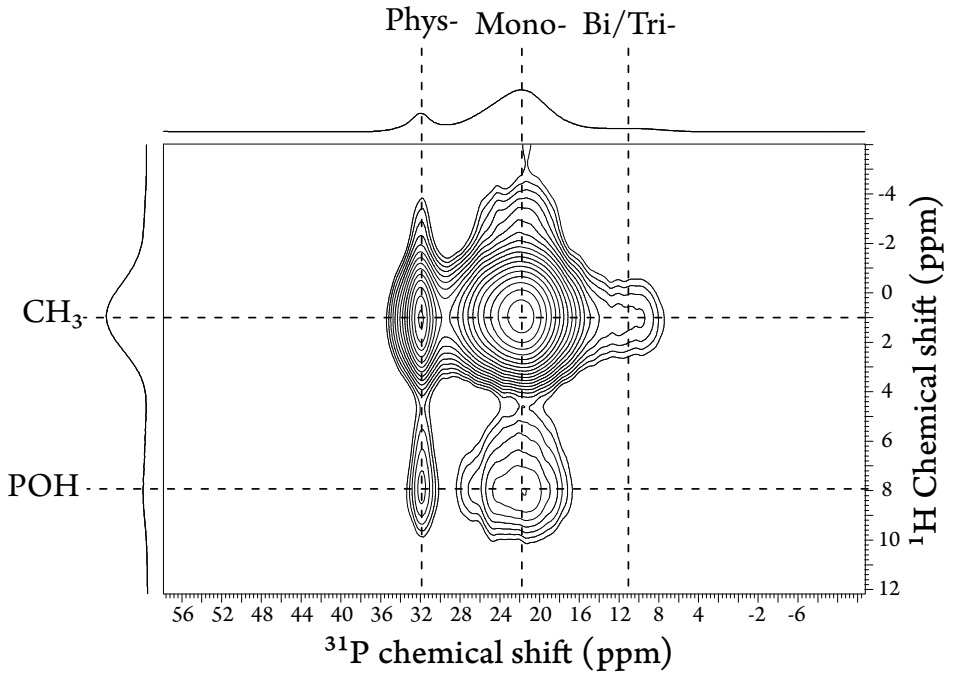

Figure 1.4. $^{1}H \rightarrow ^{31}P$ HETCOR NMR spectrum for MPA functionalized SiO_2. Collected with a contact time of 2.5 ms and 20 kHz MAS.

To confirm the chemical shift assignments a $^{1}H \rightarrow ^{31}P$ heteronuclear correlation (HETCOR) 2D NMR spectrum was collected for the MPA functionalized silica, shown in Figure 1.4. In this spectrum, there is clear resolution of the 3 resonances for physisorbed, monodentate and bi/tridentate MPA on silica in the ^{31}P dimension. Furthermore, in the ^{1}H dimension there is clear resolution between the methyl protons and the protons associated with the protonated phosphonic acid (POH). The fact that a cross peak is observed between the POH and the monodentate, supports the assignments as shown. The lack of a cross peak between the POH and the bi/tridentate peak supports the claim that this resonance is associated with fully deprotonated MPA interacting with the surface. This is in contrast to previous work by our group where it was indicated that PPA binding to SnO_2 nanoparticles resulted in only fully deprotonated surface phosphonic acids.[1] This difference can be attributed to the difference in surface acidity

between SiO_2 and SnO_2, resulting in a weaker bond being formed between the PPA and SiO_2 than in the SnO_2 case. A weaker interaction with the surface could result in the formation of more physisorbed/monodentate type binding modes. To further characterize MPA and PPA binding to SiO_2 nanoparticles, a sample containing an equimolar mixture of both MPA and PPA was synthesized and characterized using ^{31}P CP-MAS (see Figure 3 (a)). The resultant spectrum appears to be a convolution of the spectra for the 2 functionalized silicas that have only one phosphonic acid. In this spectrum it appears that there is more MPA compared to PPA qualitatively, but in order to carefully quantify the populations associated with each resonance direct detection magic angle spinning (DD-MAS) experiments are needed.

Table 1.1. Summary of ^{31}P chemical shift assignments for phosphonic acids binding to silica. Δ is the difference between the ^{31}P chemical shift of that site and the shift of the crystalline phosphonic acid.

Site	*^{31}P Chemical Shift (ppm)*	*Δ (ppm)*
MPA	37.5	0
MPA-SiO_2 (phys)	32.1	5.4
MPA-SiO_2 (monodentate)	21.9	15.6
MPA-SiO_2 (bi/tridentate)	11.0	26.5
PPA	21.2	0
PPA-SiO_2 (phys)	18.5	2.7
PPA-SiO_2 (monodentate)	8.9	12.3
PPA-SiO_2 (bi/tridentate)	-2.0	23.2

The ^{31}P DD-MAS spectra of the phosphonic acid functionalized silicas are shown in Figure 1.4. The collection of fully relaxed ^{31}P NMR data allows for quantification of the different resonances in the ^{31}P spectrum (see Figure 1.8). Deconvolution of the spectra resulted in a ratio of physisorbed to mono-dentate of 42:58 for the MPA-SiO_2 and 37.5:62.5 for the PPA-SiO_2. The deconvolution for the MPA/PPA-SiO_2 sample shows a

ratio of MPA to PPA of 81:19; nearly 4 times more MPA on the surface than PPA. The increase in the presence of MPA on the surface in the mixed ligand case is consistent with the stronger interaction with the surface as indicated by the larger chemical shift differences for the MPA binding modes summarized in Table 1.1. One potential explanation for the overrepresentation of MPA on the surface of the silica compared to PPA is a difference in acidity between the phosphonic acids. The aqueous acid disassociation constant (pK_a) for MPA is 2.38,[64] and the pKa for PPA is 1.83.[65] Therefore, deprotonated MPA would be a stronger base than deprotonated PPA.

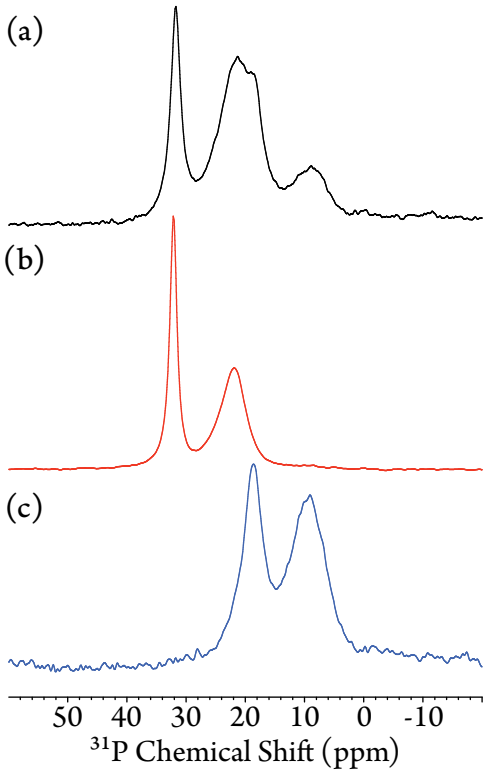

Figure 1.5. ^{31}P MAS NMR for 1:1 MPA:PPA capped fumed silica (a), MPA capped fumed silica (b), and PPA capped fumed silica (c). These spectra were collected with a spinning speed of 10kHz, and a recycle delay of 15s.

The ^{1}H spectra of the phosphonic acid capped fumed silica are shown in Figure 1.6. The complex nature of these spectra arise from the many chemical environments which protons can experience on the silica surface.[66] Additionally, the distribution of observable ^{1}H environments associated with the surface is very sensitive to the drying conditions of the sample.[66] Good resolution is observed in the spectra in spite of being collected at only a moderate MAS speed of 20 kHz. This enhanced resolution is likely due to the elevated dynamics of the ligands attached to the silica surface partially averaging some of the homonuclear dipolar coupling. The large peak at approximately 1 ppm in the MPA capped fumed silica spectrum, which does not appear in the PPA capped fumed silica spectrum, is associated with the methyl group of MPA. The large 2-component peak that is centered at approximately 7 ppm in the spectrum for PPA functionalized fumed silica, is associated with the phenyl ring proton environments of the PPA. The ^{1}H NMR spectrum of MPA functionalized fumed silica there is a proton signal at approximately 8.5 ppm, which is associated with weakly hydrogen bonded POH groups. This resonance is likely present in all of the spectra, making quantifying the PPA signal more difficult. A ^{1}H 2D homonuclear through space correlation experiment, exchange spectroscopy (EXSY), for the 1:1 MPA:PPA functionalized fumed silica is shown in Figure 1.9. This spectrum can be quantified by monitoring the change in volume of peaks as a function of mixing time.[72] However, the convolution of resonances by complex surface species makes quantifying this data difficult. Qualitatively, the presence of a cross peak in this spectrum between the methyl protons (~1 ppm) and the phenyl protons (~7 ppm) indicates that the .the fact that the cross peaks seen contain the multiple peak features observed in the ^{1}H spectrum of PPA capped fumed silica, it can be

concluded that there is a magnetization transfer between the PPA and MPA, and that they spatially near one another (less than or equal to 5 angstroms). The spatial distance between the methyl and phenyl group in this nanostructure can be further quantified using the DQ/SQ BABA 2D experiment.

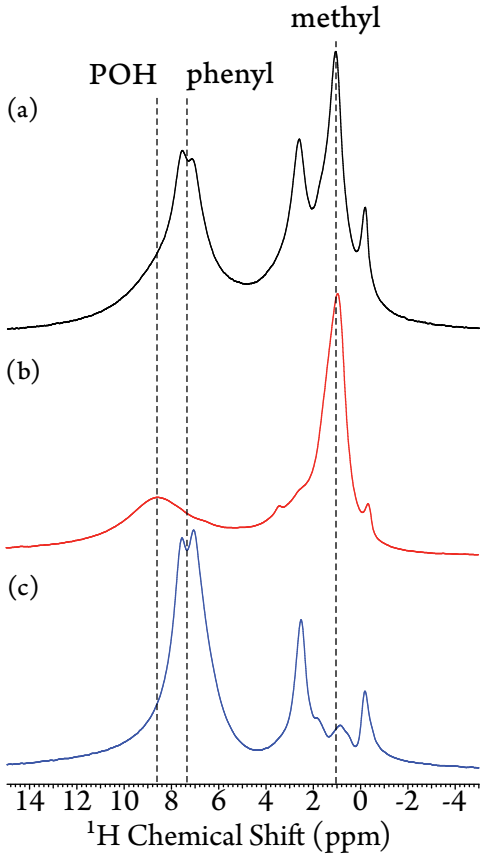

Figure 1.6. ^{1}H-DEPTH NMR spectra of 1:1 mole ratio MPA:PPA capped fumed silica (black), MPA capped fumed silica (red), and PPA capped fumed silica (blue). These spectra were collected with a recycle delay of 5 seconds, 32 scans, and 20 kHz MAS.

The ^{1}H-^{1}H single quantum-double quantum (SQ-DQ) back-to-back (BABA) 2D NMR spectrum for the 1:1 MPA:PPA functionalized fumed silica is shown in Figure 1.7(a). The cross peak located on the diagonal (enclosed by a red box) at approximately 1 ppm in the SQ dimension is associated with an intra-molecular DQ coherence associated

with the methyl of the MPA, as shown in Figure 1.7(b). The cross peak located on the diagonal (enclosed by a green box) at approximately 7 ppm in the SQ dimension is associated with the intra-molecular DQ coherence associated with the protons on the phenyl ring. The peak which appears off the diagonal and has a blue box around it, is an inter-molecular DQ coherence associated with the methyl and phenyl protons. The build up of this inter-molecular DQ coherence as a function of BABA excitation/reconversion blocks has a dependence on the average dipolar coupling between two spins.[73,74] Experimental and simulation results for the NMR signal intensity as a function of dipole coupling and DQ buildup time are shown in Figure 1.7(c). The experimental data points all fall within the range for a spin pair dipole coupling of 1750 ± 250 Hz. The dipole coupling (b_{IS}), can be used in the following equation to calculate the distance between 2 spins (r_{IS}):

$$b_{IS} = \frac{\mu_0 \hbar \gamma_I \gamma_S}{4\pi r_{IS}^3} \qquad (1)$$

where γ_I and γ_S are the gyromagnetic ratios of the two spins, μ_0 is the vacuum permeability, and $\hbar$ is Plank's constant.[75] Calculation of the distance between this spin pair using Equation 1 results in an average distance between the methyl and phenyl protons of this system of 4.2 ± 0.2 Å. Considering that the ligands are dynamic on the surface, the dipolar coupling can only be weakened thus the ligands must be less than or equal to 4.2 Å. Such a close proximity indicates a homogenous distribution of ligands on the surface.

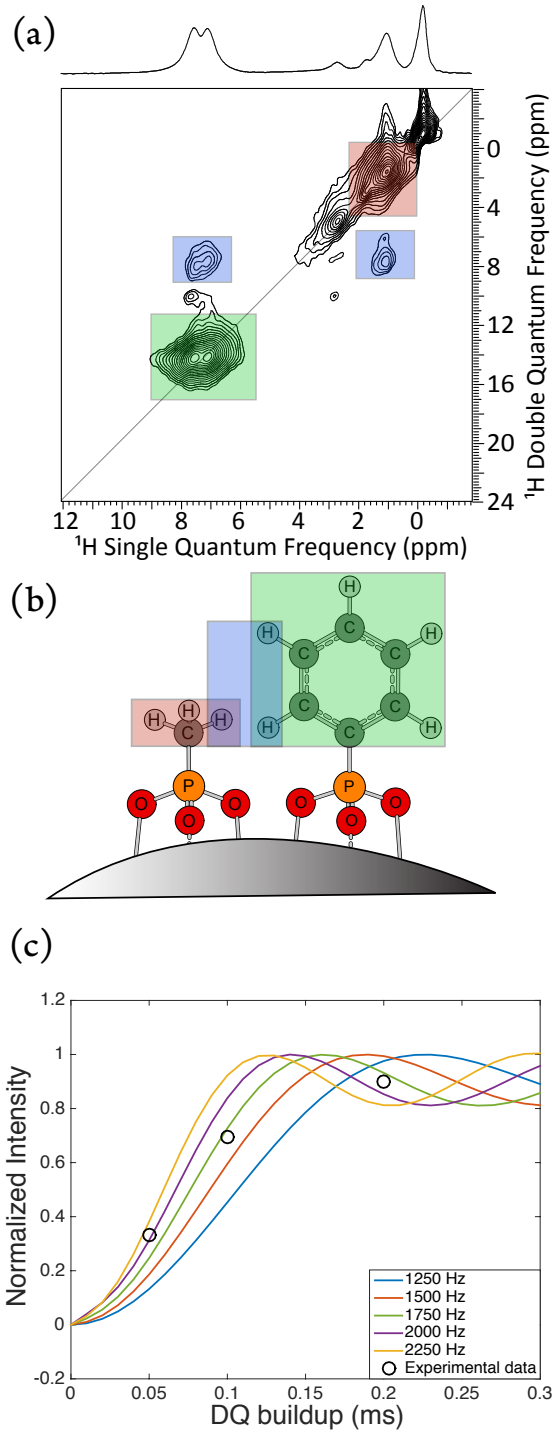

Figure 1.7. A ^{1}H-^{1}H SQ-DQ NMR spectrum for the MPA:PPA capped fumed silica, spinning 20kHz (a), a schematic representation of MPA and PPA on the surface of silica (b), and a DQ coherence buildup curve for the intermolecular DQ resonance. The shown spectrum was collected with 4 rotor cycles of excitation and reconversion, and the $f_1=2f_2$ is shown by the grey diagonal line.

1.4 Conclusions

The ^{31}P and ^{29}Si NMR results have confirmed that phosphonic acid functionalization of the fumed silica has taken place. The ^{29}Si CP-MAS NMR spectra have indicated that geminal silanols are consumed in the functionalization process, and that some (Q3) silanols remain after the functionalization. The ^{31}P NMR spectra of the phosphonic acid functionalized silica showed 3 distinct ligand environments, which have been assigned to physisorbed, monodentate, and bi/tridentate. A larger change in chemical shift associated with binding to silica was observed for MPA than for PPA, indicating MPA interacts with the surface more strongly. Furthermore, quantitative ^{31}P NMR results showed that when silica is functionalized with an equimolar ratio of MPA and PPA, a larger population of MPA is observed on the surface. The good resolution observed in the ^{1}H NMR spectra imply that the ligands are dynamic on the surface. Finally, ^{1}H DQ/SQ BABA NMR build-up curves were used to determine that the average distance between the two ligands on the surface is 4.2 ± 0.2 Å. These results indicate the MPA and PPA ligands are spatially close to one another, such that the ligands are likely homogenously distributed on the silica surface. Solid-state NMR is a powerful approach to characterize ligand binding and organization in multi-ligand systems.

1.5 Supplementary Material

The figures below are provided as supplementary figures to Chapter 1.

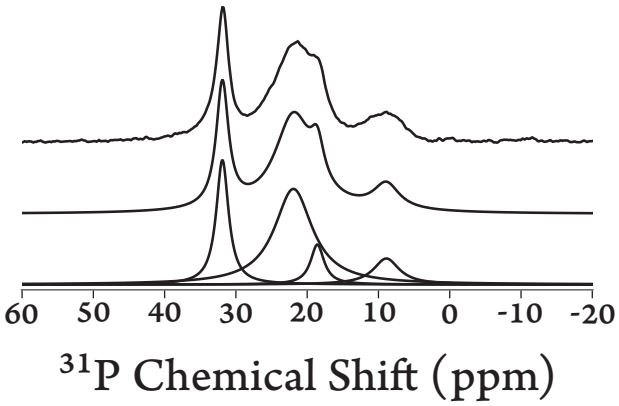

Figure 1.8 ^{31}P MAS NMR spectrum of SiO_2 functionalized with equimolar MPA:PPA deconvoluted using DMFit, original spectrum shown in Figure 1.4 a.

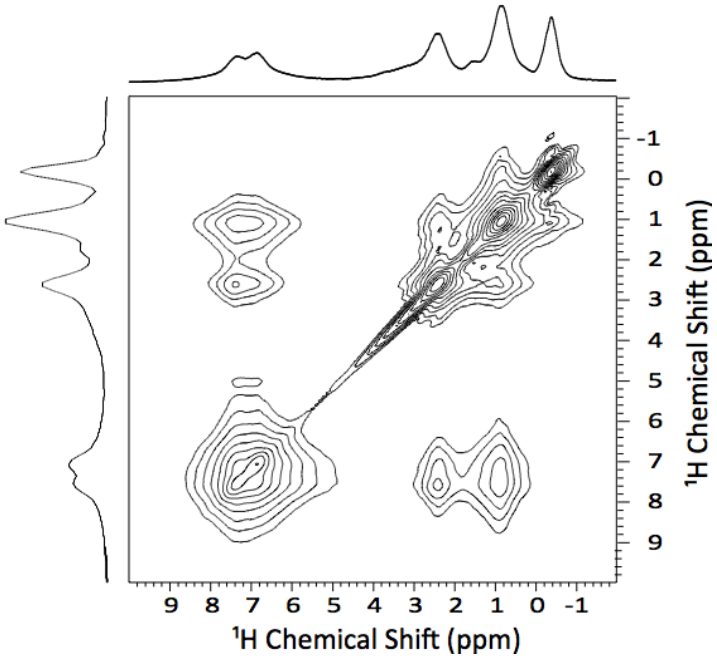

Figure 1.9 ^{1}H EXSY NMR spectrum collected on 1:1 mole ratio MPA:PPA capped fumed silica, collected with a spinning speed of 20kHz and a mixing time of 10ms.

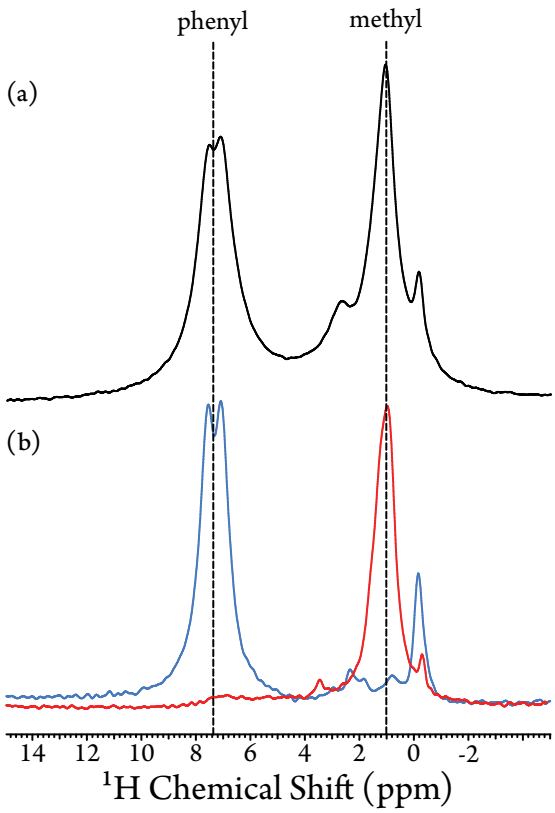

Figure 1.10 ^{1}H-^{1}H BABA-DQ spectra of (a)1:1 mole ratio MPA:PPA capped fumed silica (black), (b) MPA capped fumed silica (red), and PPA capped fumed silica (blue). These spectra were collected with 20 kHz MAS.

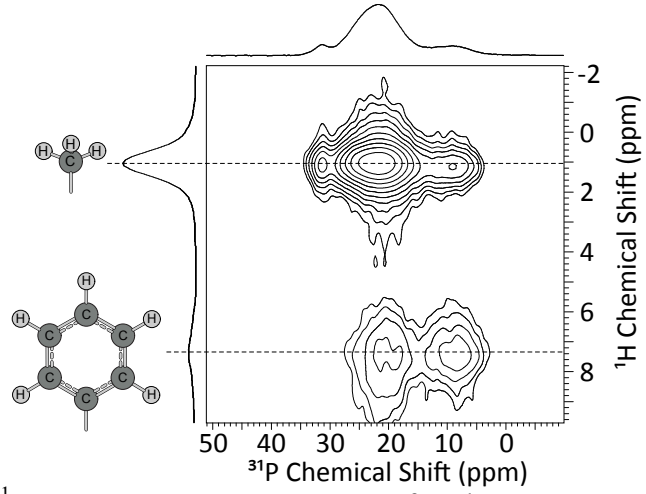

Figure 1.11 ^{1}H→^{31}P HETCOR NMR spectrum for the 1:1 MPA:PPA functionalized SiO_2. Spectrum was collected with a contact time of 2.5 ms and a MAS rate of 20 kHz.

1.6 References

(1) Holland, G. P.; Sharma, R.; Agola, J. O.; Amin, S.; Solomon, V. C.; Singh, P.; Buttry, D. A.; Yarger, J. L. NMR Characterization of Phosphonic Acid Capped SnO_2 Nanoparticles. *Chem. Mater.* **2007**, *19*, 2519–2526.

(2) Kobayashi, T.; Mao, K.; Wang, S.-G.; Lin, V. S.-Y.; Pruski, M. Molecular Ordering of Mixed Surfactants in Mesoporous Silicas: a Solid-State NMR Study. *Solid-State Nucl. Magn. Reson.* **2011**, *39*, 65–71.

(3) Babonneau, F.; Baccile, N.; Laurent, G.; Maquet, J.; Azaïs, T.; Gervais, C.; Bonhomme, C. Solid-State Nuclear Magnetic Resonance: a Valuable Tool to Explore Organic-Inorganic Interfaces in Silica-Based Hybrid Materials. *C. R. Chimie* **2010**, *13*, 58–68.

(4) Wang, W.; Banerjee, S.; Jia, S.; Steigerwald, M. L.; Herman, I. P. Ligand Control of Growth, Morphology, and Capping Structure of Colloidal CdSe Nanorods. *Chem. Mater.* **2007**, *19*, 2573–2580.

(5) Daniel, M.-C.; Astruc, D. Gold Nanoparticles: Assembly, Supramolecular Chemistry, Quantum-Size-Related Properties, and Applications Toward Biology, Catalysis, and Nanotechnology. *Chem. Rev.* **2004**, *104*, 293–346.

(6) Cushing, B. L.; Kolesnichenko, V. L.; O'Connor, C. J. Recent Advances in the Liquid-Phase Syntheses of Inorganic Nanoparticles. *Chem. Rev.* **2004**, *104*, 3893–3946.

(7) Stranick, S. J.; Parikh, A. N.; Tao, Y. T.; Allara, D. L.; Weiss, P. S. Phase Separation of Mixed-Composition Self-Assembled Monolayers Into Nanometer Scale Molecular Domains. *J. Phys. Chem.* **1994**, *98*, 7636–7646.

(8) Smith, R. K.; Reed, S. M.; Lewis, P. A.; Monnell, J. D.; Clegg, R. S.; Kelly, K. F.; Bumm, L. A.; Hutchison, J. E.; Weiss, P. S. Phase Separation Within a Binary Self-Assembled Monolayer on Au{111} Driven by an Amide-Containing Alkanethiol. *J. Phys. Chem. B* **2001**, *105*, 1119–1122.

(9) Lewis, P. A.; Smith, R. K.; Kelly, K. F.; Bumm, L. A.; Reed, S. M.; Clegg, R. S.; Gunderson, J. D.; Hutchison, J. E.; Weiss, P. S. The Role of Buried Hydrogen Bonds in Self-Assembled Mixed Composition Thiols on Au{111}. *J. Phys. Chem. B* **2001**, *105*, 10630–10636.

(10) Jackson, A. M.; Myerson, J. W.; Stellacci, F. Spontaneous Assembly of Subnanometre-Ordered Domains in the Ligand Shell of Monolayer-Protected Nanoparticles. *Nat. Mater.* **2004**, *3*, 330–336.

(11) Jackson, A. M.; Hu, Y.; Silva, P. J.; Stellacci, F. From Homoligand- to Mixed-Ligand- Monolayer-Protected Metal Nanoparticles: a Scanning Tunneling Microscopy Investigation. *J. Am. Chem. Soc.* **2006**, *128*, 11135–11149.

(12) Ong, Q. K.; Zhao, S.; Reguera, J.; Biscarini, F.; Stellacci, F. Comparative STM Studies of Mixed Ligand Monolayers on Gold Nanoparticles in Air and in 1-Phenyloctane. *Chem. Commun.* **2014**, *50*, 10456–10459.

(13) Ong, Q. K.; Reguera, J.; Silva, P. J.; Moglianetti, M.; Harkness, K.; Longobardi, M.; Mali, K. S.; Renner, C.; De Feyter, S.; Stellacci, F. High-Resolution Scanning Tunneling Microscopy Characterization of Mixed Monolayer Protected Gold Nanoparticles. *ACS Nano* **2013**, *7*, 8529–8539.

(14) Vilain, C.; Goettmann, F.; Moores, A.; Le Floch, P.; Sanchez, C. Study of Metal Nanoparticles Stabilised by Mixed Ligand Shell: a Striking Blue Shift of the Surface-Plasmon Band Evidencing the Formation of Janus Nanoparticles. *J. Mater. Chem.* **2007**, *17*, 3509–3514.

(15) Walther, A.; Müller, A. H. E. Janus Particles: Synthesis, Self-Assembly, Physical Properties, and Applications. *Chem. Rev.* **2013**, *113*, 5194–5261.

(16) Singh, C.; Ghorai, P. K.; Horsch, M. A.; Jackson, A. M.; Larson, R. G.; Stellacci, F.; Glotzer, S. C. Entropy-Mediated Patterning of Surfactant-Coated Nanoparticles and Surfaces. *Phys. Rev. Lett.* **2007**, *99*, 226106.

(17) Singh, C.; Jackson, A. M.; Stellacci, F.; Glotzer, S. C. Exploiting Substrate Stress to Modify Nanoscale SAM Patterns. *J. Am. Chem. Soc.* **2009**, *131*, 16377–16379.

(18) Pons-Siepermann, I. C.; Glotzer, S. C. Design of Patchy Particles Using Quaternary Self-Assembled Monolayers. *ACS Nano* **2012**, *6*, 3919–3924.

(19) Shafi, K. V. P. M.; Ulman, A.; Yan, X.; Yang, N.-L.; Estournès, C.; White, H.; Rafailovich, M. Sonochemical Synthesis of Functionalized Amorphous Iron Oxide Nanoparticles. *Langmuir* **2001**, *17*, 5093–5097.

(20) McElwee, J.; Helmy, R.; Fadeev, A. Y. Thermal Stability of Organic Monolayers Chemically Grafted to Minerals. *J. Colloid Interf. Sci.* **2005**, *285*, 551–556.

(21) Marcinko, S.; Fadeev, A. Y. Hydrolytic Stability of Organic Monolayers Supported on TiO 2and ZrO 2. *Langmuir* **2004**, *20*, 2270–2273.

(22) Silverman, B. M.; Wieghaus, K. A.; Schwartz, J. Comparative Properties of Siloxane vs Phosphonate Monolayers on a Key Titanium Alloy. *Langmuir* **2005**, *21*, 225–228.

(23) Hotchkiss, P. J.; Jones, S. C.; Paniagua, S. A.; Sharma, A.; Kippelen, B.; Armstrong, N. R.; Marder, S. R. The Modification of Indium Tin Oxide with Phosphonic Acids: Mechanism of Binding, Tuning of Surface Properties, and Potential for Use in Organic Electronic Applications. *Acc. Chem. Res.* **2012**, *45*, 337–346.

(24) Paniagua, S. A.; Hotchkiss, P. J.; Jones, S. C.; Marder, S. R.; Mudalige, A.; Marrikar, F. S.; Pemberton, J. E.; Armstrong, N. R. Phosphonic Acid Modification of Indium−Tin Oxide Electrodes: Combined XPS/UPS/Contact Angle Studies. *J. Phys. Chem. C* **2008**, *112*, 7809–7817.

(25) Gawalt, E. S.; Avaltroni, M. J.; Koch, N.; Schwartz, J. Self-Assembly and Bonding of Alkanephosphonic Acids on the Native Oxide Surface of Titanium. *Langmuir* **2001**, *17*, 5736–5738.

(26) Guerrero, G.; Mutin, P. H.; Vioux, A. Anchoring of Phosphonate and Phosphinate Coupling Molecules on Titania Particles. *Chem. Mater.* **2001**, *13*, 4367–4373.

(27) Sahoo, Y.; Pizem, H.; Fried, T.; Golodnitsky, D.; Burstein, L.; Sukenik, C. N.; Markovich, G. Alkyl Phosphonate/Phosphate Coating on Magnetite Nanoparticles: a Comparison with Fatty Acids. *Langmuir* **2001**, *17*, 7907–7911.

(28) Pawsey, S.; McCormick, M.; De Paul, S.; Graf, R.; Lee, Y. S.; Reven, L.; Spiess, H. W. 1H Fast MAS NMR Studies of Hydrogen-Bonding Interactions in Self-Assembled Monolayers. *J. Am. Chem. Soc.* **2003**, *125*, 4174–4184.

(29) Hotchkiss, P. J.; Malicki, M.; Giordano, A. J.; Armstrong, N. R.; Marder, S. R. Characterization of Phosphonic Acid Binding to Zinc Oxide. *J. Mater. Chem.* **2011**, *21*, 3107–3112.

(30) Lukes, I.; Borbaruah, M.; Quin, L. D. Direct Reaction of Phosphorus Acids with Hydroxy of a Silanol and on the Silica Gel Surface. *J. Am. Chem. Soc.* **1994**, *116*, 1737–1741.

(31) Hanson, E. L.; Schwartz, J.; Nickel, B.; Koch, N.; Danisman, M. F. Bonding Self-Assembled, Compact Organophosphonate Monolayers to the Native Oxide Surface of Silicon. *J. Am. Chem. Soc.* **2003**, *125*, 16074–16080.

(32) Gouzman, I.; Dubey, M.; Carolus, M. D.; Schwartz, J.; Bernasek, S. L. Monolayer vs. Multilayer Self-Assembled Alkylphosphonate Films: X-Ray Photoelectron Spectroscopy Studies. *Surf. Sci.* **2006**, *600*, 773–781.

(33) Egger, N.; Schmidt-Rohr, K.; Blümich, B.; Domke, W. D.; Stapp, B. Solid State NMR Investigation of Cationic Polymerized Epoxy Resins. *J. Appl. Polym. Sci.* **1992**, *44*, 289–295.

(34) Aliev, A.; Li Ou, D.; Ormsby, B.; Sullivan, A. C. Porous Silica and Polysilsesquioxane with Covalently Linked Phosphonates and Phosphonic Acids. *J. Mater. Chem.* **2000**, *10*, 2758–2764.

(35) Mutin, P. H.; Lafond, V.; Popa, A. F.; Granier, M.; Markey, L.; Dereux, A. Selective Surface Modification of SiO 2−TiO 2Supports with Phosphonic Acids. *Chem. Mater.* **2004**, *16*, 5670–5675.

(36) Gomes, R.; Hassinen, A.; Szczygiel, A.; Zhao, Q.; Vantomme, A.; Martins, J. C.; Hens, Z. Binding of Phosphonic Acids to CdSe Quantum Dots: a Solution NMR Study. *J. Phys. Chem. Lett.* **2011**, *2*, 145–152.

(37) Hassinen, A.; Gomes, R.; De Nolf, K.; Zhao, Q.; Vantomme, A.; Martins, J. C.; Hens, Z. Surface Chemistry of CdTe Quantum Dots Synthesized in Mixtures of Phosphonic Acids and Amines: Formation of a Mixed Ligand Shell. *J. Phys. Chem. C* **2013**, *117*, 13936–13943.

(38) Carbone, L.; Kudera, S.; Carlino, E.; Parak, W. J.; Giannini, C.; Cingolani, R.; Manna, L. Multiple Wurtzite Twinning in CdTe Nanocrystals Induced by Methylphosphonic Acid. *J. Am. Chem. Soc.* **2006**, *128*, 748–755.

(39) Wang, F.; Tang, R.; Kao, J. L.-F.; Dingman, S. D.; Buhro, W. E. Spectroscopic Identification of Tri-N-Octylphosphine Oxide (TOPO) Impurities and Elucidation of Their Roles in Cadmium Selenide Quantum-Wire Growth. *J. Am. Chem. Soc.* **2009**, *131*, 4983–4994.

(40) Dubey, M.; Weidner, T.; Gamble, L. J.; Castner, D. G. Structure and Order of Phosphonic Acid-Based Self-Assembled Monolayers on Si(100). *Langmuir* **2010**, *26*, 14747–14754.

(41) P chy, P. T.; Rotzinger, F. O. P.; Nazeeruddin, M. K.; Kohle, O.; Zakeeruddin, S. M.; Humphry-Baker, R.; Gr tzel, M. Preparation of Phosphonated Polypyridyl Ligands to Anchor Transition-Metal Complexes on Oxide Surfaces: Application for the Conversion of Light to Electricity with Nanocrystalline TiO2 Films. *J. Chem. Soc., Chem. Commun.* **1995**, *0*, 65–66.

(42) Ruile, S.; Kohle, O.; Péchy, P.; Grätzel, M. Novel Sensitisers for Photovoltaic Cells. Structural Variations of Ru(II) Complexes Containing 2,6-Bis(1-Methylbenzimidazol-2-Yl)Pyridine. *Inorganica Chimica Acta* **1997**, *261*, 129–140.

(43) Zakeeruddin, S. M.; Nazeeruddin, M. K.; Pechy, P.; Rotzinger, F. P.; Humphry-Baker, R.; Kalyanasundaram, K.; Grätzel, M.; Shklover, V.; Haibach, T. Molecular Engineering of Photosensitizers for Nanocrystalline Solar Cells: Synthesis and Characterization of Ru Dyes Based on Phosphonated Terpyridines. *Inorg. Chem.* **1997**, *36*, 5937–5946.

(44) Wang, P.; Klein, C.; Moser, J.-E.; Humphry-Baker, R.; Cevey-Ha, N.-L.; Charvet, R.; Comte, P.; Zakeeruddin, S. M.; Grätzel, M. Amphiphilic Ruthenium Sensitizer with 4,4‘-Diphosphonic Acid-2,2‘-Bipyridine as Anchoring Ligand for Nanocrystalline Dye Sensitized Solar Cells. *J. Phys. Chem. B* **2004**, *108*, 17553–17559.

(45) Foster, E. W.; Kearns, G. J.; Goto, S.; Hutchison, J. E. Patterned Gold-Nanoparticle Monolayers Assembled on the Oxide of Silicon. *Adv. Mater.* **2005**, *17*, 1542–1545.

(46) Ito, D.; Jespersen, M. L.; Hutchison, J. E. Selective Growth of Vertical ZnO Nanowire Arrays Using Chemically Anchored Gold Nanoparticles. *ACS Nano* **2008**, *2*, 2001–2006.

(47) Bluemel, J. Reactions of Phosphines with Silicas: a Solid-State NMR Study. *Inorg. Chem.* **1994**, *33*, 5050–5056.

(48) Gao, W.; Dickinson, L.; Grozinger, C.; Morin, F. G.; Reven, L. Self-Assembled Monolayers of Alkylphosphonic Acids on Metal Oxides. *Langmuir* **1996**, *12*, 6429–6435.

(49) Pawsey, S.; Yach, K.; Reven, L. Self-Assembly of Carboxyalkylphosphonic Acids on Metal Oxide Powders. *Langmuir* **2002**, *18*, 5205–5212.

(50) Lafond, V.; Gervais, C.; Maquet, J.; Prochnow, D.; Babonneau, F.; Mutin, P. H. 17O MAS NMR Study of the Bonding Mode of Phosphonate Coupling Molecules in a Titanium Oxo-Alkoxo-Phosphonate and in Titania-Based Hybrid Materials. *Chem. Mater.* **2003**, *15*, 4098–4103.

(51) Brodard-Severac, F.; Guerrero, G.; Maquet, J.; Florian, P.; Gervais, C.; Mutin, P. H. High-Field 17O MAS NMR Investigation of Phosphonic Acid Monolayers on Titania. *Chem. Mater.* **2008**, *20*, 5191–5196.

(52) Neff, G. A.; Page, C. J.; Meintjes, E.; Tsuda, T.; Pilgrim, W. C.; Roberts, N.; Warren, W. W. Hydrolysis of Surface-Bound Phosphonate Esters for the Self-Assembly of Multilayer Films: Use of Solid State Magic Angle Spinning 31P NMR as a Probe of Reactions on Surfaces. *Langmuir* **1996**, *12*, 238–242.

(53) Kosmulski, M. Compilation of PZC and IEP of Sparingly Soluble Metal Oxides and Hydroxides From Literature. *Adv Colloid Interface Sci* **2009**, *152*, 14–25.

(54) Liu, C. C.; Maciel, G. E. The Fumed Silica Surface: a Study by NMR. *J. Am. Chem. Soc.* **1996**, *118*, 5103–5119.

(55) Brei, V. V. 29Si Solid-State NMR Study of the Surface Structure of Aerosil Silica. *J. Chem. Soc., Faraday Trans.* **1994**, *90*, 2961.

(56) Gun'ko, V. M.; Voronin, E. F.; Pakhlov, E. M.; Zarko, V. I.; Turov, V. V.; Guzenko, N. V.; Leboda, R.; Chibowski, E. Features of Fumed Silica Coverage with Silanes Having Three or Two Groups Reacting with the Surface. *Colloids Surf., A* **2000**, *166*, 187–201.

(57) Bennett, A. E.; Rienstra, C. M.; Auger, M.; Lakshmi, K. V.; Griffin, R. G. Heteronuclear Decoupling in Rotating Solids. *J. Chem. Phys.* **1995**, *103*, 6951–6957.

(58) Cory, D. G.; Ritchey, W. M. Suppression of Signals From the Probe in Block Decay Spectra. *J. Magn. Reson.* **1988**, *80*, 128–132.

(59) Feike, M.; Demco, D. E.; Graf, R.; Gottwald, J.; Hafner, S.; Spiess, H. W. Broadband Multiple-Quantum NMR Spectroscopy. *J. Magn. Reson., Ser A* **1996**, *122*, 214–221.

(60) Schnell, I.; Spiess, H. W. High-Resolution 1H NMR Spectroscopy in the Solid State: Very Fast Sample Rotation and Multiple-Quantum Coherences. *J. Magn. Reson.* **2001**, *151*, 153–227.

(61) Hayashi, S.; Hayamizu, K. High-Resolution Solid-State 31P NMR of Alkali Phosphates. *Bull. Chem. Soc. Jpn.* **1989**.

(62) Massiot, D.; Fayon, F.; Capron, M.; King, I.; Calve, S. L.; Alonso, B.; Durand, J. O.; Bujoli, B.; Gan, Z.; Hoatson, G. Modelling One- and Two-Dimensional Solid-State NMR Spectra. *Magn. Reson. Chem.* **2002**, *40*, 70–76.

(63) Bak, M.; Rasmussen, J. T.; Nielsen, N. C. SIMPSON: a General Simulation Program for Solid-State NMR Spectroscopy. *J. Magn. Reson.* **2000**, *147*, 296–330.

(64) Crofts, P. C.; Kosolapoff, G. M. Preparation and Determination of Apparent Dissociation Constants of Some Alkylphosphonic and Dialkylphosphinic Acids 1. *J. Am. Chem. Soc.* **1953**, *75*, 3379–3383.

(65) Jaffé, H. H.; Freedman, L. D.; Doak, G. O. The Acid Dissociation Constants of Aromatic Phosphonic Acids. I. Meta and Para Substituted Compounds 1. *J. Am. Chem. Soc.* **1953**, *75*, 2209–2211.

(66) Trébosc, J.; Wiench, J. W.; Huh, S.; Lin, V. S.-Y.; Pruski, M. Solid-State NMR Study of MCM-41-Type Mesoporous Silica Nanoparticles. *J. Am. Chem. Soc.* **2005**, *127*, 3057–3068.

(67) Trébosc, J.; Wiench, J. W.; Huh, S.; Lin, V. S.-Y.; Pruski, M. Studies of Organically Functionalized Mesoporous Silicas Using Heteronuclear Solid-State Correlation NMR Spectroscopy Under Fast Magic Angle Spinning. *J. Am. Chem. Soc.* **2005**, *127*, 7587–7593.

(68) Maciel, G. E.; Sindorf, D. W. Silicon-29 NMR Study of the Surface of Silica Gel by Cross Polarization and Magic-Angle Spinning. *J. Am. Chem. Soc.* **1980**, *102*, 7606–7607.

(69) Tielens, F.; Gervais, C.; Lambert, J.-F.; Mauri, F.; Costa, D. Ab Initio Study of the Hydroxylated Surface of Amorphous Silica: a Representative Model. *Chem. Mater.* **2008**, *20*, 3336–3344.

(70) Chuang, I. S.; Kinney, D. R.; Maciel, G. E. Interior Hydroxyls of the Silica Gel System as Studied by Silicon-29 CP-MAS NMR Spectroscopy. *J. Am. Chem. Soc.* **1993**, *115*, 8695–8705.

(71) d'espinose de la Caillerie, J.-B.; Aimeur, M. R.; Kortobi, Y. E.; Legrand, A. P. Water Adsorption on Pyrogenic Silica Followed by1H MAS NMR. *J. Colloid Interf. Sci.* **1997**, *194*, 434–439.

(72) Perrin, C. L.; Dwyer, T. J. Application of Two-Dimensional NMR to Kinetics of Chemical Exchange. *Chem. Rev.* **1990**, *90*, 935–967.

(73) Brown, S. P. Probing Proton–Proton Proximities in the Solid State. *Prog. Nucl. Magn. Reson. Spectrosc.* **2007**, *50*, 199–251.

(74) Brown, S. P. Applications of High-Resolution 1H Solid-State NMR. *Solid-State Nucl. Magn. Reson.* **2012**, *41*, 1–27.

(75) Schmidt-Rohr, K.; Spiess, H. W. Multidimensional Solid-State NMR and Polymers - Klaus Schmidt-Rohr, Hans Wolfgang Spiess - Google Books. **1994**.

Chapter 2

Characterizing mixed phosphonic acid ligand capping on CdSe/ZnS quantum dots using ligand exchange and NMR spectroscopy

2.1 Introduction

The synthesis and characterization of highly luminescent core-shell quantum dot (QD) systems have been a major focus of study in the past several years[1] due to their excellent stability and photoluminescent properties.[2-4] Advances in robustness and functionality have been attributed to more efficient passivation of the photoactive core via the additional inorganic shell of semiconductor,[5,6] rather than passivation by organic ligands alone. The CdSe/ZnS system has been of particular interest in this area, due to a band gap allowing for tunable optical properties spanning the visible light range,[1] high quantum yields,[4] and a relatively well understood synthesis.[7-10]

Understanding the details of the ligand structure at the surface of QDs is imperative for the reproducible production of high quality QDs. Ligand effects are vital for size and shape control during the synthesis of QDs.[11-14] Additionally, ligand effects have been shown to affect the structure of the of the nanomaterial at the ligand interface,[15,16] as well as the resulting quantum yield of the nanoparticles.[17,18] Alkyl phosphonic acids (PAs) are routinely used as organic passivating ligands for nanomaterials,[19,20] due to their multidentate[21,22] strong binding,[23] and stability.[24] The utilization of PAs for functionalization of QDs has been popularized by the identification of their role as the ligands involved in the surface chemistry of QDs prepared in technical grade tri-N-octylphosphine oxide (TOPO).[12,13,25,26]

Nuclear magnetic resonance (NMR) spectroscopy is a versatile tool for studying the structure of functionalized nanomaterials, and can be used to effectively identify ligands in a QD system and characterize the ligand environment.[21,27] The use of ^{31}P NMR allows for the facile identify phosphorus-containing ligands and other species,[13,25,28] and has the potential to reveal information about the bonding environment of the ligand.[22] When phosphorus-containing ligands such as PAs are bound to the surface of QDs, they typically show significant heterogeneously broadened resonances in ^{31}P NMR.[21,29] Furthermore, there is usually a significant change in the ^{31}P chemical shift compared to the free ligand in solution.[30] The combination of broadening and change in chemical shift of the surface bound ligands compared to the free ligands allows for facile simultaneous identification and quantification of ligands in different environments. Solid-state NMR is a tool which has been used considerably in the literature for the characterization of CdSe QD systems,[28,31,32] and can be utilized to give detailed information about inter-nuclear distances and chemical environments.[33]

Ligand exchange is often used to replace the hydrophobic ligands of CdSe/ZnS QDs, with hydrophilic ligands to render the QDs water-soluble,[34-36] but ligand exchange also has the potential to offer qualitative and quantitative information about the ligand populations on the surface of quantum dots. Ligand exchange, in conjunction with ^{31}P NMR, has been used to identify phosphonic acids displaced from the surface of QDs using a variety of strategies. An array of different Trimethylsilyl type ligands have been used to liberate ligands from QD surfaces for subsequent analysis.[37-39] Phosphonic acid ligands have also previously been displaced from the surface of CdSe QDs,[20] using a large excess of propionate.[25] There has also been a comparative study of ligand exchange

using oleic acid and alkyl phosphonic acids to displace each other, which has shown that alkyl phosphonic acids bind preferentially to the surface of CdSe QDs.[29]

Here we present a method for quantifying phosphorus-containing ligands on the surface of CdSe/ZnS QDs via a ligand exchange reaction and subsequent ^{31}P NMR analysis. We use phenyl phosphonic acid (PPA) to displace the alkyl phosphonic acids, ethyl phosphonic acid (EPA) and tetradecyl phosphonic acid (TDPA) from the surface of the QDs. The extent of ligand exchange is then confirmed by washing away the excess free ligand and observing the populations of surface-bound ligands using solid and liquid state ^{31}P NMR.

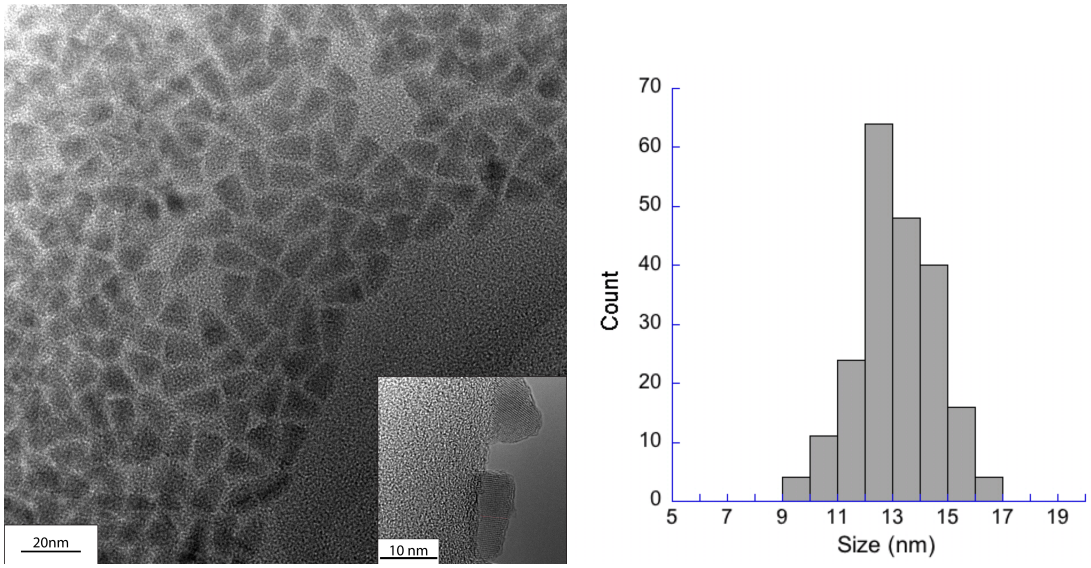

Figure 2.1 TEM images of the CdSe/ZnS QDs, and a histogram showing the size dispersity of the NPs, measured along the long axis of the particles. (n=210 particles.)

2.2 Experimental

Materials. The core-shell CdSe/ZnS QDs used in this study were provided by the Life Technologies Corporation and were generated according to standard synthetic methods.[40]

Fully deuterated chloroform (D, 99.8%) and methanol (D, 99.8%) were obtained from Cambridge isotopes laboratories and the phenyl phosphonic acid (98%) used in this work was obtained from Sigma-Aldrich. All materials were used as received without any further purification.

TEM. High-resolution transmission electron microscopy (HR-TEM), used to image the size and structure of the quantum dot samples, was carried out using a Phillips CM-200 TEM fitted with a Schottky field emission gun and a Gatan CCD camera, operating at an accelerating voltage of 200 kV, with a point to point resolution of 2.5 Å. Samples for analysis by TEM were prepared by sonicating the solid QD sample into suspension in hexanes and placing a drop of that solution onto a lacey carbon film with copper grid support. After allowing the grid to incubate for a few minutes the excess suspension was removed and the grid was allowed to air-dry prior to analysis via TEM. Images were acquired and processed using the software Gatan - Digital Micrograph.

NMR analysis of Quantum Dot samples. The liquid-state ^{31}P NMR spectra were collected utilizing a 400 MHz Bruker Avance III spectrometer equipped with a 5 mm double resonance broadband probe configured for ^{1}H-^{31}P operation. The spectra were all collected with a ^{31}P $\pi/2$ pulse length of 10.0 μs, a 10 s recycle delay, and WALTZ proton decoupling during acquisition.[41] Chemical shifts were referenced to phosphoric acid (δ=0 ppm).

Solid-state NMR spectra were collected on a 400 MHz wide-bore Varian VNMRS spectrometer equipped with a Varian 4 mm triple resonance probe configured for ^{1}H - ^{31}P operation. ^{1}H$\rightarrow$^{31}P cross polarization magic angle spinning (CP-MAS) spectra were collected with a MAS speed of 10 kHz, a recycle delay of 5 seconds and 83

kHz two pulse phase modulated[42] (TPPM) proton decoupling with a phase shift of 6.5° during acquisition. The ^{1}H $\pi/2$ pulse used in the sequence was 3.0 μs, and the CP utilized a 2.5 ms ramped (~15 %) ^{1}H spin-lock pulse (62kHz) matched to the -1 spinning sideband of the Hartman-Hahn matching profile with a 72 kHz ^{31}P square contact pulse. ^{31}P direct detection magic angle spinning (DD-MAS) spectra were collected with a ^{31}P $\pi/2$ pulse of 3.5 μs, a MAS speed of 10 kHz, a recycle delay of 60 s, and 62.5 kHz TPPM proton decoupling during acquisition. Chemical shifts were indirectly referenced to phosphoric acid (δ=0 ppm) using the solid sample ammonium phosphate ($NH_4H_2PO_4$, δ=0.8 ppm).

Ligand exchange procedure. In a 5 mL tube, 10.50 mg of a QD sample was dissolved in 700 uL of a 3:1 (vol/vol) mixture of deuterated chloroform and deuterated methanol ($CDCl_3$:MeOD). Subsequently, a 100 uL aliquot of a stock solution of PPA, which had been generated by adding 7.50 mg to 750 uL of $CDCl_3$ and 250 uL of MeOD, was added (resulting in the addition of approximately 0.75 mg of PPA). This solution was mixed using a pipette and placed into a 5 mm NMR tube for liquid state NMR analysis. To remove the excess free ligand, the solution was pipetted from the NMR tube into a 2 mL Eppendorf tube, and the solid was precipitated via the addition of approximately 1 mL of methanol. This sample was centrifuged and the supernatant discarded. The solid sample was washed with approximately 1 mL of methanol, and dried under a flow of nitrogen gas. In order to prepare larger sample sizes needed for solid state NMR, a 50 mL centrifuge tube was charged with 5.00 mL of a 3:1 (v/v) mixture of $CHCl_3$:MeOH, approximately 50 mg of QD sample, and 3.57 mg of PPA (for an approximate molar ratio of PPA:TDPA+EPA of 1:1). This mixture was shaken for approximately 5 minutes

and the solid QDs were precipitated via the addition of 10 mL of methanol and separated from the solution via centrifugation. These samples were further washed with approximately 5 mL of methanol, and dried under a flow of nitrogen gas prior to analysis.

2.3 Results and discussion

TEM images were obtained for the QDs in order to determine size, dispersity, and morphology. Representative TEM image shown in Figure 2.1 displays the common triangular shape and aspect ratio of the QDs. The size of the QDs was found to be 12.7+/-1.4 nm (n=210 particles) along the long axis of the particles. The TEM results show that the QDs used in this study are relatively monodisperse and highly crystalline, as seen from the lattice fringes in the images.

Stacked ^{31}P CP-MAS NMR spectra of the QDs functionalized with varying ratios of TDPA and EPA are shown in Figure 2.2, along with lines at the chemical shifts of the pure ligands. Resonances for the surface bound ligands are broadened and upfield for the ligands bound to the QDs compared to that of the native ligands. Resonances for the bound TDPA and bound EPA are convoluted, inhibiting direct quantification from solid-state NMR.

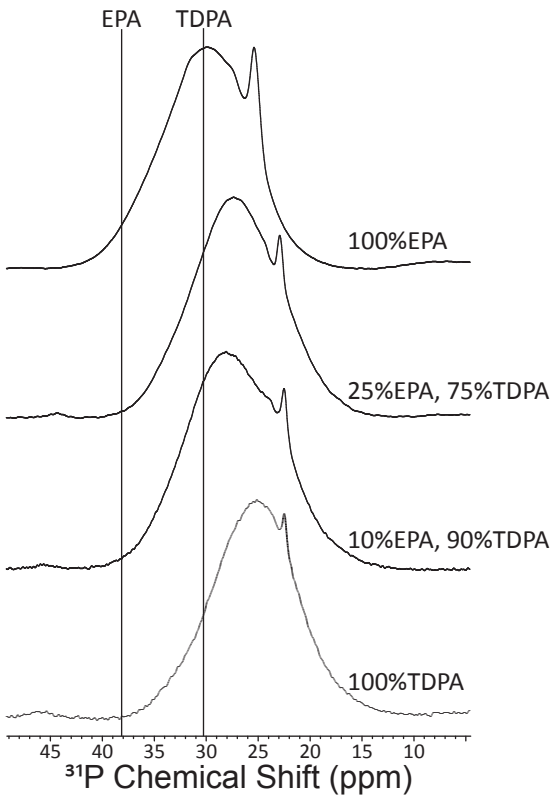

Figure 2.2 ^{31}P CP-MAS solid-state NMR of CdSe/ZnS quantum dot samples capped with different ratios of phosphonic acid capping ligands. The lines represent the chemical shifts of the pure ligands. The MAS speed for these spectra was 10 kHz.

The upfield shift and broadening of resonances associated with phosphonic acid ligands bound to the surface of nanoparticles is consistent with previous solid state NMR studies.[21,28,43] The broadening of the resonances for the bound ligands is likely due to a heterogeneous distribution of chemical shifts, which has been observed in a previous study of phosphonic acids binding to metal oxides.[21] There is a notable shift in the peak maximum between the spectrum for 100% EPA functionalized QDs (30.0 ppm) and the spectrum for 100% TDPA functionalized QDs (25.1 ppm). However, the peak maximum does not scale linearly with phosphonic acid composition as shown by the peak maximums for the spectra of 25:75 EPA-TDPA (27.2 ppm) and 10:90 EPA-TDPA (28.1 ppm). This could be due to the chemical shift of the peak maximum depending partially

on factors other than ligand composition; such as a distribution of mono-, bi- and tri dentate binding modes.[21,22,44]

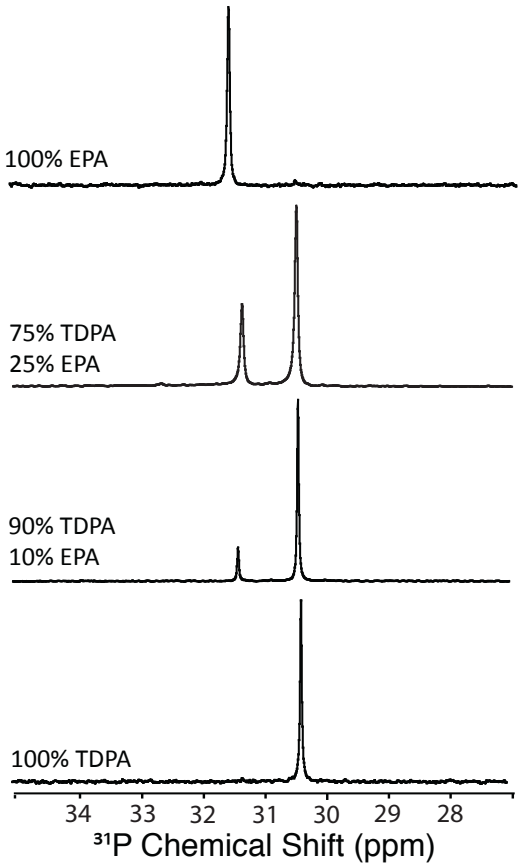

Figure 2.3 Ligand exchange $^{31}P\{^{1}H\}$ liquid state NMR of CdSe/ZnS quantum dots with approximately a 1:1 ratio of ligands on the surface to PPA dissolved in a mixture of 3:1 $CDCl_3$:MeOD.

Liquid ^{31}P NMR spectra were collected for the PA functionalized QDs after ligand exchange with PPA, see Figure 2.3. For each of the ligand exchange spectra the downfield peak at 31.4 ppm has been assigned to free EPA, and the upfield peak at 30.5 ppm has been assigned to free TDPA; the resonance for free PPA is not shown.

Table 2.1 Comparison of the ratios of the phosphonic acid ligands used to stabilize the QDs during synthesis and the ratio of the 2 ligands observed via ligand exchange and subsequent ^{31}P NMR.

EPA:TDPA as synthesized	EPA:TDPA Observed
0:100	0:100
10:90	16:84
25:75	31:69
100:0	100:0

Integration of the fully relaxed ^{31}P resonances allows for the determination of the ratio of displaced EPA to TDPA in each of these samples. A summary of the integrated areas of the resonances is shown in Table 2.1. The ratio of the observed displaced ligands is closely related to the ratio of the ligands used during the synthesis of these QDs (within 6%). The fact that the ligands are displaced in a similar ratio implies that the phosphonic acids used in this study have a comparable binding affinity for the surface of the QDs. This method allows for the facile quantification of the ligands on the surface of the QDs.

Washing the QD samples after the ligand exchange reactions allows for the removal of free ligand from the solution. The collection of liquid-state ^{31}P NMR spectra with a large number of scans (4k or more in this case) facilitates the observation of the broad resonances associated with PAs bound to the surface of the quantum dots, as shown in Figure 2.4. The two broad resonances centered at 17 ppm and 30 ppm have been assigned to PPA bound to the surface and the convolution of TDPA and EPA bound to the surface respectively.

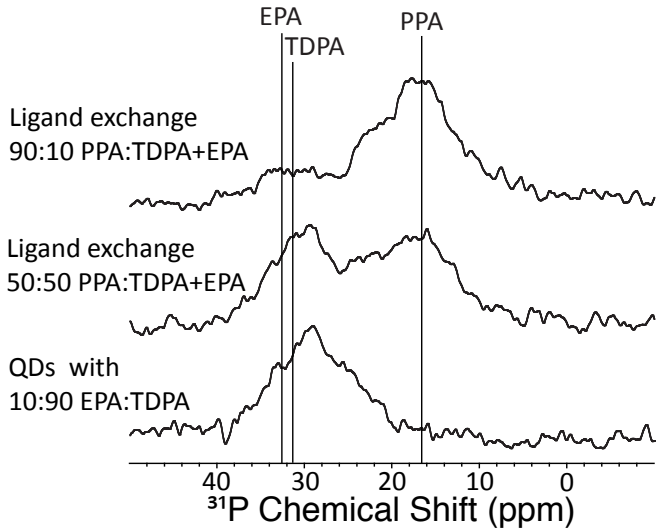

Figure 2.4 $^{31}P\{^{1}H\}$ liquid-state NMR of CdSe/ZnS quantum dots with various ratios of ligands on the surface dissolved in a mixture of 3:1 $CDCl_3$:MeOD, after ligand exchange the samples were precipitated with methanol and washed with methanol to remove excess free ligand and redissolved in 3:1 $CDCl_3$:MeOD.

The fact that the resonances in these spectra are broad and remain after washing is consistent with the claim that they are associated with ligands bound to the surface of the QDs. These data imply that the ratio of PPA to TDPA+EPA on the surface of the quantum dots can be controlled using this ligand exchange technique and that the ratio of PPA to TDPA+EPA used in ligand exchange is similar to the ratio of ligands on the surface, even after washing away the excess ligand. The presence of both PPA and TDPA+EPA in this spectrum indicates that the PPA has a similar binding affinity to the surface as the alkyl phosphonic acids due to its inability to completely displace them at similar ligand concentrations. This is in contrast to some previous studies in which incoming ligands of a higher binding affinity, such as bis(trimethysilyl)-selenide, were used to displace all of the phosphonic acid ligands.[29,37]

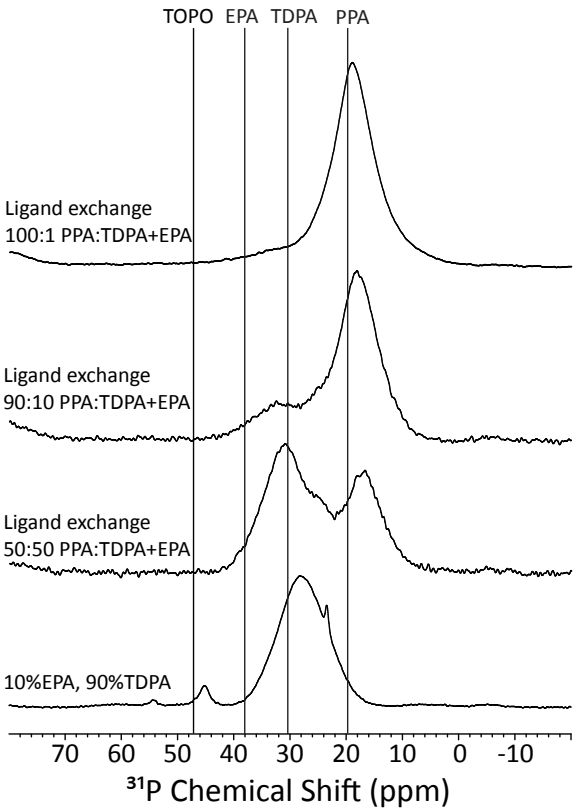

Figure 2.5 ^{31}P solid-state DD-MAS NMR spectra for dried PA functionalized QDs before and after ligand exchange reactions using approximate molar ratios of ligand on the surface to PPA of 1:1, 1:10, and 1:100. Lines are shown at the chemical shifts for the ligands TOPO, EPA, TDPA and PPA obtained from ^{1}H - ^{31}P CPMAS spectra. The MAS speed for these spectra was 10 kHz.

Precipitation of the QDs from the solution after washing away the excess ligand from the ligand exchange allows for solid-state ^{31}P MAS-NMR analysis, as shown in Figure 2.5. A summary of the areas associated with each of the resonances in the spectra is shown in Table 2.2. The resulting fully relaxed ^{31}P spectra indicate that following ligand exchange with PPA, a slight excess of alkyl PAs is observed. This is likely due to the fact that PPA is a weaker base than the alkyl PAs,[45,46] leading to a slightly lower binding affinity.

Table 2.2 Ratios of the ligands used during the ligand exchange reactions and the ratios observed on the surface of the QDs using solid-state NMR and liquid-state NMR.

PPA:TDPA+EPA during exchange	PPA:TDPA+EPA ssNMR	PPA:TDPA+EPA NMR
90:10	85:15	89:11
50:50	33:67	46:54

The results from the ^{31}P solid-state NMR spectra are in good agreement with those obtained using ^{31}P liquid-state NMR on the QDs in solution shown in Figure 2.5. A summary of the comparison of the ratios detected between the two methods is shown in Table 2.2. These results indicate that liquid-state NMR can be used to directly quantify ligand populations on the surface of the QDs, when sufficient resolution between the broad resonances of surface bound ligands is observed.

2.4 Conclusions

Ligand exchange reactions utilizing PPA to displace alkyl phosphonic acid ligands from QDs for subsequent ^{31}P NMR analysis have shown to be an effective and facile method for quantifying the populations of ligands on the surface of QDs. This method is optimal for use in systems utilizing multiple phosphorus containing ligands. Further, this method will only be effective in systems where the binding affinity of PPA is sufficient to displace the native ligands. In the present study it was found that the ratio of EPA to TDPA observed using this method closely correlated to the ratio of ligands used in the synthesis of the QDs. The ligands on the surface of the QDs which remain after washing away the free ligand, can be observed using liquid and solid state ^{31}P NMR, allowing for direct quantification of ligand populations from these spectra if there is sufficient resolution between the broad resonances. After ligand exchange with PPA, the

observed underrepresentation of PPA on the surface of the QDs indicates that PPA has a slightly lower binding affinity for the QDs than the alkyl phosphonic acids.

2.5 References

(1) Chaudhuri, R. G.; Paria, S. Core/Shell Nanoparticles: Classes, Properties, Synthesis Mechanisms, Characterization, and Applications. *Chem. Rev.* **2012**, *112*, 2373–2433.

(2) Hines, M. A.; Guyot-Sionnest, P. Synthesis and Characterization of Strongly Luminescing ZnS-Capped CdSe Nanocrystals. *J. Phys. Chem.* **1996**, *100*, 468–471.

(3) Dabbousi, B. O.; Rodriguez-Viejo, J.; Mikulec, F. V.; Heine, J. R.; Mattoussi, H.; Ober, R.; Jensen, K. F.; Bawendi, M. G. (CdSe)ZnS Core−Shell Quantum Dots: Synthesis and Characterization of a Size Series of Highly Luminescent Nanocrystallites. *J. Phys. Chem. B* **1997**, *101*, 9463–9475.

(4) Peng, X.; Schlamp, M. C.; Kadavanich, A. V.; Alivisatos, A. P. Epitaxial Growth of Highly Luminescent CdSe/CdS Core/Shell Nanocrystals with Photostability and Electronic Accessibility. *J. Am. Chem. Soc.* **1997**, *119*, 7019–7029.

(5) Reiss, P.; Protière, M.; Li, L. Core/Shell Semiconductor Nanocrystals. *Small* **2009**, *5*, 154–168.

(6) Chon, B.; Lim, S. J.; Kim, W.; Seo, J.; Kang, H.; Joo, T.; Hwang, J.; Shin, S. K. Shell and Ligand-Dependent Blinking of CdSe -Based Core/Shell Nanocrystals. *Phys. Chem. Chem. Phys.* **2010**, *12*, 9312–9319.

(7) Liu, H.; Owen, J. S.; Alivisatos, A. P. Mechanistic Study of Precursor Evolution in Colloidal Group II−VI Semiconductor Nanocrystal Synthesis. *J. Am. Chem. Soc.* **2007**, *129*, 305–312.

(8) García-Rodríguez, R.; Hendricks, M. P.; Cossairt, B. M.; Liu, H.; Owen, J. S. Conversion Reactions of Cadmium Chalcogenide Nanocrystal Precursors. *Chem. Mater.* **2013**, *25*, 1233–1249.

(9) Abe, S.; Capek, R. K.; De Geyter, B.; Hens, Z. Reaction Chemistry/Nanocrystal Property Relations in the Hot Injection Synthesis, the Role of the Solute Solubility. *ACS Nano* **2013**, *7*, 943–949.

(10) Yu, K.; Liu, X.; Zeng, Q.; Yang, M.; Ouyang, J.; Wang, X.; Tao, Y. The Formation Mechanism of Binary Semiconductor Nanomaterials: Shared by Single-Source and Dual-Source Precursor Approaches. *Angew Chem Int Ed* **2013**, *52*, 11034–11039.

(11) Wang, W.; Banerjee, S.; Jia, S.; Steigerwald, M. L.; Herman, I. P. Ligand Control of Growth, Morphology, and Capping Structure of Colloidal CdSe Nanorods. *Chem. Mater.* **2007**, *19*, 2573–2580.

(12) Wang, F.; Tang, R.; Buhro, W. E. The Trouble with TOPO; Identification of Adventitious Impurities Beneficial to the Growth of Cadmium Selenide Quantum Dots, Rods, and Wires. *Nano Lett.* **2008**, *8*, 3521–3524.

(13) Wang, F.; Tang, R.; Kao, J. L.-F.; Dingman, S. D.; Buhro, W. E. Spectroscopic Identification of Tri-N-Octylphosphine Oxide (TOPO) Impurities and Elucidation of Their Roles in Cadmium Selenide Quantum-Wire Growth. *J. Am. Chem. Soc.* **2009**, *131*, 4983–4994.

(14) Huang, J.; Kovalenko, M. V.; Talapin, D. V. Alkyl Chains of Surface Ligands Affect Polytypism of CdSe Nanocrystals and Play an Important Role in the Synthesis of Anisotropic Nanoheterostructures. *J. Am. Chem. Soc.* **2010**, *132*, 15866–15868.

(15) Frederick, M. T.; Achtyl, J. L.; Knowles, K. E.; Weiss, E. A.; Geiger, F. M. Surface-Amplified Ligand Disorder in CdSe Quantum Dots Determined by Electron and Coherent Vibrational Spectroscopies. *J. Am. Chem. Soc.* **2011**, *133*, 7476–7481.

(16) Morris-Cohen, A. J.; Frederick, M. T.; Lilly, G. D.; McArthur, E. A.; Weiss, E. A. Organic Surfactant-Controlled Composition of the Surfaces of CdSe Quantum Dots. *J. Phys. Chem. Lett.* **2010**, *1*, 1078–1081.

(17) Hassinen, A.; Moreels, I.; De Nolf, K.; Smet, P. F.; Martins, J. C.; Hens, Z. Short-Chain Alcohols Strip X-Type Ligands and Quench the Luminescence of PbSe and CdSe Quantum Dots, Acetonitrile Does Not. *J. Am. Chem. Soc.* **2012**, *134*, 20705–20712.

(18) Coto-García, A. M.; Fernández-Argüelles, M. T. The Influence of Surface Coating on the Properties of Water-Soluble CdSe and CdSe/ZnS Quantum Dots. *J. Nanopart. Res.* **2013**, *15*, 1330–1341.

(19) Pawsey, S.; Yach, K.; Reven, L. Self-Assembly of Carboxyalkylphosphonic Acids on Metal Oxide Powders. *Langmuir* **2002**, *18*, 5205–5212.

(20) Morris-Cohen, A. J.; Donakowski, M. D.; Knowles, K. E.; Weiss, E. A. The Effect of a Common Purification Procedure on the Chemical Composition of the Surfaces of CdSe Quantum Dots Synthesized with Trioctylphosphine Oxide. *J. Phys. Chem. C* **2010**, *114*, 897–906.

(21) Holland, G. P.; Sharma, R.; Agola, J. O.; Amin, S.; Solomon, V. C.; Singh, P.; Buttry, D. A.; Yarger, J. L. NMR Characterization of Phosphonic Acid Capped SnO 2Nanoparticles. *Chem. Mater.* **2007**, *19*, 2519–2526.

(22) Brodard-Severac, F.; Guerrero, G.; Maquet, J.; Florian, P.; Gervais, C.; Mutin, P. H. High-Field 17O MAS NMR Investigation of Phosphonic Acid Monolayers on Titania. *Chem. Mater.* **2008**, *20*, 5191–5196.

(23) Marcinko, S.; Fadeev, A. Y. Hydrolytic Stability of Organic Monolayers Supported on TiO 2and ZrO 2. *Langmuir* **2004**, *20*, 2270–2273.

(24) McElwee, J.; Helmy, R.; Fadeev, A. Y. Thermal Stability of Organic Monolayers Chemically Grafted to Minerals. *J. Colloid Interf. Sci.* **2005**, *285*, 551–556.

(25) Kopping, J. T.; Patten, T. E. Identification of Acidic Phosphorus-Containing Ligands Involved in the Surface Chemistry of CdSe Nanoparticles Prepared in Tri-N-Octylphosphine Oxide Solvents. *J. Am. Chem. Soc.* **2008**, *130*, 5689–5698.

(26) Peng, X.; Manna, L.; Yang, W.; Wickham, J.; Scher, E.; Kadavanich, A.; Alivisatos, A. P. Shape Control of CdSe Nanocrystals. *Nature* **2000**, *404*, 59–61.

(27) Hens, Z.; Martins, J. C. A Solution NMR Toolbox for Characterizing the Surface Chemistry of Colloidal Nanocrystals. *Chem. Mater.* **2013**, *25*, 1211–1221.

(28) Ratcliffe, C. I.; Yu, K.; Ripmeester, J. A.; Badruz Zaman, M.; Badarau, C.; Singh, S. Solid State NMR Studies of Photoluminescent Cadmium Chalcogenide Nanoparticles. *Phys. Chem. Chem. Phys.* **2006**, *8*, 3510–3519.

(29) Gomes, R.; Hassinen, A.; Szczygiel, A.; Zhao, Q.; Vantomme, A.; Martins, J. C.; Hens, Z. Binding of Phosphonic Acids to CdSe Quantum Dots: a Solution NMR Study. *J. Phys. Chem. Lett.* **2011**, *2*, 145–152.

(30) Moreels, I.; Martins, J. C.; Hens, Z. Ligand Adsorption/Desorption on Sterically Stabilized InP Colloidal Nanocrystals: Observation and Thermodynamic Analysis. *ChemPhysChem* **2006**, *7*, 1028–1031.

(31) Iacono, F.; Palencia, C.; la Cueva, de, L.; Meyns, M.; Terracciano, L.; Vollmer, A.; la Mata, de, M. J.; Klinke, C.; Gallego, J. M.; Juarez, B. H.; et al. Interfacing Quantum Dots and Graphitic Surfaces with Chlorine Atomic Ligands. *ACS Nano* **2013**, *7*, 2559–2565.

(32) Steigerwald, M. L.; Alivisatos, A. P.; Gibson, J. M.; Harris, T. D.; Kortan, R.; Muller, A. J.; Thayer, A. M.; Duncan, T. M.; Douglass, D. C.; Brus, L. E. Surface Derivatization and Isolation of Semiconductor Cluster Molecules. *J. Am. Chem. Soc.* **1988**, *110*, 3046–3050.

(33) Tomaselli, M.; Yarger, J. L.; Bruchez, M.; Havlin, R. H.; deGraw, D.; Pines, A.; Alivisatos, A. P. NMR Study of InP Quantum Dots: Surface Structure and Size Effects. *J. Chem. Phys.* **1999**, *110*, 8861.

(34) Jeong, S.; Achermann, M.; Nanda, J.; Ivanov, S.; Klimov, V. I.; Hollingsworth, J. A. Effect of the Thiol-Thiolate Equilibrium on the Photophysical Properties of Aqueous CdSe/ZnS Nanocrystal Quantum Dots. *J. Am. Chem. Soc.* **2005**, *127*, 10126–10127.

(35) Dubois, F.; Mahler, B.; Dubertret, B.; Doris, E.; Mioskowski, C. A Versatile Strategy for Quantum Dot Ligand Exchange. *J. Am. Chem. Soc.* **2007**, *129*, 482–483.

(36) Zylstra, J.; Amey, J.; Miska, N. J.; Pang, L.; Hine, C. R.; Langer, J.; Doyle, R. P.; Maye, M. M. A Modular Phase Transfer and Ligand Exchange Protocol for Quantum Dots. *Langmuir* **2011**, *27*, 4371–4379.

(37) Owen, J. S.; Park, J.; Trudeau, P.-E.; Alivisatos, A. P. Reaction Chemistry and Ligand Exchange at Cadmium−Selenide Nanocrystal Surfaces. *J. Am. Chem. Soc.* **2008**, *130*, 12279–12281.

(38) Hassinen, A.; Gomes, R.; De Nolf, K.; Zhao, Q.; Vantomme, A.; Martins, J. C.; Hens, Z. Surface Chemistry of CdTe Quantum Dots Synthesized in Mixtures of Phosphonic Acids and Amines: Formation of a Mixed Ligand Shell. *J. Phys. Chem. C* **2013**, *117*, 13936–13943.

(39) Caldwell, M. A.; Albers, A. E.; Levy, S. C.; Pick, T. E.; Cohen, B. E.; Helms, B. A.; Milliron, D. J. Driving Oxygen Coordinated Ligand Exchange at Nanocrystal Surfaces Using Trialkylsilylated Chalcogenides. *Chem. Commun.* **2011**, *47*, 556–558.

(40) Murray, C. B.; Norris, D. J.; Bawendi, M. G. Synthesis and Characterization of Nearly Monodisperse CdE (E = Sulfur, Selenium, Tellurium) Semiconductor Nanocrystallites. *J. Am. Chem. Soc.* **1993**, *115*, 8706–8715.

(41) Shaka, A. J.; Keeler, J.; Frenkiel, T.; Freeman, R. An Improved Sequence for Broadband Decoupling: WALTZ-16. *J. Magn. Reson.* **1983**, *52*, 335–338.

(42) Bennett, A. E.; Rienstra, C. M.; Auger, M.; Lakshmi, K. V.; Griffin, R. G. Heteronuclear Decoupling in Rotating Solids. *J. Chem. Phys.* **1995**, *103*, 6951–6957.

(43) Gutmann, T.; Bonnefille, E.; Breitzke, H.; Debouttière, P.-J.; Philippot, K.; Poteau, R.; Buntkowsky, G.; Chaudret, B. Investigation of the Surface Chemistry of Phosphine-Stabilized Ruthenium Nanoparticles--an Advanced Solid-State NMR Study. *Phys. Chem. Chem. Phys.* **2013**, *15*, 17383–17394.

(44) Lafond, V.; Gervais, C.; Maquet, J.; Prochnow, D.; Babonneau, F.; Mutin, P. H. ^{17}O MAS NMR Study of the Bonding Mode of Phosphonate Coupling Molecules in a Titanium Oxo-Alkoxo-Phosphonate and in Titania-Based Hybrid Materials. *Chem. Mater.* **2003**, *15*, 4098–4103.

(45) Crofts, P. C.; Kosolapoff, G. M. Preparation and Determination of Apparent Dissociation Constants of Some Alkylphosphonic and Dialkylphosphinic Acids 1. *J. Am. Chem. Soc.* **1953**, *75*, 3379–3383.

(46) Jaffé, H. H.; Freedman, L. D.; Doak, G. O. The Acid Dissociation Constants of Aromatic Phosphonic Acids. I. Meta and Para Substituted Compounds 1. *J. Am. Chem. Soc.* **1953**, *75*, 2209–2211.

Chapter 3

NMR characterization of ionicity and transport properties for a series of diethylmethylamine based protic ionic liquids

3.1 Introduction

Ionic liquids (IL) have been the subject of considerable interest due to their diverse applications, particularly as solvents and electrolytes for fuel cell and battery materials.[1-9] These compounds exhibit unique combinations of properties such as thermal stability well beyond 100 ºC, low vapor pressures, high ionic conductivity, and non-flammability, making them ideal for use in fuel cell and battery applications where chemical stability and safety is necessary.[10,11]

Ionic liquids are typically grouped into two classes: protic and aprotic. Protic Ionic Liquids (PIL) are the subset which function through proton transfer from Brønsted acid-base chemistry while inheriting many of the properties of the aprotic class. The proton transfer reaction creates an equilibrium between molecular species, ion pairs, and dissociated ions where incomplete proton transfer leads to neutral species and ion pair aggregates, making it difficult to quantify and define the ionicity of a PIL.[12,13] The degree of proton transfer has been estimated using aqueous pKa values of acids and bases, and provides an adequate prediction in systems with large ΔpKa.[11] However, solvents can play a significant role in proton exchange, as shown by the large differences in pKa values of acids in various media, thus raising concerns about the validity of using aqueous pKa values for pure PIL systems.[14,15] In this paper, we discuss the concept of using proton affinities in place of pKa to estimate the proton transfer behavior of a PIL based on its constituents.

Although a standard method for determining ionicity is not established, the performance of most PIL have been assessed using a Walden plot when conductivity and viscosity are known.[10,16,17] Vibrational spectroscopy and thermal techniques offer qualitative insight into the formation of ionic species, intermolecular interactions, and transport characteristics of PIL and its constituents, which can be used to gauge the degree of proton transfer.[7,8,18] In contrast, NMR spectroscopy has proven to be particularly useful for its quantitative ability to probe proton environments, providing measurements of chemical shifts and J-coupling to determine the degree of proton transfer.[12,19-22] Perhaps more useful is the ability to directly measure the transport behavior of individual ionic species by NMR, where diffusion coefficients can be obtained from various experiments utilizing magnetic field gradients and spin echo pulse sequences. Recent studies on PIL have taken advantage of these experiments to measure the diffusion coefficients of ionic species in PIL and calculate conductivities via the Nernst-Einstein equation, providing another quantitative method for determining ionicity.[19,20]

In the present work, ^{1}H and ^{15}N NMR is used to probe the behavior and ionicity of several DEMA based PIL and compare the results to conductivity based measurements. DEMA based PILs have been studied extensively with various acids (anions) for their ability to form low melting point compounds while showing promise as anhydrous proton conducting materials above 100 ºC.[1,3,23-25] Acids of varying strength have been chosen to illustrate a range of proton transfer conditions which can be probed experimentally with NMR. These measurements correlate well with calculated proton affinities, providing a useful technique for predicting the proton transfer characteristics of a PIL.

3.2 Experimental

Materials. N,N-Diethylmethylamine (DEMA, 97%), acetic anhydride (AcA, >99%), trifluoroacetic acid (TFA, 99%), trifluoroacetic anhydride (TFAA, >99%), tetrafluoroboric acid (HBF_4, 48%), and perchloric acid ($HClO_4$, 70%) were obtained from Fisher scientific (USA). Calcium hydride (CaH_2, 95%), methanesulfonic acid (MS, ≥99.5%), acetic acid (HAc, 97%), nitric acid (HNO_3, 70%), and sulfuric acid (H_2SO_4, 99%) were obtained from Sigma-Aldrich (USA). Triflic acid (HOtf, ≥98%) was obtained from Alfa Aesar (USA). Bis(trifluoromethane)sulfonimide (HTFSI, ≥95%) was obtained from Synquest Laboratories (USA). Diethylmethylamine (DEMA) was dried via distillation from CaH_2 prior to use. The resulting dried amine was determined to have less than 40 ppm water, measured by Karl-Fischer titration. The acetic acid was dried by mixing with the appropriate amount of acetic anhydride to render it anhydrous. The same method was used to dry the trifluoroacetic acid using trifluoroacetic anhydride. All other materials were used as received.

Ionic liquid synthesis. Ionic liquids were synthesized by drop wise addition of each acid to form a 1:1 mole ratio mixture with the base. To limit exposure to water, the reactions were carried out under a nitrogen atmosphere. In an effort to prevent decomposition of any of the materials during the course of the exothermic proton transfer reactions, each synthesis was placed in a dry ice in acetone bath. A typical synthesis was carried out using the following procedure: approximately 5 g of dried DEMA (57.4 mmole) was added to a round bottom flask under a nitrogen atmosphere. A pressure equalizing addition funnel was filled with 57.4 mmole of the appropriate acid and fitted to the round-bottomed flask containing the base. The flask was submerged in a bath of dry ice

and acetone and a magnetic stir plate. The acid was then added drop-wise to the base, typically resulting in a white/amber solid, which melted upon re-heating to room temperature. Ionic liquids synthesized with weaker acids (acetic acid and trifluoroacetic acid) were transferred directly to a nitrogen atmosphere glove box. Ionic liquids synthesized with stronger acids were dried in a vacuum oven at 60-80 °C for approximately 2 days with a container of P_2O_5. Upon completion of the drying process, the ionic liquids were transferred to a nitrogen atmosphere glove box. DEMA-TFSI was synthesized with the same procedure except that the solid HTFSI was placed in the round bottom flask and DEMA was added drop wise to the acid.

NMR spectroscopy. All NMR studies were carried out on samples that were flame sealed in 5 mm NMR tubes to prevent air exposure. ^{1}H NMR spectra were collected using a 400 MHz Varian VNMRS spectrometer equipped with a Varian 5mm double resonance ^{1}H-X broad band probe. Data were collected using a recycle delay of 5-10 seconds, 8 scans and a 45^o ^{1}H pulse with a duration of 5.30 μs. The frequency of the spectrometer was not locked during data acquisition due to the lack of a deuterated solvent. The magnetic field was shimmed manually for each sample to minimize magnetic field inhomogeneities. ^{1}H spectra were collected at 25 ºC for all PILs except DEMA-NO_3 and DEMA-BF_4, which are solids at room temperature. ^{1}H NMR spectra for these PILs were collected at 50 ºC; ^{1}H chemical shifts for all PILs were found to have a negligible dependence on temperature in this range. All ^{1}H chemical shifts were externally referenced to the TMS peak of a mixture of 1% TMS in $CDCl_3$ shortly before the spectra were collected. ^{15}N NMR spectra of the ionic liquids were collected using a 400 MHz Varian VNMRS spectrometer equipped with a Varian 5 mm double resonance

^{1}H – X broad band probe operating at a 40.499 MHz resonant frequency. ^{15}N spectra were collected without ^{1}H decoupling to allow observation of J_{NH} coupling when present. Data were collected using a recycle delay of 2 seconds and averaging 256-1024 transients. All ^{15}N chemical shifts were indirectly referenced to methyl nitrite by setting the resonance for benzamide to -277.8 ppm shortly before the spectra were collected.

Diffusion coefficients were measured using a pulsed field gradient stimulated echo (PFG-STE) pulse sequence with bipolar gradient pulses.[26] Data were collected utilizing 800 MHz Varian VNMRS spectrometer equipped with a 5 mm Doty PFG probe operating at proton resonant frequency of 799.85 MHz, and a ^{19}F resonant frequency of 752.5. Proton Spectra were collected with a recycle delay of 5 seconds, 16 transients, a 90^{o} pulse with a duration of 16.5-18.0 μs, 20-40 ms diffusion delay (Δ), 0.5 ms gradient length (δ), and a maximum gradient strength (g) of approximately 1200 G/cm depending on the diffusivity of the ionic liquid. For the PILs synthesized with fluorinated acids, (TFA and Otf) ^{19}F PFG-NMR was used to measure the diffusivity of the anions. The ^{19}F spectra were collected with a recycle delay of 3 seconds, 16 transients, a 90^{o} pulse with a duration of 19.5 μs, 25 ms diffusion delay (Δ), 0.5 ms gradient length (δ), and a maximum gradient strength (g) of approximately 1000 G/cm depending on the diffusivity of the ionic liquid. During each measurement the temperature was regulated at 25 $^{\circ}C$.

Electronic structure calculations. In an attempt to quantify the strength of the acids used in this study, gas phase electronic structure calculations were used to obtain proton affinities. Proton affinity for each acid was calculated using the density functional theory (DFT) B3LYP functional with the 6-31G (d) basis set in Gaussian09.[27] The structures of the acid, its conjugate base and a bare proton were geometry optimized prior to executing

thermochemistry calculations. A comparison of the proton affinities obtained from ab initio calculations to available literature values is shown in Figure 3.7. The results obtained via electronic structure calculations are all within ±6 kcal/mol of literature values.

Conductivity measurements. Ionic conductivities were determined from complex impedance data from a PAR VMP2 potentiostat (Princeton Applied Research) with a frequency range of 10 Hz to1 MHz. The dip-type conductivity cells for liquid electrolytes were constructed with platinum electrodes sealed in soft glass. Cell constants of about 1 cm^{-1} were determined using a standard 0.01 M KCl solution. Approximately 1 mL of solution was used to perform each measurement. Conductivities were measured from 25 ºC to 105 ºC with 10 ºC steps. Temperatures were controlled using Yamato Scientific DKN-402 programmable oven. Viscosity for each PIL was determined using a Brookfield DV-E viscometer. Densities were measured using a 1.5 mL volumetric flask and a scale.

3.3 Results and discussion

^{1}H NMR is a valuable tool in the study of PILs due to its ability to investigate the properties of the transferred proton. A subset of the ^{1}H NMR spectra collected for these DEMA PILs is shown in Figure 3.1. The resonances below 4 ppm labeled with "B_1-B_3" are associated with the diethylmethylamine base (cation). The peaks denoted with "A" are resonances associated with the acid (anion). The peaks labeled with "E" are resonances associated with the exchangeable proton for each ionic liquid and have chemical shifts ranging from approximately 6 to 14 ppm. The exchangeable proton is the hydrogen atom which has been transferred from the Brønsted acid to the base. The

general trend observed in this series of spectra is that as the strength of the acid increases, the chemical shift of the exchangeable proton is shifted upfield (to lower ppm values). The shift of the exchangeable proton has information about how strongly the proton is associated with the base. There is a large difference in chemical shift between the proton associated with an acid (c.10-12 ppm) and associated with the DEMA-H^+ (3-4 ppm).

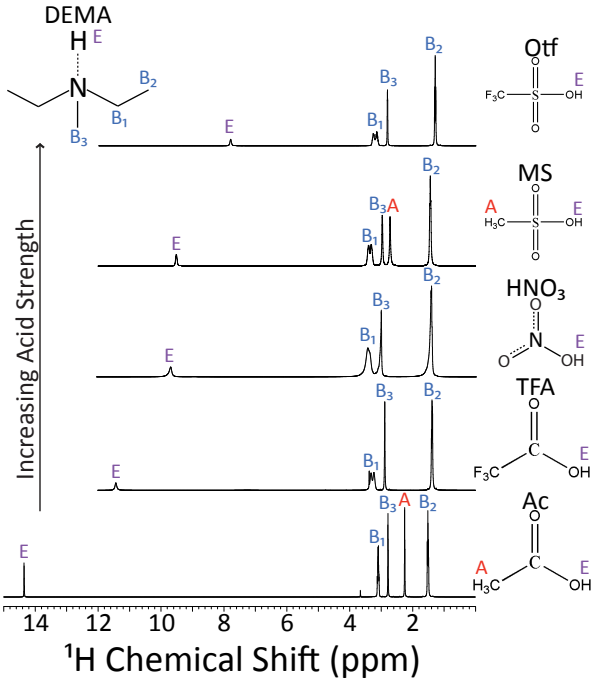

Figure 3.1. ^{1}H NMR spectra for DEMA based ionic liquids generated with various acids. The structure and abbreviation for each acid is shown to the right of the corresponding spectrum. The symbols A, B, and E correspond to protons associated with the acid, base, and exchangeable protons respectively.

Due to the fast exchange of the proton between the acid and the base relative to the timescale of the NMR measurement, a single peak is observed for the exchangeable protons. Furthermore, as the strength of the acid increases, the chemical shift of the exchangeable proton approaches that of the pure protonated base without any weak base interaction from the anion. This upfield shift is indicative of an increase in the shielding

experienced by the exchangeable proton due to its increased interaction with the lone pair of electrons on the amine. Similarly, as the strength of the acid weakens, the expectation is that the chemical shift of the exchangeable proton would approach that of the proton attached to the acid. However, this does not appear to be the case. In the weakest acid case studied here, an exchangeable proton chemical shift of 14.35 ppm is observed, which is downfield from pure acetic acid (12.2 ppm). This indicates that the hydrogen bond formed between the anion and the protonated base is causing a de-shielding of the exchangeable proton.[28] The trend of chemical shift of exchangeable proton with acid strength is consistent with a previous study on a smaller set of TEA based PILs.[20]A similar trend has been observed by Denisov et al. when recording the ^{1}H chemical shifts of a series of 1:1 mixtures of acids and pyridine dissolved in CD_2Cl_2.[29] A chemical shift maximum was observed at 20.5 ppm for the exchangeable proton of dichloroacetic acid and pyridine (ΔpK_a=3.9). This chemical shift indicates the presence of a strong hydrogen bond between the acid and the base. We predict that if weaker acids were included in this set of ionic liquids, a similar result would be observed. A chemical shift maximum was not observed in our system due to DEMA being a stronger base (pK_a=10.6) than pyridine (pK_a =5.2). This difference in strength of conjugate acids leads to a more complete proton transfer for DEMA than for pyridine, with acids of comparable strength.

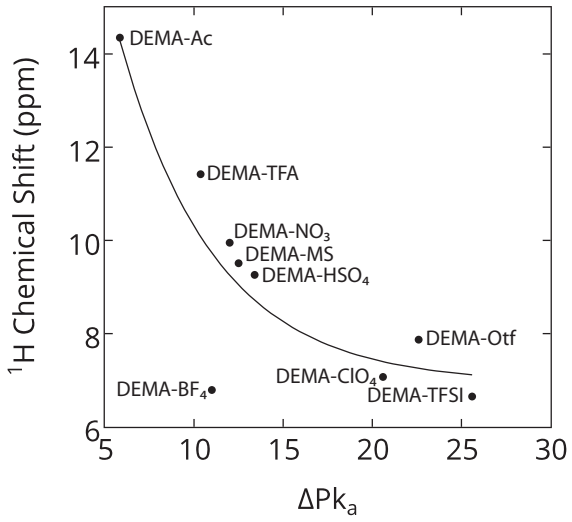

Figure 3.2. Chemical shift of the exchangeable proton for each DEMA based ionic liquid extracted from the ^{1}H spectra as a function of acid strength.

The extent of protonation in protic ionic liquids has previously been correlated to the value of ΔpK_a, which is defined as the difference between the aqueous pK_a of the protonated base ($pK_a(BH^+)$) and the protonated acid ($pK_a(AH)$) as shown in eq 1.[11,16]

$$\Delta pK_a = pK_a(BH^+) - pK_a(AH) \qquad (1)$$

The larger the ΔpK_a for a PIL, the stronger the driving force for the proton transfer. The measurement of aqueous pKa values for superacids are typically obtained by measuring the relative acidity of the molecule of interest with respect to a standard in a non-aqueous solvent and then approximating the solvation effect of water.[30] The assumption associated with using ΔpK_a in this context, is that the free energy of solvation by water, from the pure PIL state to the aqueous standard state, is the same for cation and anion components, which is not unreasonable when both anion and cation are large.[16] However, this approximation cannot be expected to hold in all cases. There is evidence of

solvation energies playing an important role in the relative acidities of a set of super acids.[31]

A plot correlating the ^{1}H chemical shift of the exchangeable proton of each ionic liquid with its ΔpK_a is shown in Figure 3.2. The overall trend observed is that as the strength of the acid increases, the resonance of the exchangeable proton is shifted upfield (lower ppm values). In general the ionic liquids with smaller ΔpK_a values fit the trend more closely, while the ionic liquids synthesized with super acids seem to have larger deviations from the trend. Furthermore, in the case of the acid HBF_4 the aqueous ΔpK_a leads to chemical shift which does not match the trend, likely due to the role water plays in its acidity. Most of these issues appear to arise from aqueous super acid pK_a values having less bearing on the true acidity of these molecules in the context of ionic liquid synthesis.

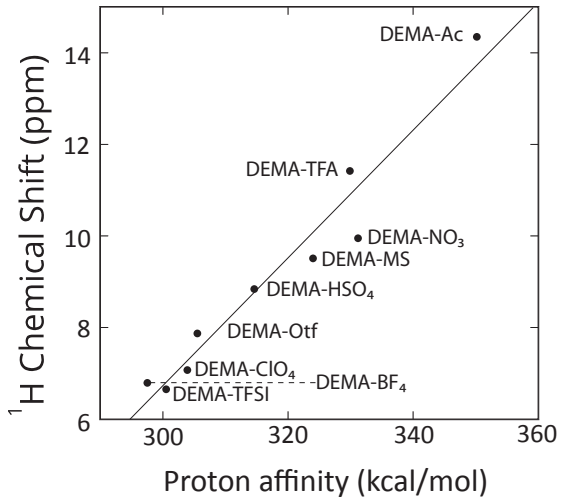

Figure 3.3. Chemical shift of the exchangeable proton for an array of DEMA based protic ionic liquids correlated with the proton affinity of the acid used to generate the PIL. The proton affinities in this plot were obtained by calculating the proton affinity of each acid using Gaussian09 to perform DFT-B3LYP with the basis set 6-31G (d). The equation for the trend line shown is δ=0.14*PA-35.11.

A way to classify the strengths of acids, which does not rely on their activity in a solvent, is by determining their gas phase proton affinity using electronic structure calculations. Proton affinities were calculated by obtaining the ΔH of the protonation of the anions; this reaction scheme is shown in eq 2:

$$A^-_{(g)} + H^+_{(g)} \rightarrow AH_{(g)} \qquad (2)$$

The lower the proton affinity of an anion, the stronger the associated acid. Similar gas phase ab initio calculation studies have been a focus of recent publications estimating the acidity of superacids.[32,33] A plot correlating the gas phase proton affinity for each anion and the chemical shift of the exchangeable proton upon reaction with the base DEMA is shown in Figure 3. The stronger acids will have lower proton affinities, resulting in the exchangeable proton forming a stronger bond to the amine of the base. This increased interaction with the lone pair of the nitrogen on the base results in the chemical shift of the exchangeable proton shifting upfield (to lower ppm). The good correlation between the gas phase proton affinities and exchangeable proton chemical shifts implies that this is a better predictor of the extent of proton transfer than is the ΔpK_a value. Furthermore, this method could be used to interpolate a proton affinity for an acid of unknown strength for a facile method of acidity determination. The practice of correlating proton affinity to chemical shift is one that has been used extensively to determine the acidity of solid acid catalysts.[34,35] In some cases, d_5-pyridine has been used to form hydrogen bonds with the acid sites of the material, and the ^1H chemical shift of the proton which is hydrogen-bonded to they nitrogen on the pyridine is used to determine the proton affinity of the acid sites in the solid.[36] A correlation between acid proton affinity and the chemical shift of exchangeable proton has also been observed in a set of PILs generated with a base of

considerably different basicity, 1,3-Dimethyl-2-imidazolidinone (DMI), see Figure S2. This set of ionic liquids will be the focus of a separate publication from our group, however this observation demonstrates that this correlation is not unique to PILs generated using simple amines as bases.

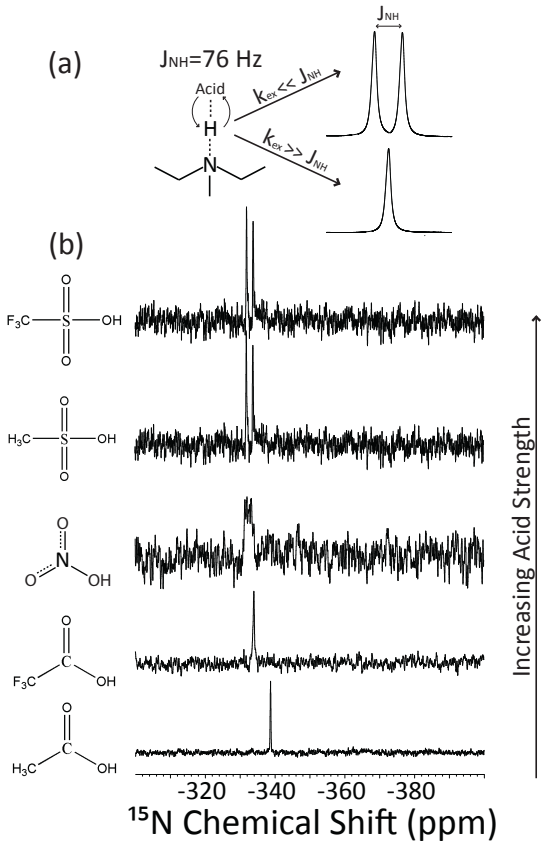

Figure 3.4. (a) The schematic representation of a DEMA based ionic liquid in exchange and an example splitting pattern for the case of fast and slow exchange. (b) ^{15}N NMR spectra for an array of DEMA based Ionic liquids collected without ^{1}H decoupling to allow for the observation of J_{NH}.

Details about the extent of proton transfer as a function of acid strength can be elucidated using ^{15}N NMR. Natural abundance ^{15}N NMR is possible on neat ionic liquids due to the high concentration of the DEMA cation. A series of ^{15}N NMR spectra were collected for the set of DEMA based ionic liquids without ^{1}H decoupling to observe the

J_{NH} coupling, and these spectra are shown in Figure 3.4. As the acid strength increases, the exchangeable proton is more associated with the nitrogen of the base, resulting in a shift of the ^{15}N resonance down field (higher ppm). This shift is consistent with previous studies which measured the ^{15}N chemical shift of amines as a function of the extent of protonation.[13,20] Furthermore, when the acid used to generate the PIL is stronger than nitric acid the J_{NH} coupling (76Hz) is clearly observed. In the weak acid case, the exchangeable proton is exchanging faster than the timescale of the ^{15}N NMR measurement, resulting in the observation of a singlet. In the intermediate case (DEMA-NO_3) a peak broadened by exchange is observed, reminiscent of temperature-induced coalescence.[37] The observation of the J_{NH} splitting in ionic liquids made with acids stronger than nitric acid implies that the proton exchange in these PILs is slower than the time scale associated with the observed J_{NH}. Additionally, the observation of a singlet for the ionic liquids synthesized with acids weaker than nitric acid implies that the rate of exchange is faster than the time scale associated with the J_{NH}. PILs formed with weak proton transfers seem to have properties more similar to molecular liquids, such as an appreciable vapor pressure.[38] The observation of these properties is consistent with the claim that these latter ionic liquids have a low ionicity.

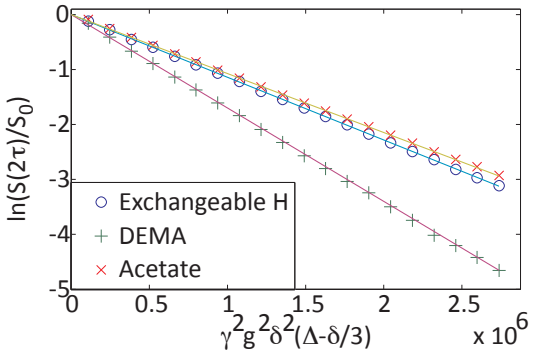

Figure 3.5. Example Stejskal-Tanner plot obtained from PFG-NMR experiments for DEMA-Ac protic ionic liquid using the stimulated echo sequence with bipolar gradients.

Pulsed field gradient stimulated echo (PFG-STE) NMR can be used to measure the transport properties of ionic liquids, and thereby provide information about the extent of proton transfer.[39] This pulse sequence was used instead of the spin echo (SE) pulse sequence[40] because the magnetization during the diffusion delay relaxes according to T_1 instead of T_2. T_1 relaxation is typically slower than T_2 relaxation in liquids, resulting in the PFG-STE sequence having better sensitivity than the PFG-SE version. Furthermore, bipolar gradient pulses were implemented to limit eddy-current effects. Using this technique, it is possible to determine the diffusion coefficient of the cation, anion, and exchangeable proton simultaneously, if each is NMR active. To determine the diffusion coefficients, the decrease in area of each peak as a function of gradient strength was fit with the Stejskal-Tanner[41,42] equation:

$$\ln(S(2\tau)/S_0) = -Dg^2\gamma^2\delta^2(\Delta - \frac{\delta}{3}) \qquad (3)$$

where $S(2\tau)$ is the attenuated signal, $S(0)$ is the signal with zero gradient strength, g is the gradient strength, γ is the gyromagnetic ratio, δ is the gradient length, and Δ is the diffusion delay. An example of a diffusion NMR analysis result is shown in the Stejskal-

Tanner plot of Figure 3.5. Resonances that are associated with molecules which possess a larger diffusion coefficient will have a steeper slope in the plot. Based on the similarity of the diffusion coefficients of the anion and the exchangeable proton, they can be considered to be diffusing together. Observation of the exchangeable proton diffusing at a similar rate to the Ac anion indicates that there is a weak proton transfer from the acid to the base in DEMA-Ac and that this ionic liquid has a low ionicity. A summary of the diffusion NMR results is shown below in Table 2. For the PIL with the strongest acid (DEMA-Otf), the diffusion coefficient of the exchangeable proton closely matches the cation, indicating that this PIL has a high ionicity. For the two moderately ionic PILs, the anion, cation and exchangeable proton appeared to be diffusing at the same rate. This similarity in diffusion coefficient could indicate that the cation and anion are diffusing as hydrogen bonded ion pairs.

Table 3.1. Results of diffusion NMR experiments and conductivity measurements. Diffusion coefficients are shown as $D*10^9$ (m^2/s) and conductivities are all reported in mS.

	D^-	D^H	D^+	L_{NE}	L_{exp}	L_{exp}/L_{NE}
DEMA-Ac	8.46	9.03	13.1	49.5	2.72	0.055
DEMA-TFA	3.90	3.93	3.97	16.0	3.69	0.231
DEMA-MS	2.48	2.46	2.45	10.7	3.55	0.332
DEMA-Tf	1.91	4.40	4.35	12.5	7.69	0.615

Quantifying the ionicity of protic ionic liquids and establishing trends is important for the prediction of the properties of ionic liquids. To quantify ionicity, results of the diffusion NMR experiments can be used to calculate the ideal Nernst Einstein conductivity using the following equation:

$$\Lambda_{NE} = \frac{N_A e^2}{kT}(D^+ + D^-) \qquad (4)$$

where Λ_{NE} is the ionic conductivity predicted via PFG-NMR, N_A is the Avogadro number, e is the electronic charge, k is Boltzmann's constant, T is temperature, D^+ and D^- are the measured diffusion coefficients of the cation and anion respectively. The ratio of this ionic conductivity and the experimentally measured ionic conductivity from an impedance experiment is related to the ionicity of the ionic liquid.

Additionally, the deviation from the ideal viscosity limited Walden conductivity (ΔW) can be used as a measure of ionicity.[8,11,12,16] The ΔW is calculated by correlating the log of equivalent conductivity with the log of fluidity for an ionic liquid and comparing it to the ideal case for conductivity of 1 M KCl.[8,11] A plot summarizing the characterization of the ionicity of a subset of the ionic liquids using these two methods is shown in Figure 3.6. The two different measures of ionicity are in good agreement, as was also found by Miran et al. for the case of a series of acids protonating the super base 1,8-diazabicyclo-[5,4,0]-undec-7-ene (DBU). However, the data point for the most ionic IL analyzed (DEMA-Otf) deviates from linearity, which indicates a difference between these two methods for determining ionicity as the ionic liquid approaches higher ionicities. The inability of an ionic liquid's conductivity to approach the ideal Nernst-Einstein conductivity has previously been attributed to the effects from ion-pair diffusion.[12,43] PFG-NMR results for the PILs with intermediate proton transfer strengths showed the cation and anion diffusing at approximately the same rate, which supports the presence of ion-pairing (see Table 3.1). However, for the strong proton transfer case (DEMA-Otf), different diffusion rates were observed for the anion and cation, suggesting

that ion pairing is not prominent for this PIL. In cases where ion-pairing is not expected, the deviation from the Nernst-Einstein conductivity can be attributed to interionic friction as described previously for molten salts by Berne and Rice.[44]

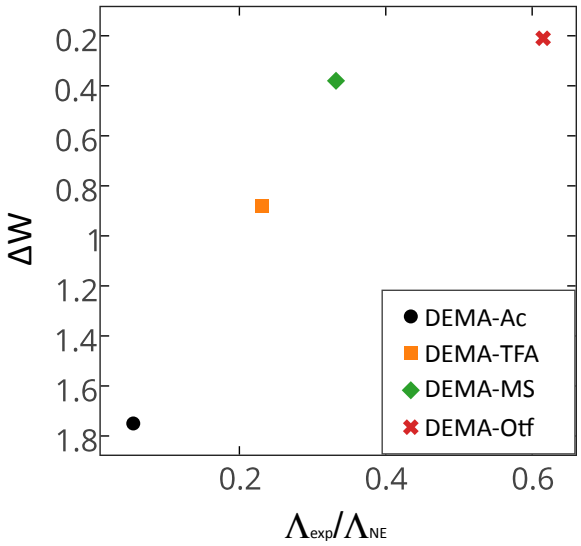

Figure 3.6. Summary of the characterization of the ionicity of a subset of the DEMA based ionic liquids studied via the deviation from Walden conductivity (ΔW) and the ratio of the measured conductivity through impedance measurements, and the predicted conductivity from NMR ($\Lambda_{exp}/\Lambda_{NE}$).

3.4 Conclusions

The ionicities of several liquids in a set of DEMA based PILs were characterized using NMR spectroscopy, electronic structure calculations, and conductivity measurements. The chemical shift of the exchangeable proton for each PIL was observed to have a linear relationship with the gas phase proton affinity of the acid. Consequently, our results show that proton affinity is a better predictor of ionicity than aqueous ΔpKa values. Furthermore, diffusion results indicated that the exchangeable proton diffuses primarily with the anion in weakly ionic PILs (DEMA-Ac), while in strongly ionic PILs (DEMA-Otf) it diffuses with the cation. To predict the ionicity of a more general set of

ionic liquids, the difference in the proton affinity of the acid and the proton affinity of the base (ΔPA) can be used. Some data collected by our group for a set of DMI based ionic liquids indicates that this is a general trend (see Figure 3.8).

3.5 Supplementary Material

The figures below are provided as supplementary figures to Chapter 3.

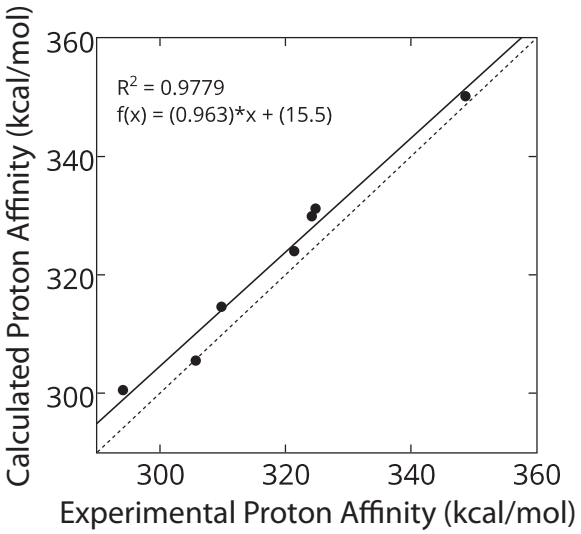

Figure 3.7 Gas phase proton affinity values obtained via electronic structure calculations carried out at the DFT-B3LYP level of theory with a basis set of 6-31G(d) compared to values obtained from the literature. The solid line is a fit of the data points, and the dotted line is along y=x.

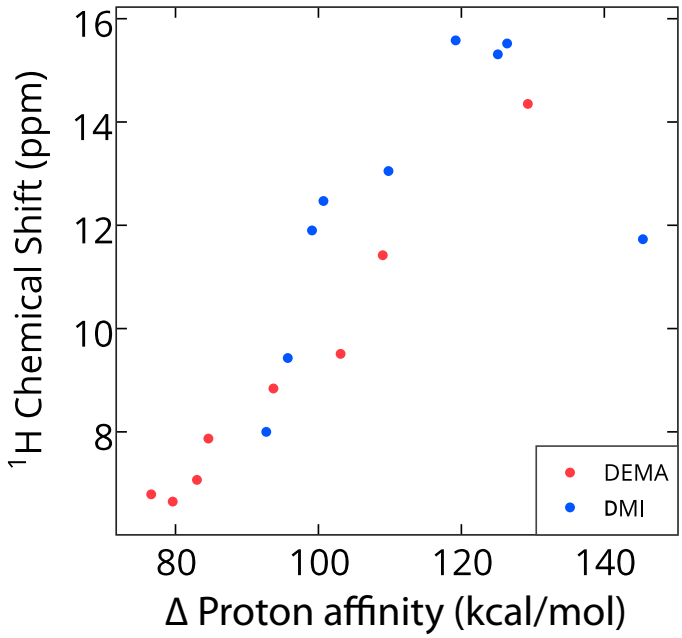

Figure 3.8 Plot exemplifying the relation of the exchangeable proton's chemical shift in protic ionic liquids (PILs) with the different in the proton affinity of the acid and base (ΔPA) used to generate the PIL. The data is shown for 2 sets of PILs made with the bases diethylmethylamine (DEMA) and 1,3-Dimethyl-2-imidazolidinone (DMI).

3.6 References

(1) Inoue, D.; Mitsushima, S.; Matsuzawa, K.; Lee, S.-Y.; Yasuda, T.; Watanabe, M.; OTA, K.-I. A Mesothermal Fuel Cell Using Diethylmethylammonium Trifluoromethanesulfonate Absorbed Membrane with H3PO4 Addition and Various Amount of Electrolyte Loading in Catalyst Layer. *Electrochemistry* **2011**, *79*, 377–380.

(2) Lee, S. Y.; Yasuda, T.; Watanabe, M. Fabrication of Protic Ionic Liquid/Sulfonated Polyimide Composite Membranes for Non-Humidified Fuel Cells. *J. Power Sources* **2010,** *195,* 5909-5914.

(3) Mitsushima, S.; Shinohara, Y.; Matsuzawa, K.; Ota, K. Mass Transportation in Diethylmethylammonium Trifluoromethanesulfonate for Fuel Cell Applications. *Electrochimica Acta* **2010,** *55,* 6639-6644.

(4) Li, H.; Jiang, F.; Di, Z.; Gu, J. Anhydrous Proton-Conducting Glass Membranes Doped with Ionic Liquid for Intermediate-Temperature Fuel Cells. *Electrochimica Acta* **2012**, *59*, 86–90.

(5) Li, Q.; He, R.; Ronghuan He; Jens Oluf Jensen, A.; Bjerrum, N. J. Approaches and Recent Development of Polymer Electrolyte Membranes for Fuel Cells Operating Above 100 °C. *Chem. Mater.* **2003**, *15*, 4896–4915.

(6) Binary Inorganic Salt Mixtures as High Conductivity Liquid Electrolytes for >100 ºC Fuel Cells. **2006**, 4799–3.

(7) Miran, M. S.; Yasuda, T.; Susan, M. A. B. H.; Dokko, K.; Watanabe, M. Binary Protic Ionic Liquid Mixtures as a Proton Conductor: High Fuel Cell Reaction Activity and Facile Proton Transport. **2014**, *118*, 27631–27639.

(8) Xu, W.; Angell, C. A. Solvent-Free Electrolytes with Aqueous Solution-Like Conductivities. *Science* **2003**, *302*, 422–425.

(9) Menne, S.; Pires, J.; Anouti, M.; Balducci, A. Protic Ionic Liquids as Electrolytes for Lithium-Ion Batteries. *Electrochemistry Communications* **2013,** *31,* 39-41.

(10) Greaves, T. L.; Drummond, C. J. Protic Ionic Liquids: Properties and Applications. *Chem. Rev.* **2008**, *108*, 206–237.

(11) Yoshizawa, M.; Xu, W.; Angell, C. A. Ionic Liquids by Proton Transfer: Vapor Pressure, Conductivity, and the Relevance of Δp Kafrom Aqueous Solutions. *J. Am. Chem. Soc.* **2003**, *125*, 15411–15419.

(12) Macfarlane, D. R.; Forsyth, M.; Izgorodina, E. I.; Abbott, A. P.; Annat, G.; Fraser, K. On the Concept of Ionicity in Ionic Liquids. *Phys. Chem. Chem. Phys.* **2009**, *11*, 4962–4967.

(13) Burrell, G. L.; Burgar, I. M.; Separovic, F.; Dunlop, N. F. Preparation of Protic Ionic Liquids with Minimal Water Content and (15)N NMR Study of Proton Transfer. *Phys. Chem. Chem. Phys.* **2010**, *12*, 1571–1577.

(14) Sarmini, K.; Kenndler, E. Ionization Constants of Weak Acids and Bases in Organic Solvents. *Journal of Biochemical and Biophysical Methods* **1999**, *38*, 123–137.

(15) Bordwell, F. G. Equilibrium Acidities in Dimethyl Sulfoxide Solution. *Acc. Chem. Res.* **1988**, *21*, 456–463.

(16) Belieres, J.-P.; Angell, C. A. Protic Ionic Liquids: Preparation, Characterization, and Proton Free Energy Level Representation. *J. Phys. Chem. B* **2007**, *111*, 4926–4937.

(17) Noda, A.; Susan, M. A. B. H.; Kudo, K.; Mitsushima, S.; Hayamizu, K.; Watanabe, M. Brønsted Acid−Base Ionic Liquids as Proton-Conducting Nonaqueous Electrolytes. *J. Phys. Chem. B* **2003**, *107*, 4024–4033.

(18) Nuthakki, B.; Greaves, T. L.; Krodkiewska, I.; Weerawardena, A.; Burgar, M. I.; Mulder, R. J.; Drummond, C. J. Protic Ionic Liquids and Ionicity. *Australian Journal of Chemistry* **2007**, *60*, 21–28.

(19) Blanchard, J. W.; Belieres, J.-P.; Alam, T. M.; Yarger, J. L.; Holland, G. P. NMR Determination of the Diffusion Mechanisms in Triethylamine-Based Protic Ionic Liquids. *J. Phys. Chem. Lett.* **2011**, *2*, 1077–1081.

(20) Judeinstein, P.; Iojoiu, C.; Sanchez, J.-Y.; Ancian, B. Proton Conducting Ionic Liquid Organization as Probed by NMR: Self-Diffusion Coefficients and Heteronuclear Correlations. *J. Phys. Chem. B* **2008**, *112*, 3680–3683.

(21) Iojoiu, C.; Judeinstein, P.; Sanchez, J. Y. Ion Transport in CLIP: Investigation Through Conductivity and NMR Measurements. *Electrochimica Acta* **2007** *53*, 1395-1403.

(22) Iojoiu, C.; Martinez, M.; Hanna, M.; Molmeret, Y.; Cointeaux, L.; Leprêtre, J.-C.; Kissi, N. E.; Guindet, J.; Judeinstein, P.; Sanchez, J.-Y. PILs-Based Nafion Membranes: a Route to High-Temperature PEFMCs Dedicated to Electric and Hybrid Vehicles. **2008**, *19*, 1406–1414.

(23) Mori, K.; Hashimoto, S.; Yuzuri, T.; Sakakibara, K. Structural and Spectroscopic Characteristics of a Proton-Conductive Ionic Liquid Diethylmethylammonium Trifluoromethanesulfonate [Dema][TfOH]. **2010**, *83*, 328–334.

(24) Mori, K.; Kobayashi, T.; Sakakibara, K.; Ueda, K. Experimental and Theoretical Investigation of Proton Exchange Reaction Between Protic Ionic Liquid Diethylmethylammonium Trifluoromethanesulfonate and H_2O. *Chem. Phys. Lett.* **2012,** *552,* 58-63.

(25) Römich, C.; Merkel, N. C.; Valbonesi, A.; Schaber, K.; Sauer, S.; Schubert, T. J. S. Thermodynamic Properties of Binary Mixtures of Water and Room-Temperature Ionic Liquids: Vapor Pressures, Heat Capacities, Densities, and Viscosities of Water + 1-Ethyl-3-Methylimidazolium Acetate and Water + Diethylmethylammonium Methane Sulfonate. **2012**, *57*, 2258–2264.

(26) Wu, D. H.; Chen, A. D.; Johnson, C. S. An Improved Diffusion-Ordered Spectroscopy Experiment Incorporating Bipolar-Gradient Pulses. *J. Magn. Reson., Ser A* **1995**, *115*, 260–264.

(27) Frisch, M. J.; Trucks, G. W.; Schlegel, H. B.; Scuseria, G. E.; Robb, M. A.; Cheeseman, J. R.; Scalmani, G.; Barone, V.; Mennucci, B.; Petersson, G. A.; et al. Guassian 09.

(28) Miran, M. S.; Kinoshita, H.; Yasuda, T.; Susan, M. A. B. H.; Watanabe, M. Hydrogen Bonds in Protic Ionic Liquids and Their Correlation with Physicochemical Properties. *Chem. Commun.* **2011**, *47*, 12676–12678.

(29) Denisov, G. S.; Gindin, V. A.; Golubev, N. S.; Ligay, S. S.; Shchepkin, D. N.; Smimov, S. N. NMR Study of Proton Location in Strongly Hydrogen Bonded Complexes of Pyridine as Influenced by Solvent Polarity. *J. Mol. Liq.* **1995**, *67*, 217–234.

(30) Kütt, A.; Rodima, T.; Saame, J.; Raamat, E.; Mäemets, V.; Kaljurand, I.; Koppel, I. A.; Garlyauskayte, R. Y.; Yagupolskii, Y. L.; Yagupolskii, L. M.; et al. Equilibrium Acidities of Superacids. *J. Org. Chem.* **2011**, *76*, 391–395.

(31) Raamat, E.; Kaupmees, K.; Ovsjannikov, G.; Trummal, A.; Kütt, A.; Saame, J.; Koppel, I.; Kaljurand, I.; Lipping, L.; Rodima, T.; et al. Acidities of Strong Neutral Brønsted Acids in Different Media. *J. Phys. Org. Chem.* **2012**, *26*, 162–170.

(32) Gutowski, K. E.; Dixon, D. A. Ab Initio Prediction of the Gas- and Solution-Phase Acidities of Strong Brønsted Acids: the Calculation of pKa Values Less Than −10. *J. Phys. Chem. A* **2006,** 12044-12054.

(33) Zhang, M.; Sonoda, T.; Mishima, M.; Honda, T.; Leito, I.; Koppel, I. A.; Bonrath, W.; Netscher, T. Gas-Phase Acidity of Bis[(Perfluoroalkyl)Sulfonyl]Imides. Effects of the Perfluoroalkyl Group on the Acidity. *J. Phys. Org. Chem.* **2014**, *27*, 676–679.

(34) Zheng, A.; Liu, S.-B.; Deng, F. Acidity Characterization of Heterogeneous Catalysts by Solid-State NMR Spectroscopy Using Probe Molecules. *Solid-State Nucl. Magn. Reson.* **2013**, *55-56*, 12–27.

(35) Yi, D.; Zhang, H.; Deng, Z. 1H and 15N Chemical Shifts of Adsorbed Acetonitrile as Measures to Probe the Brønsted Acid Strength of Solid Acids: a DFT Study. *Journal of Molecular Catalysis A: Chemical* **2010**.

(36) Chen, T.-H.; Wouters, B. H.; Grobet, P. J. Enhanced Resolution of Aluminum and Proton Sites in the Molecular Sieve SAPO-37 by 27Al Multiple Quantum Magic Angle Spinning and 1H Spin Echo Editing NMR. *J. Phys. Chem. B* **1999**, *103*, 6179–6184.

(37) Ross, B. D.; True, N. S. Gas-Phase Carbon-13 NMR Spectra and Exchange Kinetics of N,N-Dimethylformamide - Journal of the American Chemical Society (ACS Publications). *J. Am. Chem. Soc.* **1984**.

(38) Angell, C. A.; Byrne, N.; Belieres, J.-P. Parallel Developments in Aprotic and Protic Ionic Liquids: Physical Chemistry and Applications. *Acc. Chem. Res.* **2007**, *40*, 1228–1236.

(39) Burrell, G. L.; Burgar, I. M.; Gong, Q.; Dunlop, N. F.; Separovic, F. NMR Relaxation and Self-Diffusion Study at High and Low Magnetic Fields of Ionic Association in Protic Ionic Liquids. *J. Phys. Chem. B* **2010**, *114*, 11436–11443.

(40) Tanner, J. E. Pulsed Field Gradients for NMR Spin-Echo Diffusion Measurements. *Rev. Sci. Instrum.* **1965**, *36*, 1086–1087.

(41) Stejskal, E. O.; Tanner, J. E. Browse - Journal of Chemical Physics. *J. Chem. Phys.* **1965**, *42*, 288–292.

(42) Tanner, J. E.; Stejskal, E. O. Restricted Self‐Diffusion of Protons in Colloidal Systems by the Pulsed‐Gradient, Spin‐Echo Method. *J. Chem. Phys.* **1968**, *49*, 1768–1777.

(43) Ueno, K.; Tokuda, H.; Watanabe, M. Ionicity in Ionic Liquids: Correlation with Ionic Structure and Physicochemical Properties. *Phys. Chem. Chem. Phys.* **2010**, *12*, 1649.

(44) Berne, B.; Rice, S. A. On the Kinetic Theory of Dense Fluids. XVI. The Ideal Ionic melt. *J. Chem. Phys.* **1964,** *40,* 1347-1362.

Chapter 4

Investigating the diffusion of small molecules in aqueous media using PFG-NMR and molecular dynamics

4.1 Introduction

The diffusion of molecules in the liquid phase is of substantial importance to many physical, chemical, and biological processes. Diffusion of molecules in a system can be the limiting factor for the rate of chemical reactions, and can play a significant role in the details of bimolecular interactions. Characterizing the diffusion of molecules in a system has been used extensively in the determination of the extent of oligomerization of proteins,[1] and to characterize the molecular weight distributions of polymer solutions.[2] Additionally, the self-diffusion of molecules can be used to approximate their viscosity via the Stokes-Einstein equation.[3] Here we present a pulsed field gradient nuclear magnetic resonance (PFG-NMR) experiment, coupled with molecular dynamics simulations, which can be used to determine the diffusion coefficients of small molecules in aqueous media experimentally and computationally.

One of the most direct and accurate ways to measure the diffusion of molecules is by using PFG-NMR.[4] This technique involves applying a magnetic field gradient along the z-axis of the sample, resulting in the nuclear spins experiencing a magnetic field based on their location. This is referred to as the spatial encoding gradient, because the spins are "encoded" with their location by this gradient pulse. Subsequently, a diffusion delay period occurs, during which the molecules undergo diffusion. After the diffusion delay is complete, a second gradient pulse is applied to the sample of equal strength and length but of effectively opposite sign. This second gradient's purpose is to refocus the

dephasing of the magnetization caused by the spatial encoding gradient. Therefore, in the absence of any diffusion the refocusing gradient will counteract the dephasing caused by the encoding gradient and the ideal signal will be observed for the nuclei. However, in the presence of diffusion, the signal observed will be attenuated in a manner that depends on how far the spin has moved along the z-axis during the diffusion delay. Furthermore, the signal decrease depends on the diffusion coefficient of the molecule. The observed signal attention is dictated by the Stejskal-Tanner equation:[5]

$$\ln(S(2\tau)/S_0) = -Dg^2\gamma^2\delta^2(\Delta - \frac{\delta}{3}) \qquad (1)$$

Where $S(2\tau)$ is the signal observed in the experiment, S_0 is the signal observed in the absence of any gradient strength, g is the gradient strength, γ is the gyromagnetic ratio for the observed nucleus, δ is the gradient length, Δ is the diffusion delay, and D is the diffusion coefficient. The full derivation of the Stejskal-Tanner equation can be found here.[6] To collect this data the stimulated echo (STE) PFG pulse sequence[7] was used. The STE-PFG NMR pulse sequence is shown in Figure 1 (B) along with the simpler spin echo (SE) PFG sequence for comparison, shown in Figure 1 (A).

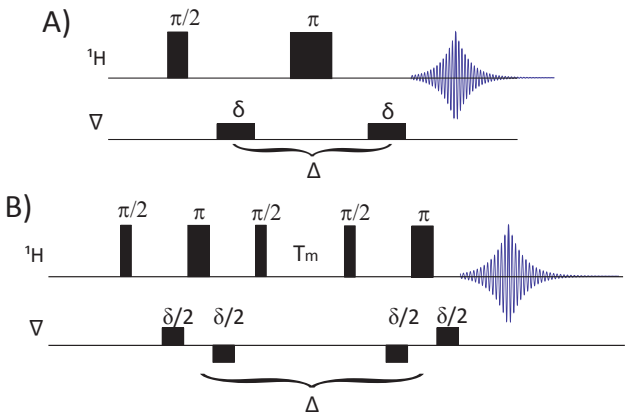

Figure 4.1. Schematic diagram of the pulse sequences commonly used to determine diffusion coefficients via NMR. The spin echo pulsed field gradient (SE-PFG) sequence[13] (A) and the stimulated echo pulsed field gradients (STE-PFG) sequence with bipolar gradients[7] (B).

Molecular dynamics (MD) simulations involve the numerical calculation of forces between, and the movement of, atoms in a system as a function of time.[8] Simply put, the simulation calculates the forces exerted on each atom by the surrounding atoms and moves the atoms according to classical equations of motion. To calculate the forces exerted on each atom, a force field is used to approximate the bonding and non-bonding interactions between the atoms in the system.[9] The equations of motion for the atoms are then integrated over small (typically 1 fs), finite time steps (Δt). There are many methods for executing the calculations,[8] but a simple example is the Verlet algorithm,[10] which is shown below in Equation 2:

$$x(t+\Delta t) = 2x(t) - x(t-\Delta t) + \frac{d^2x(t)}{dt^2}\Delta t^2 \qquad (2)$$

This equation can be used to calculate the position of the atom at the next time step (x(t+Δt)) using the current location of the atom (x(t)), the position of the atom at the previous time step (x(t-Δt)) and the acceleration of the atom at time t ($d^2x(t)/dt^2$). More

complicated versions of this algorithm are typically implemented,[11] but this simple algorithm is a good example for teaching purposes. To determine the diffusion coefficient (D) of a molecule in a MD simulation, the mean squared displacement ($\langle \Delta r(\tau)^2 \rangle$) as a function of lag time (τ) is calculated from the trajectory and used along with the dimensionality of the system (n) in the following equation:[12]

$$\left\langle \Delta r(\tau)^2 \right\rangle = 2nD\tau \qquad (3)$$

4.2 Experimental

Materials. The 99.9% D_2O was obtained from Cambridge Isotopes Laboratories. Solutes were obtained from Sigma-Aldrich and used as received.

Sample preparation. Samples for diffusion NMR experiments were generated by dissolving approximately 1 wt.% of each solute in 99.9% D2O and pipetting approximately 700 μL of the solution into a 5 mm NMR tube.

NMR data collection. ^{1}H stimulated echo pulsed field gradient (STE-PFG) NMR spectra were collected using a 500 MHz Varian VNMRS spectrometer equipped with a 5mm ^{1}H-^{13}C-^{15}N probe capable of an approximately 70 G/cm pulsed field gradient strength at maximum power. Spectra were collected using the stimulated echo sequence[7] with bipolar gradients as shown in Figure 4. 1 B. Primary NMR parameters used in the collection of this data were a recycled delay of 5 seconds, a diffusion delay of 60 ms, and a gradient length of 1.0 ms. The gradient strength was varied from approximately 2.5 G/cm to 70 G/cm averaging 8 transients at each gradient strength. During data collection, the temperature of the probe was regulated at 25.0 ºC. The gradient strength of the probe calibrated using a sample of 99.9% D_2O, which has a well characterized diffusion

coefficient of 1.872×10^{-9} m^2/s.[13] The ^1H chemical shifts were referenced by setting the chemical shift of the residual HOD in the D_2O to 4.8 ppm.

Molecular dynamics simulations. All MD simulations were carried out using the program NAMD (version 2.10),[14] and prepared/visualized using VMD 1.9.1.[15] Cubic simulation cells with periodic boundary conditions were used. The cubic simulation cells had a volume of 216,000 $Å^3$ (each side was 60 Å). Simulation cells were populated with the molecule of interest in the center, along with approximately 6,000 water molecules, which were represented with the TIP3P potential function.[16] Each system was energy minimized for 200 steps prior to carrying out the MD simulation for 200 ps, with a time step of 1 fs. The temperature of each system was regulated at 298 K using Langevin dynamics,[17] and the pressure was regulated at 1 atm using the Langevin piston method,[18] both of which are standard methods implemented by NAMD. The CHARM general force field (CGenFF) [19,20] was used for the calculation of forces. MSDs were obtained from the trajectories either using the tcl script supplied in the supporting information, or by using the diffusion plug-in for VMD. Each simulation was completed in approximately 4 hours using the quad-core 2.8 GHz central processing unit (CPU) of an imac computer.

Hazards. The solutes are all common laboratory reagents/solvents, and should be handled using gloves. Benzene is a known carcinogen, so efforts to minimize exposure should be taken. Dioxane has a tendency to form peroxides, which can be explosive, so routine peroxide tests should be carried out on bottles of this reagent. NMR spectrometers produce large magnetic fields, so any students with medical implants or pacemakers should not work with them.

4.3 Results and discussion

A typical trajectory result from an MD simulation, visualized using VMD, is shown in Figure 2. The acetone molecule is shown as a function of simulation time with the structure's color corresponding to the time step (red→blue is increasing time). The molecules do not follow any set path, presenting a good example of Brownian motion.

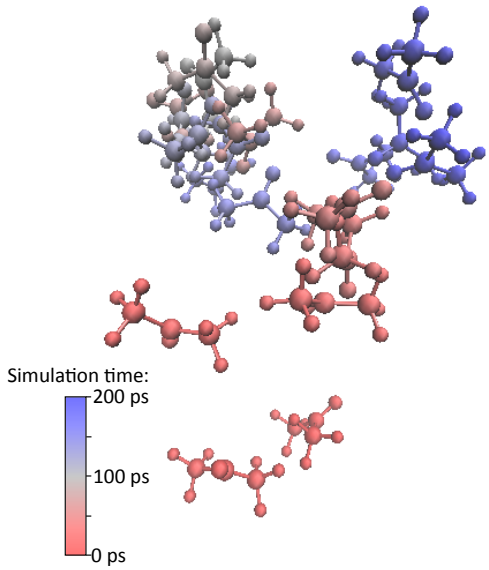

Figure 4.2. Molecular dynamics trajectory for acetone diffusing through a collection of water molecules over the course of 200 ps. The colors of the ball and stick models represent their time-step red→blue is increasing time.

It has been shown that the accuracy of the diffusion coefficient extracted from MD trajectories can be greatly improved by averaging the results from multiple simulations.[12] This strategy was utilized to obtain diffusion coefficients with acceptable accuracy without needing extremely long simulation times and large simulation cells. A plot of the 20 of the trajectories from MD simulations with the same starting conditions is shown in Figure 4.3. The circles on this plot represent the average values for the MSD at each lag time. The large deviation from the mean is typical, due to the nature of

Brownian motion on these relatively short timescales.[12] Fitting these data with a line allows for the calculation of the diffusion coefficient utilizing Equation 3. This same analysis was done for each of the 10 solutes shown in the study, and the resultant average trajectories are shown in Figure 4.4. The Diffusion coefficient is directly related to the slope of the trend these data follow, as seen in Equation 3. Therefore, the solutes that have an MSD which rises more quickly with lag time, qualitatively have a larger diffusion coefficient. In general the trend observed of relatively diffusivities observed via the MD simulations in consistent with literature values. The Diffusion coefficients obtained from fitting these data are shown in Table 4.1.

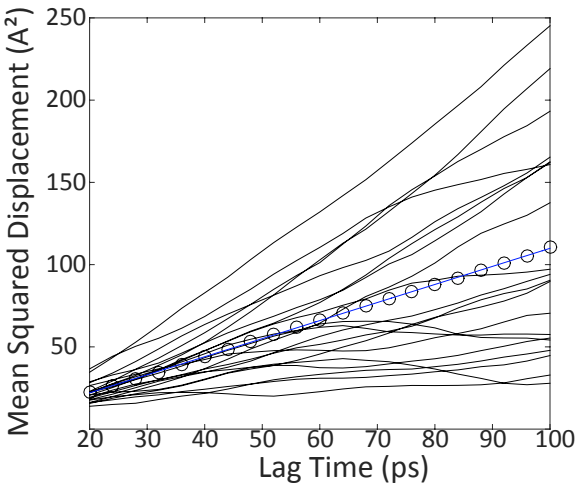

Figure 4.3. Molecular dynamics trajectories for 20 simulations of acetone in TIP3P water. The circles represent the average MSD at each lag time.

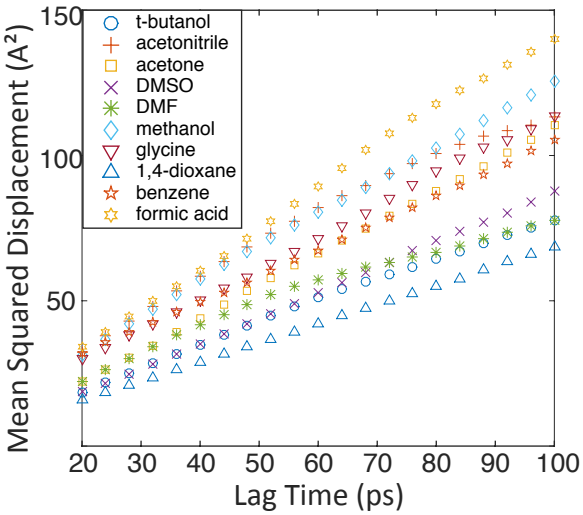

Figure 4.4. Average of 20 molecular dynamics trajectories for each of the solutes in water.

A ^{1}H NMR spectrum for the mixture of molecules dissolved in D_2O is shown in Figure 4.5. The solutes in this mixture are all at a concentration of approximately 20 μM. The chemical shifts for each of the molecules are shown in Table 4.1. The resonances for the solutes are all well resolved in the spectrum, allowing for simple quantification. The simple small molecules used in this study have resonances in the ^{1}H spectrum which are singlets. This lack of J-coupling allows for the integration of peak areas to be carried out more easily.

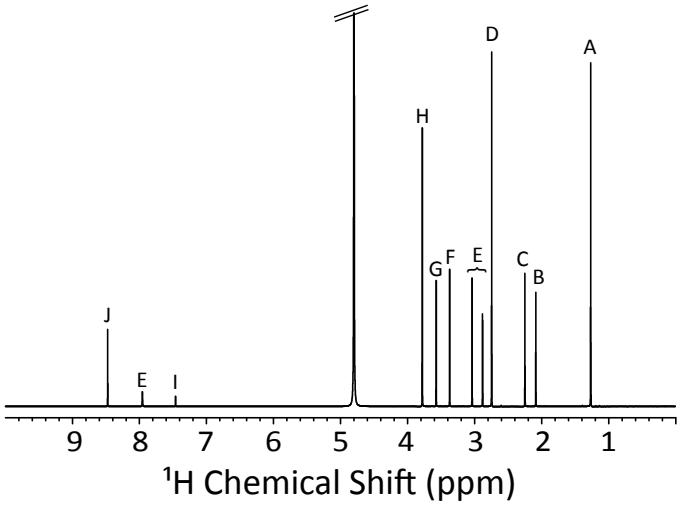

Figure 4.5. ^{1}H NMR spectrum of the mixture of solutes in D_2O at approximately 20 μM. The resonances in the spectrum have been assigned to (A) t-butanol, (B) acetonitrile, (C) acetone, (D) DMSO, (E) DMF, (F) methanol, (G) glycine, (H) 1,4-dioxane, (I) benzene, (J) formic acid.

Pulsed field gradient (PFG) NMR can be used to determine the diffusion coefficients of NMR active molecules in a mixture simultaneously.[4] PFG-NMR was implemented in this study to characterize the diffusivity of the molecules in the well-resolved spectrum shown in Figure 4.5. A Stejskal-Tanner plot from the PFG-NMR experiment conducted in this study is shown in Figure 4.6. The Signal decay as a function of gradient strength was fit with Equation 1. Signals which decay more quickly with gradient strength are associated with molecules which have higher diffusion coefficients. The results of the PFG-NMR analysis are shown in Table 4.1. In general, the numbers are in good agreement with literature values. The diffusivities are all lower than expected based on literature; this could be due to solute-solute interactions present at 20 uM concentration.

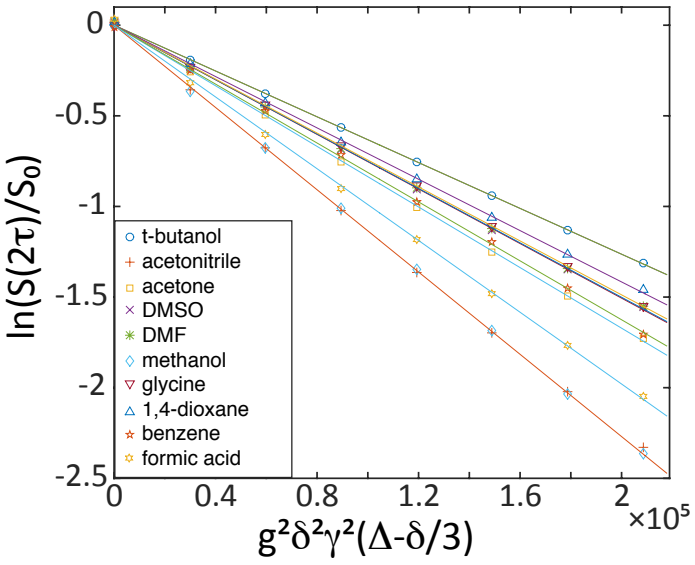

Figure 4.6. Stejskal-Tanner plot for each of the solutes diffusing through D_2O.

4.4 Conclusions

The diffusion coefficients of an array of small molecules in an aqueous media were determined experimentally and computationally, using pulsed field gradient (PFG) NMR and molecular dynamics (MD) simulations respectively. Coupling experimental results with simulation results has allowed students to more meaningfully interpret data from complex experiments such as PFG-NMR. Furthermore, MD simulations allow students to better understand and visualize the time and length-scale of molecular diffusion in liquids. The PFG-NMR experiment allowed for the accurate determination of the diffusion coefficient associated with each molecule in an aqueous solution. Diffusion coefficients obtained using this method were in good agreement with literature values. MD simulations were employed to determine the diffusion coefficients of the same molecules in a bath of water molecules. By averaging together 20 successive 200 ps simulations for each molecule, more accurate results were obtained, without needing

larger systems. Due to the exponential advances in computational power, MD simulations have become more accessible and common. Therefore, the simulations described here can be run in a reasonable amount of time on modern personal computers (PCs). The data collection for this experiment can be completed in two or three 3-hour lab periods.

Table 4.1. Diffusion Coefficients for the listed small molecules diffusing through H_2O/D_2O obtained using MD and PFG-NMR and compared to literature.

	^{1}H Chemical Shift (ppm)	*MD (m^2/s)*10^9*	*PFG-NMR (m^2/s)*10^9*	*Literature (m^2/s)*10^9*
t-butanol	1.26	1.23	0.60	0.57
acetonitrile	2.08	1.71	1.08	1.26
acetone	2.24	1.82	0.84	1.28
DMSO	2.75	1.45	0.75	0.83
DMF	2.87,3.02,7.94	1.11	0.82	1.12
methanol	3.37	1.93	1.14	1.28
glycine	3.64	1.78	0.74	1.05
1,4-dioxane	3.75	1.29	0.70	1.10
benzene	7.42	1.52	0.81	1.02
formic acid	8.47	2.28	0.99	1.41

4.5 References

(1) Krishnan, V. V. Determination of Oligomeric State of Proteins in Solution From Pulsed-Field-Gradient Self-Diffusion Coefficient Measurements. a Comparison of Experimental, Theoretical, and Hard-Sphere Approximated Values. *J. Magn. Reson.* **1997**, *124*, 468–473.

(2) Chen, A.; Wu, D.; Johnson, C. S. Determination of Molecular Weight Distributions for Polymers by Diffusion-Ordered NMR. *J. Am. Chem. Soc.* **1995**, *117*, 7965–7970.

(3) Li, W.; Kagan, G.; Hopson, R.; Williard, P. G. Measurement of Solution Viscosity via Diffusion-Ordered NMR Spectroscopy (DOSY). *J. Chem. Educ.* **2011**, *88*, 1331–1335.

(4) Tanner, J. E. Pulsed Field Gradients for NMR Spin-Echo Diffusion Measurements. *Rev. Sci. Instrum.* **1965**, *36*, 1086–1087.

(5) Tanner, J. E.; Stejskal, E. O. Restricted Self‐Diffusion of Protons in Colloidal Systems by the Pulsed‐Gradient, Spin‐Echo Method | Browse - Journal of Chemical Physics. *J. Chem. Phys.* **1968**, *49*, 1768–1777.

(6) Kuchel, P. W.; Pagès, G.; Nagashima, K.; Velan, S.; Vijayaragavan, V.; Nagarajan, V.; Chuang, K. H. Stejskal-Tanner Equation Derived in Full. *Concepts Magn. Reson.* **2012**, *40A*, 205–214.

(7) Wu, D. H.; Chen, A. D.; Johnson, C. S. An Improved Diffusion-Ordered Spectroscopy Experiment Incorporating Bipolar-Gradient Pulses. *J. Magn. Reson., Ser A* **1995**, *115*, 260–264.

(8) Adcock, S. A.; McCammon, J. A. Molecular Dynamics: Survey of Methods for Simulating the Activity of Proteins. *Chem. Rev.* **2006**, *106*, 1589–1615.

(9) Wang, J.; Wolf, R. M.; Caldwell, J. W.; Kollman, P. A.; Case, D. A. Development and Testing of a General Amber Force Field. *J Comput Chem* **2004**, *25*, 1157–1174.

(10) Verlet, L. Computer "Experiments" on Classical Fluids. I. Thermodynamical Properties of Lennard-Jones Molecules. *Phys. Rev.* **1967**, *159*, 99–103.

(11) Swope, W. C.; Anderson, H. C.; Berens, P. H.; Wilson, K. R. A Computer Simulation Method for the Calculation of Equilibrium Constants for the Formation of Physical Clusters of Molecules: Application to Small Water Clusters. *J. Chem. Phys.* **1982**, *76*, 637–649.

(12) Wang, J.; Hou, T. Application of Molecular Dynamics Simulations in Molecular Property Prediction II: Diffusion Coefficient. *J Comput Chem* **2011**, *32*, 3505–3519.

(13) Holz, M.; Weingartner, H. Calibration in Accurate Spin-Echo Self-Diffusion Measurements Using 1 H and Less-Common Nuclei. *J. Magn. Reson.* **1991**, *92*, 115–125.

(14) Phillips, J. C.; Braun, R.; Wang, W.; Gumbart, J.; Tajkhorshid, E.; Villa, E.; Chipot, C.; Skeel, R. D.; Kalé, L.; Schulten, K. Scalable Molecular Dynamics with NAMD. *J Comput Chem* **2005**, *26*, 1781–1802.

(15) Humphrey, W.; Dalke, A.; Schulten, K. VMD: Visual Molecular Dynamics. *J Mol Graph* **1996**, *14*, 33–38.

(16) Jorgensen, W. L.; Chandrasekhar, J.; Madura, J. D.; Impey, R. W.; Klein, M. L. Comparison of Simple Potential Functions for Simulating Liquid Water. *J. Chem. Phys.* **1983**, *79*, 926.

(17) Uberuaga, B. P.; Anghel, M.; Voter, A. F. Synchronization of Trajectories in Canonical Molecular-Dynamics Simulations: Observation, Explanation, and Exploitation. *J. Chem. Phys.* **2004**, *120*, 6363–6374.

(18) Feller, S. E.; Zhang, Y.; Pastor, R. W.; Brooks, B. R. Constant Pressure Molecular Dynamics Simulation: the Langevin Piston Method. *J. Chem. Phys.* **1995**, *103*, 4613–4621.

(19) Vanommeslaeghe, K.; Hatcher, E.; Acharya, C.; Kundu, S.; Zhong, S.; Shim, J.; Darian, E.; Guvench, O.; Lopes, P.; Vorobyov, I.; et al. CHARMM General Force Field: a Force Field for Drug-Like Molecules Compatible with the CHARMM All-Atom Additive Biological Force Fields. *J Comput Chem* **2010**, *31*, 671–690.

(20) Yu, W.; He, X.; Vanommeslaeghe, K.; MacKerell, A. D. Extension of the CHARMM General Force Field to Sulfonyl-Containing Compounds and Its Utility in Biomolecular Simulations. *J Comput Chem* **2012**, *33*, 2451–2468.

REFERENCES

CHAPTER 1

(1) Holland, G. P.; Sharma, R.; Agola, J. O.; Amin, S.; Solomon, V. C.; Singh, P.; Buttry, D. A.; Yarger, J. L. NMR Characterization of Phosphonic Acid Capped SnO_2 Nanoparticles. *Chem. Mater.* **2007**, *19*, 2519–2526.

(2) Kobayashi, T.; Mao, K.; Wang, S.-G.; Lin, V. S.-Y.; Pruski, M. Molecular Ordering of Mixed Surfactants in Mesoporous Silicas: a Solid-State NMR Study. *Solid-State Nucl. Magn. Reson.* **2011**, *39*, 65–71.

(3) Babonneau, F.; Baccile, N.; Laurent, G.; Maquet, J.; Azaïs, T.; Gervais, C.; Bonhomme, C. Solid-State Nuclear Magnetic Resonance: a Valuable Tool to Explore Organic-Inorganic Interfaces in Silica-Based Hybrid Materials. *C. R. Chimie* **2010**, *13*, 58–68.

(4) Wang, W.; Banerjee, S.; Jia, S.; Steigerwald, M. L.; Herman, I. P. Ligand Control of Growth, Morphology, and Capping Structure of Colloidal CdSe Nanorods. *Chem. Mater.* **2007**, *19*, 2573–2580.

(5) Daniel, M.-C.; Astruc, D. Gold Nanoparticles: Assembly, Supramolecular Chemistry, Quantum-Size-Related Properties, and Applications Toward Biology, Catalysis, and Nanotechnology. *Chem. Rev.* **2004**, *104*, 293–346.

(6) Cushing, B. L.; Kolesnichenko, V. L.; O'Connor, C. J. Recent Advances in the Liquid-Phase Syntheses of Inorganic Nanoparticles. *Chem. Rev.* **2004**, *104*, 3893–3946.

(7) Stranick, S. J.; Parikh, A. N.; Tao, Y. T.; Allara, D. L.; Weiss, P. S. Phase Separation of Mixed-Composition Self-Assembled Monolayers Into Nanometer Scale Molecular Domains. *J. Phys. Chem.* **1994**, *98*, 7636–7646.

(8) Smith, R. K.; Reed, S. M.; Lewis, P. A.; Monnell, J. D.; Clegg, R. S.; Kelly, K. F.; Bumm, L. A.; Hutchison, J. E.; Weiss, P. S. Phase Separation Within a Binary Self-Assembled Monolayer on Au{111} Driven by an Amide-Containing Alkanethiol. *J. Phys. Chem. B* **2001**, *105*, 1119–1122.

(9) Lewis, P. A.; Smith, R. K.; Kelly, K. F.; Bumm, L. A.; Reed, S. M.; Clegg, R. S.; Gunderson, J. D.; Hutchison, J. E.; Weiss, P. S. The Role of Buried Hydrogen Bonds in Self-Assembled Mixed Composition Thiols on Au{111}. *J. Phys. Chem. B* **2001**, *105*, 10630–10636.

(10) Jackson, A. M.; Myerson, J. W.; Stellacci, F. Spontaneous Assembly of Subnanometre-Ordered Domains in the Ligand Shell of Monolayer-Protected Nanoparticles. *Nat. Mater.* **2004**, *3*, 330–336.

(11) Jackson, A. M.; Hu, Y.; Silva, P. J.; Stellacci, F. From Homoligand- to Mixed-Ligand- Monolayer-Protected Metal Nanoparticles: a Scanning Tunneling Microscopy Investigation. *J. Am. Chem. Soc.* **2006**, *128*, 11135–11149.

(12) Ong, Q. K.; Zhao, S.; Reguera, J.; Biscarini, F.; Stellacci, F. Comparative STM Studies of Mixed Ligand Monolayers on Gold Nanoparticles in Air and in 1-Phenyloctane. *Chem. Commun.* **2014**, *50*, 10456–10459.

(13) Ong, Q. K.; Reguera, J.; Silva, P. J.; Moglianetti, M.; Harkness, K.; Longobardi, M.; Mali, K. S.; Renner, C.; De Feyter, S.; Stellacci, F. High-Resolution Scanning Tunneling Microscopy Characterization of Mixed Monolayer Protected Gold Nanoparticles. *ACS Nano* **2013**, *7*, 8529–8539.

(14) Vilain, C.; Goettmann, F.; Moores, A.; Le Floch, P.; Sanchez, C. Study of Metal Nanoparticles Stabilised by Mixed Ligand Shell: a Striking Blue Shift of the Surface-Plasmon Band Evidencing the Formation of Janus Nanoparticles. *J. Mater. Chem.* **2007**, *17*, 3509–3514.

(15) Walther, A.; Müller, A. H. E. Janus Particles: Synthesis, Self-Assembly, Physical Properties, and Applications. *Chem. Rev.* **2013**, *113*, 5194–5261.

(16) Singh, C.; Ghorai, P. K.; Horsch, M. A.; Jackson, A. M.; Larson, R. G.; Stellacci, F.; Glotzer, S. C. Entropy-Mediated Patterning of Surfactant-Coated Nanoparticles and Surfaces. *Phys. Rev. Lett.* **2007**, *99*, 226106.

(17) Singh, C.; Jackson, A. M.; Stellacci, F.; Glotzer, S. C. Exploiting Substrate Stress to Modify Nanoscale SAM Patterns. *J. Am. Chem. Soc.* **2009**, *131*, 16377–16379.

(18) Pons-Siepermann, I. C.; Glotzer, S. C. Design of Patchy Particles Using Quaternary Self-Assembled Monolayers. *ACS Nano* **2012**, *6*, 3919–3924.

(19) Shafi, K. V. P. M.; Ulman, A.; Yan, X.; Yang, N.-L.; Estournès, C.; White, H.; Rafailovich, M. Sonochemical Synthesis of Functionalized Amorphous Iron Oxide Nanoparticles. *Langmuir* **2001**, *17*, 5093–5097.

(20) McElwee, J.; Helmy, R.; Fadeev, A. Y. Thermal Stability of Organic Monolayers Chemically Grafted to Minerals. *J. Colloid Interf. Sci.* **2005**, *285*, 551–556.

(21) Marcinko, S.; Fadeev, A. Y. Hydrolytic Stability of Organic Monolayers Supported on TiO 2and ZrO 2. *Langmuir* **2004**, *20*, 2270–2273.

(22) Silverman, B. M.; Wieghaus, K. A.; Schwartz, J. Comparative Properties of Siloxane vs Phosphonate Monolayers on a Key Titanium Alloy. *Langmuir* **2005**, *21*, 225–228.

(23) Hotchkiss, P. J.; Jones, S. C.; Paniagua, S. A.; Sharma, A.; Kippelen, B.; Armstrong, N. R.; Marder, S. R. The Modification of Indium Tin Oxide with Phosphonic Acids: Mechanism of Binding, Tuning of Surface Properties, and Potential for Use in Organic Electronic Applications. *Acc. Chem. Res.* **2012**, *45*, 337–346.

(24) Paniagua, S. A.; Hotchkiss, P. J.; Jones, S. C.; Marder, S. R.; Mudalige, A.; Marrikar, F. S.; Pemberton, J. E.; Armstrong, N. R. Phosphonic Acid Modification of Indium−Tin Oxide Electrodes: Combined XPS/UPS/Contact Angle Studies. *J. Phys. Chem. C* **2008**, *112*, 7809–7817.

(25) Gawalt, E. S.; Avaltroni, M. J.; Koch, N.; Schwartz, J. Self-Assembly and Bonding of Alkanephosphonic Acids on the Native Oxide Surface of Titanium. *Langmuir* **2001**, *17*, 5736–5738.

(26) Guerrero, G.; Mutin, P. H.; Vioux, A. Anchoring of Phosphonate and Phosphinate Coupling Molecules on Titania Particles. *Chem. Mater.* **2001**, *13*, 4367–4373.

(27) Sahoo, Y.; Pizem, H.; Fried, T.; Golodnitsky, D.; Burstein, L.; Sukenik, C. N.; Markovich, G. Alkyl Phosphonate/Phosphate Coating on Magnetite Nanoparticles: a Comparison with Fatty Acids. *Langmuir* **2001**, *17*, 7907–7911.

(28) Pawsey, S.; McCormick, M.; De Paul, S.; Graf, R.; Lee, Y. S.; Reven, L.; Spiess, H. W. 1H Fast MAS NMR Studies of Hydrogen-Bonding Interactions in Self-Assembled Monolayers. *J. Am. Chem. Soc.* **2003**, *125*, 4174–4184.

(29) Hotchkiss, P. J.; Malicki, M.; Giordano, A. J.; Armstrong, N. R.; Marder, S. R. Characterization of Phosphonic Acid Binding to Zinc Oxide. *J. Mater. Chem.* **2011**, *21*, 3107–3112.

(30) Lukes, I.; Borbaruah, M.; Quin, L. D. Direct Reaction of Phosphorus Acids with Hydroxy of a Silanol and on the Silica Gel Surface. *J. Am. Chem. Soc.* **1994**, *116*, 1737–1741.

(31) Hanson, E. L.; Schwartz, J.; Nickel, B.; Koch, N.; Danisman, M. F. Bonding Self-Assembled, Compact Organophosphonate Monolayers to the Native Oxide Surface of Silicon. *J. Am. Chem. Soc.* **2003**, *125*, 16074–16080.

(32) Gouzman, I.; Dubey, M.; Carolus, M. D.; Schwartz, J.; Bernasek, S. L. Monolayer vs. Multilayer Self-Assembled Alkylphosphonate Films: X-Ray Photoelectron Spectroscopy Studies. *Surf. Sci.* **2006**, *600*, 773–781.

(33) Egger, N.; Schmidt-Rohr, K.; Blümich, B.; Domke, W. D.; Stapp, B. Solid State NMR Investigation of Cationic Polymerized Epoxy Resins. *J. Appl. Polym. Sci.* **1992**, *44*, 289–295.

(34) Aliev, A.; Li Ou, D.; Ormsby, B.; Sullivan, A. C. Porous Silica and Polysilsesquioxane with Covalently Linked Phosphonates and Phosphonic Acids. *J. Mater. Chem.* **2000**, *10*, 2758–2764.

(35) Mutin, P. H.; Lafond, V.; Popa, A. F.; Granier, M.; Markey, L.; Dereux, A. Selective Surface Modification of SiO 2−TiO 2Supports with Phosphonic Acids. *Chem. Mater.* **2004**, *16*, 5670–5675.

(36) Gomes, R.; Hassinen, A.; Szczygiel, A.; Zhao, Q.; Vantomme, A.; Martins, J. C.; Hens, Z. Binding of Phosphonic Acids to CdSe Quantum Dots: a Solution NMR Study. *J. Phys. Chem. Lett.* **2011**, *2*, 145–152.

(37) Hassinen, A.; Gomes, R.; De Nolf, K.; Zhao, Q.; Vantomme, A.; Martins, J. C.; Hens, Z. Surface Chemistry of CdTe Quantum Dots Synthesized in Mixtures of Phosphonic Acids and Amines: Formation of a Mixed Ligand Shell. *J. Phys. Chem. C* **2013**, *117*, 13936–13943.

(38) Carbone, L.; Kudera, S.; Carlino, E.; Parak, W. J.; Giannini, C.; Cingolani, R.; Manna, L. Multiple Wurtzite Twinning in CdTe Nanocrystals Induced by Methylphosphonic Acid. *J. Am. Chem. Soc.* **2006**, *128*, 748–755.

(39) Wang, F.; Tang, R.; Kao, J. L.-F.; Dingman, S. D.; Buhro, W. E. Spectroscopic Identification of Tri-N-Octylphosphine Oxide (TOPO) Impurities and Elucidation of Their Roles in Cadmium Selenide Quantum-Wire Growth. *J. Am. Chem. Soc.* **2009**, *131*, 4983–4994.

(40) Dubey, M.; Weidner, T.; Gamble, L. J.; Castner, D. G. Structure and Order of Phosphonic Acid-Based Self-Assembled Monolayers on Si(100). *Langmuir* **2010**, *26*, 14747–14754.

(41) P chy, P. T.; Rotzinger, F. O. P.; Nazeeruddin, M. K.; Kohle, O.; Zakeeruddin, S. M.; Humphry-Baker, R.; Gr tzel, M. Preparation of Phosphonated Polypyridyl Ligands to Anchor Transition-Metal Complexes on Oxide Surfaces: Application for the Conversion of Light to Electricity with Nanocrystalline TiO2 Films. *J. Chem. Soc., Chem. Commun.* **1995**, *0*, 65–66.

(42) Ruile, S.; Kohle, O.; Péchy, P.; Grätzel, M. Novel Sensitisers for Photovoltaic Cells. Structural Variations of Ru(II) Complexes Containing 2,6-Bis(1-Methylbenzimidazol-2-Yl)Pyridine. *Inorganica Chimica Acta* **1997**, *261*, 129–140.

(43) Zakeeruddin, S. M.; Nazeeruddin, M. K.; Pechy, P.; Rotzinger, F. P.; Humphry-Baker, R.; Kalyanasundaram, K.; Grätzel, M.; Shklover, V.; Haibach, T. Molecular Engineering of Photosensitizers for Nanocrystalline Solar Cells: Synthesis and Characterization of Ru Dyes Based on Phosphonated Terpyridines. *Inorg. Chem.* **1997**, *36*, 5937–5946.

(44) Wang, P.; Klein, C.; Moser, J.-E.; Humphry-Baker, R.; Cevey-Ha, N.-L.; Charvet, R.; Comte, P.; Zakeeruddin, S. M.; Grätzel, M. Amphiphilic Ruthenium Sensitizer with 4,4‘-Diphosphonic Acid-2,2‘-Bipyridine as Anchoring Ligand for Nanocrystalline Dye Sensitized Solar Cells. *J. Phys. Chem. B* **2004**, *108*, 17553–17559.

(45) Foster, E. W.; Kearns, G. J.; Goto, S.; Hutchison, J. E. Patterned Gold-Nanoparticle Monolayers Assembled on the Oxide of Silicon. *Adv. Mater.* **2005**, *17*, 1542–1545.

(46) Ito, D.; Jespersen, M. L.; Hutchison, J. E. Selective Growth of Vertical ZnO Nanowire Arrays Using Chemically Anchored Gold Nanoparticles. *ACS Nano* **2008**, *2*, 2001–2006.

(47) Bluemel, J. Reactions of Phosphines with Silicas: a Solid-State NMR Study. *Inorg. Chem.* **1994**, *33*, 5050–5056.

(48) Gao, W.; Dickinson, L.; Grozinger, C.; Morin, F. G.; Reven, L. Self-Assembled Monolayers of Alkylphosphonic Acids on Metal Oxides. *Langmuir* **1996**, *12*, 6429–6435.

(49) Pawsey, S.; Yach, K.; Reven, L. Self-Assembly of Carboxyalkylphosphonic Acids on Metal Oxide Powders. *Langmuir* **2002**, *18*, 5205–5212.

(50) Lafond, V.; Gervais, C.; Maquet, J.; Prochnow, D.; Babonneau, F.; Mutin, P. H. 17O MAS NMR Study of the Bonding Mode of Phosphonate Coupling Molecules in a Titanium Oxo-Alkoxo-Phosphonate and in Titania-Based Hybrid Materials. *Chem. Mater.* **2003**, *15*, 4098–4103.

(51) Brodard-Severac, F.; Guerrero, G.; Maquet, J.; Florian, P.; Gervais, C.; Mutin, P. H. High-Field 17O MAS NMR Investigation of Phosphonic Acid Monolayers on Titania. *Chem. Mater.* **2008**, *20*, 5191–5196.

(52) Neff, G. A.; Page, C. J.; Meintjes, E.; Tsuda, T.; Pilgrim, W. C.; Roberts, N.; Warren, W. W. Hydrolysis of Surface-Bound Phosphonate Esters for the Self-Assembly of Multilayer Films: Use of Solid State Magic Angle Spinning 31P NMR as a Probe of Reactions on Surfaces. *Langmuir* **1996**, *12*, 238–242.

(53) Kosmulski, M. Compilation of PZC and IEP of Sparingly Soluble Metal Oxides and Hydroxides From Literature. *Adv Colloid Interface Sci* **2009**, *152*, 14–25.

(54) Liu, C. C.; Maciel, G. E. The Fumed Silica Surface: a Study by NMR. *J. Am. Chem. Soc.* **1996**, *118*, 5103–5119.

(55) Brei, V. V. 29Si Solid-State NMR Study of the Surface Structure of Aerosil Silica. *J. Chem. Soc., Faraday Trans.* **1994**, *90*, 2961.

(56) Gun'ko, V. M.; Voronin, E. F.; Pakhlov, E. M.; Zarko, V. I.; Turov, V. V.; Guzenko, N. V.; Leboda, R.; Chibowski, E. Features of Fumed Silica Coverage with Silanes Having Three or Two Groups Reacting with the Surface. *Colloids Surf., A* **2000**, *166*, 187–201.

(57) Bennett, A. E.; Rienstra, C. M.; Auger, M.; Lakshmi, K. V.; Griffin, R. G. Heteronuclear Decoupling in Rotating Solids. *J. Chem. Phys.* **1995**, *103*, 6951–6957.

(58) Cory, D. G.; Ritchey, W. M. Suppression of Signals From the Probe in Block Decay Spectra. *J. Magn. Reson.* **1988**, *80*, 128–132.

(59) Feike, M.; Demco, D. E.; Graf, R.; Gottwald, J.; Hafner, S.; Spiess, H. W. Broadband Multiple-Quantum NMR Spectroscopy. *J. Magn. Reson., Ser A* **1996**, *122*, 214–221.

(60) Schnell, I.; Spiess, H. W. High-Resolution 1H NMR Spectroscopy in the Solid State: Very Fast Sample Rotation and Multiple-Quantum Coherences. *J. Magn. Reson.* **2001**, *151*, 153–227.

(61) Hayashi, S.; Hayamizu, K. High-Resolution Solid-State 31P NMR of Alkali Phosphates. *Bull. Chem. Soc. Jpn.* **1989**.

(62) Massiot, D.; Fayon, F.; Capron, M.; King, I.; Calve, S. L.; Alonso, B.; Durand, J. O.; Bujoli, B.; Gan, Z.; Hoatson, G. Modelling One- and Two-Dimensional Solid-State NMR Spectra. *Magn. Reson. Chem.* **2002**, *40*, 70–76.

(63) Bak, M.; Rasmussen, J. T.; Nielsen, N. C. SIMPSON: a General Simulation Program for Solid-State NMR Spectroscopy. *J. Magn. Reson.* **2000**, *147*, 296–330.

(64) Crofts, P. C.; Kosolapoff, G. M. Preparation and Determination of Apparent Dissociation Constants of Some Alkylphosphonic and Dialkylphosphinic Acids 1. *J. Am. Chem. Soc.* **1953**, *75*, 3379–3383.

(65) Jaffé, H. H.; Freedman, L. D.; Doak, G. O. The Acid Dissociation Constants of Aromatic Phosphonic Acids. I. Meta and Para Substituted Compounds 1. *J. Am. Chem. Soc.* **1953**, *75*, 2209–2211.

(66) Trébosc, J.; Wiench, J. W.; Huh, S.; Lin, V. S.-Y.; Pruski, M. Solid-State NMR Study of MCM-41-Type Mesoporous Silica Nanoparticles. *J. Am. Chem. Soc.* **2005**, *127*, 3057–3068.

(67) Trébosc, J.; Wiench, J. W.; Huh, S.; Lin, V. S.-Y.; Pruski, M. Studies of Organically Functionalized Mesoporous Silicas Using Heteronuclear Solid-State Correlation NMR Spectroscopy Under Fast Magic Angle Spinning. *J. Am. Chem. Soc.* **2005**, *127*, 7587–7593.

(68) Maciel, G. E.; Sindorf, D. W. Silicon-29 NMR Study of the Surface of Silica Gel by Cross Polarization and Magic-Angle Spinning. *J. Am. Chem. Soc.* **1980**, *102*, 7606–7607.

(69) Tielens, F.; Gervais, C.; Lambert, J.-F.; Mauri, F.; Costa, D. Ab Initio Study of the Hydroxylated Surface of Amorphous Silica: a Representative Model. *Chem. Mater.* **2008**, *20*, 3336–3344.

(70) Chuang, I. S.; Kinney, D. R.; Maciel, G. E. Interior Hydroxyls of the Silica Gel System as Studied by Silicon-29 CP-MAS NMR Spectroscopy. *J. Am. Chem. Soc.* **1993**, *115*, 8695–8705.

(71) d'espinose de la Caillerie, J.-B.; Aimeur, M. R.; Kortobi, Y. E.; Legrand, A. P. Water Adsorption on Pyrogenic Silica Followed by1H MAS NMR. *J. Colloid Interf. Sci.* **1997**, *194*, 434–439.

(72) Perrin, C. L.; Dwyer, T. J. Application of Two-Dimensional NMR to Kinetics of Chemical Exchange. *Chem. Rev.* **1990**, *90*, 935–967.

(73) Brown, S. P. Probing Proton–Proton Proximities in the Solid State. *Prog. Nucl. Magn. Reson. Spectrosc.* **2007**, *50*, 199–251.

(74) Brown, S. P. Applications of High-Resolution 1H Solid-State NMR. *Solid-State Nucl. Magn. Reson.* **2012**, *41*, 1–27.

(75) Schmidt-Rohr, K.; Spiess, H. W. Multidimensional Solid-State NMR and Polymers - Klaus Schmidt-Rohr, Hans Wolfgang Spiess - Google Books. **1994**.

CHAPTER 2

(1) Chaudhuri, R. G.; Paria, S. Core/Shell Nanoparticles: Classes, Properties, Synthesis Mechanisms, Characterization, and Applications. *Chem. Rev.* **2012**, *112*, 2373–2433.

(2) Hines, M. A.; Guyot-Sionnest, P. Synthesis and Characterization of Strongly Luminescing ZnS-Capped CdSe Nanocrystals. *J. Phys. Chem.* **1996**, *100*, 468–471.

(3) Dabbousi, B. O.; Rodriguez-Viejo, J.; Mikulec, F. V.; Heine, J. R.; Mattoussi, H.; Ober, R.; Jensen, K. F.; Bawendi, M. G. (CdSe)ZnS Core−Shell Quantum Dots: Synthesis and Characterization of a Size Series of Highly Luminescent Nanocrystallites. *J. Phys. Chem. B* **1997**, *101*, 9463–9475.

(4) Peng, X.; Schlamp, M. C.; Kadavanich, A. V.; Alivisatos, A. P. Epitaxial Growth of Highly Luminescent CdSe/CdS Core/Shell Nanocrystals with Photostability and Electronic Accessibility. *J. Am. Chem. Soc.* **1997**, *119*, 7019–7029.

(5) Reiss, P.; Protière, M.; Li, L. Core/Shell Semiconductor Nanocrystals. *Small* **2009**, *5*, 154–168.

(6) Chon, B.; Lim, S. J.; Kim, W.; Seo, J.; Kang, H.; Joo, T.; Hwang, J.; Shin, S. K. Shell and Ligand-Dependent Blinking of CdSe -Based Core/Shell Nanocrystals. *Phys. Chem. Chem. Phys.* **2010**, *12*, 9312–9319.

(7) Liu, H.; Owen, J. S.; Alivisatos, A. P. Mechanistic Study of Precursor Evolution in Colloidal Group II−VI Semiconductor Nanocrystal Synthesis. *J. Am. Chem. Soc.* **2007**, *129*, 305–312.

(8) García-Rodríguez, R.; Hendricks, M. P.; Cossairt, B. M.; Liu, H.; Owen, J. S. Conversion Reactions of Cadmium Chalcogenide Nanocrystal Precursors. *Chem. Mater.* **2013**, *25*, 1233–1249.

(9) Abe, S.; Capek, R. K.; De Geyter, B.; Hens, Z. Reaction Chemistry/Nanocrystal Property Relations in the Hot Injection Synthesis, the Role of the Solute Solubility. *ACS Nano* **2013**, *7*, 943–949.

(10) Yu, K.; Liu, X.; Zeng, Q.; Yang, M.; Ouyang, J.; Wang, X.; Tao, Y. The Formation Mechanism of Binary Semiconductor Nanomaterials: Shared by Single-Source and Dual-Source Precursor Approaches. *Angew Chem Int Ed* **2013**, *52*, 11034–11039.

(11) Wang, W.; Banerjee, S.; Jia, S.; Steigerwald, M. L.; Herman, I. P. Ligand Control of Growth, Morphology, and Capping Structure of Colloidal CdSe Nanorods. *Chem. Mater.* **2007**, *19*, 2573–2580.

(12) Wang, F.; Tang, R.; Buhro, W. E. The Trouble with TOPO; Identification of Adventitious Impurities Beneficial to the Growth of Cadmium Selenide Quantum Dots, Rods, and Wires. *Nano Lett.* **2008**, *8*, 3521–3524.

(13) Wang, F.; Tang, R.; Kao, J. L.-F.; Dingman, S. D.; Buhro, W. E. Spectroscopic Identification of Tri-N-Octylphosphine Oxide (TOPO) Impurities and Elucidation of Their Roles in Cadmium Selenide Quantum-Wire Growth. *J. Am. Chem. Soc.* **2009**, *131*, 4983–4994.

(14) Huang, J.; Kovalenko, M. V.; Talapin, D. V. Alkyl Chains of Surface Ligands Affect Polytypism of CdSe Nanocrystals and Play an Important Role in the Synthesis of Anisotropic Nanoheterostructures. *J. Am. Chem. Soc.* **2010**, *132*, 15866–15868.

(15) Frederick, M. T.; Achtyl, J. L.; Knowles, K. E.; Weiss, E. A.; Geiger, F. M. Surface-Amplified Ligand Disorder in CdSe Quantum Dots Determined by Electron and Coherent Vibrational Spectroscopies. *J. Am. Chem. Soc.* **2011**, *133*, 7476–7481.

(16) Morris-Cohen, A. J.; Frederick, M. T.; Lilly, G. D.; McArthur, E. A.; Weiss, E. A. Organic Surfactant-Controlled Composition of the Surfaces of CdSe Quantum Dots. *J. Phys. Chem. Lett.* **2010**, *1*, 1078–1081.

(17) Hassinen, A.; Moreels, I.; De Nolf, K.; Smet, P. F.; Martins, J. C.; Hens, Z. Short-Chain Alcohols Strip X-Type Ligands and Quench the Luminescence of PbSe and CdSe Quantum Dots, Acetonitrile Does Not. *J. Am. Chem. Soc.* **2012**, *134*, 20705–20712.

(18) Coto-García, A. M.; Fernández-Argüelles, M. T. The Influence of Surface Coating on the Properties of Water-Soluble CdSe and CdSe/ZnS Quantum Dots. *J. Nanopart. Res.* **2013**, *15*, 1330–1341.

(19) Pawsey, S.; Yach, K.; Reven, L. Self-Assembly of Carboxyalkylphosphonic Acids on Metal Oxide Powders. *Langmuir* **2002**, *18*, 5205–5212.

(20) Morris-Cohen, A. J.; Donakowski, M. D.; Knowles, K. E.; Weiss, E. A. The Effect of a Common Purification Procedure on the Chemical Composition of the Surfaces of CdSe Quantum Dots Synthesized with Trioctylphosphine Oxide. *J. Phys. Chem. C* **2010**, *114*, 897–906.

(21) Holland, G. P.; Sharma, R.; Agola, J. O.; Amin, S.; Solomon, V. C.; Singh, P.; Buttry, D. A.; Yarger, J. L. NMR Characterization of Phosphonic Acid Capped SnO 2Nanoparticles. *Chem. Mater.* **2007**, *19*, 2519–2526.

(22) Brodard-Severac, F.; Guerrero, G.; Maquet, J.; Florian, P.; Gervais, C.; Mutin, P. H. High-Field 17O MAS NMR Investigation of Phosphonic Acid Monolayers on Titania. *Chem. Mater.* **2008**, *20*, 5191–5196.

(23) Marcinko, S.; Fadeev, A. Y. Hydrolytic Stability of Organic Monolayers Supported on TiO 2and ZrO 2. *Langmuir* **2004**, *20*, 2270–2273.

(24) McElwee, J.; Helmy, R.; Fadeev, A. Y. Thermal Stability of Organic Monolayers Chemically Grafted to Minerals. *J. Colloid Interf. Sci.* **2005**, *285*, 551–556.

(25) Kopping, J. T.; Patten, T. E. Identification of Acidic Phosphorus-Containing Ligands Involved in the Surface Chemistry of CdSe Nanoparticles Prepared in Tri-N-Octylphosphine Oxide Solvents. *J. Am. Chem. Soc.* **2008**, *130*, 5689–5698.

(26) Peng, X.; Manna, L.; Yang, W.; Wickham, J.; Scher, E.; Kadavanich, A.; Alivisatos, A. P. Shape Control of CdSe Nanocrystals. *Nature* **2000**, *404*, 59–61.

(27) Hens, Z.; Martins, J. C. A Solution NMR Toolbox for Characterizing the Surface Chemistry of Colloidal Nanocrystals. *Chem. Mater.* **2013**, *25*, 1211–1221.

(28) Ratcliffe, C. I.; Yu, K.; Ripmeester, J. A.; Badruz Zaman, M.; Badarau, C.; Singh, S. Solid State NMR Studies of Photoluminescent Cadmium Chalcogenide Nanoparticles. *Phys. Chem. Chem. Phys.* **2006**, *8*, 3510–3519.

(29) Gomes, R.; Hassinen, A.; Szczygiel, A.; Zhao, Q.; Vantomme, A.; Martins, J. C.; Hens, Z. Binding of Phosphonic Acids to CdSe Quantum Dots: a Solution NMR Study. *J. Phys. Chem. Lett.* **2011**, *2*, 145–152.

(30) Moreels, I.; Martins, J. C.; Hens, Z. Ligand Adsorption/Desorption on Sterically Stabilized InP Colloidal Nanocrystals: Observation and Thermodynamic Analysis. *ChemPhysChem* **2006**, *7*, 1028–1031.

(31) Iacono, F.; Palencia, C.; la Cueva, de, L.; Meyns, M.; Terracciano, L.; Vollmer, A.; la Mata, de, M. J.; Klinke, C.; Gallego, J. M.; Juarez, B. H.; et al. Interfacing Quantum Dots and Graphitic Surfaces with Chlorine Atomic Ligands. *ACS Nano* **2013**, *7*, 2559–2565.

(32) Steigerwald, M. L.; Alivisatos, A. P.; Gibson, J. M.; Harris, T. D.; Kortan, R.; Muller, A. J.; Thayer, A. M.; Duncan, T. M.; Douglass, D. C.; Brus, L. E. Surface Derivatization and Isolation of Semiconductor Cluster Molecules. *J. Am. Chem. Soc.* **1988**, *110*, 3046–3050.

(33) Tomaselli, M.; Yarger, J. L.; Bruchez, M.; Havlin, R. H.; deGraw, D.; Pines, A.; Alivisatos, A. P. NMR Study of InP Quantum Dots: Surface Structure and Size Effects. *J. Chem. Phys.* **1999**, *110*, 8861.

(34) Jeong, S.; Achermann, M.; Nanda, J.; Ivanov, S.; Klimov, V. I.; Hollingsworth, J. A. Effect of the Thiol-Thiolate Equilibrium on the Photophysical Properties of Aqueous CdSe/ZnS Nanocrystal Quantum Dots. *J. Am. Chem. Soc.* **2005**, *127*, 10126–10127.

(35) Dubois, F.; Mahler, B.; Dubertret, B.; Doris, E.; Mioskowski, C. A Versatile Strategy for Quantum Dot Ligand Exchange. *J. Am. Chem. Soc.* **2007**, *129*, 482–483.

(36) Zylstra, J.; Amey, J.; Miska, N. J.; Pang, L.; Hine, C. R.; Langer, J.; Doyle, R. P.; Maye, M. M. A Modular Phase Transfer and Ligand Exchange Protocol for Quantum Dots. *Langmuir* **2011**, *27*, 4371–4379.

(37) Owen, J. S.; Park, J.; Trudeau, P.-E.; Alivisatos, A. P. Reaction Chemistry and Ligand Exchange at Cadmium−Selenide Nanocrystal Surfaces. *J. Am. Chem. Soc.* **2008**, *130*, 12279–12281.

(38) Hassinen, A.; Gomes, R.; De Nolf, K.; Zhao, Q.; Vantomme, A.; Martins, J. C.; Hens, Z. Surface Chemistry of CdTe Quantum Dots Synthesized in Mixtures of Phosphonic Acids and Amines: Formation of a Mixed Ligand Shell. *J. Phys. Chem. C* **2013**, *117*, 13936–13943.

(39) Caldwell, M. A.; Albers, A. E.; Levy, S. C.; Pick, T. E.; Cohen, B. E.; Helms, B. A.; Milliron, D. J. Driving Oxygen Coordinated Ligand Exchange at Nanocrystal Surfaces Using Trialkylsilylated Chalcogenides. *Chem. Commun.* **2011**, *47*, 556–558.

(40) Murray, C. B.; Norris, D. J.; Bawendi, M. G. Synthesis and Characterization of Nearly Monodisperse CdE (E = Sulfur, Selenium, Tellurium) Semiconductor Nanocrystallites. *J. Am. Chem. Soc.* **1993**, *115*, 8706–8715.

(41) Shaka, A. J.; Keeler, J.; Frenkiel, T.; Freeman, R. An Improved Sequence for Broadband Decoupling: WALTZ-16. *J. Magn. Reson.* **1983**, *52*, 335–338.

(42) Bennett, A. E.; Rienstra, C. M.; Auger, M.; Lakshmi, K. V.; Griffin, R. G. Heteronuclear Decoupling in Rotating Solids. *J. Chem. Phys.* **1995**, *103*, 6951–6957.

(43) Gutmann, T.; Bonnefille, E.; Breitzke, H.; Debouttière, P.-J.; Philippot, K.; Poteau, R.; Buntkowsky, G.; Chaudret, B. Investigation of the Surface Chemistry of Phosphine-Stabilized Ruthenium Nanoparticles--an Advanced Solid-State NMR Study. *Phys. Chem. Chem. Phys.* **2013**, *15*, 17383–17394.

(44) Lafond, V.; Gervais, C.; Maquet, J.; Prochnow, D.; Babonneau, F.; Mutin, P. H. 17O MAS NMR Study of the Bonding Mode of Phosphonate Coupling Molecules in a Titanium Oxo-Alkoxo-Phosphonate and in Titania-Based Hybrid Materials. *Chem. Mater.* **2003**, *15*, 4098–4103.

(45) Crofts, P. C.; Kosolapoff, G. M. Preparation and Determination of Apparent Dissociation Constants of Some Alkylphosphonic and Dialkylphosphinic Acids 1. *J. Am. Chem. Soc.* **1953**, *75*, 3379–3383.

(46) Jaffé, H. H.; Freedman, L. D.; Doak, G. O. The Acid Dissociation Constants of Aromatic Phosphonic Acids. I. Meta and Para Substituted Compounds 1. *J. Am. Chem. Soc.* **1953**, *75*, 2209–2211.

CHAPTER 3

(1) Inoue, D.; Mitsushima, S.; Matsuzawa, K.; Lee, S.-Y.; Yasuda, T.; Watanabe, M.; OTA, K.-I. A Mesothermal Fuel Cell Using Diethylmethylammonium Trifluoromethanesulfonate Absorbed Membrane with H3PO4 Addition and Various Amount of Electrolyte Loading in Catalyst Layer. *Electrochemistry* **2011**, *79*, 377–380.

(2) Lee, S. Y.; Yasuda, T.; Watanabe, M. Fabrication of Protic Ionic Liquid/Sulfonated Polyimide Composite Membranes for Non-Humidified Fuel Cells. *J. Power Sources* **2010,** *195,* 5909-5914.

(3) Mitsushima, S.; Shinohara, Y.; Matsuzawa, K.; Ota, K. Mass Transportation in Diethylmethylammonium Trifluoromethanesulfonate for Fuel Cell Applications. *Electrochimica Acta* **2010,** *55,* 6639-6644.

(4) Li, H.; Jiang, F.; Di, Z.; Gu, J. Anhydrous Proton-Conducting Glass Membranes Doped with Ionic Liquid for Intermediate-Temperature Fuel Cells. *Electrochimica Acta* **2012**, *59*, 86–90.

(5) Li, Q.; He, R.; Ronghuan He; Jens Oluf Jensen, A.; Bjerrum, N. J. Approaches and Recent Development of Polymer Electrolyte Membranes for Fuel Cells Operating Above 100 °C. *Chem. Mater.* **2003**, *15*, 4896–4915.

(6) Binary Inorganic Salt Mixtures as High Conductivity Liquid Electrolytes for >100 ºC Fuel Cells. **2006**, 4799–3.

(7) Miran, M. S.; Yasuda, T.; Susan, M. A. B. H.; Dokko, K.; Watanabe, M. Binary Protic Ionic Liquid Mixtures as a Proton Conductor: High Fuel Cell Reaction Activity and Facile Proton Transport. **2014**, *118*, 27631–27639.

(8) Xu, W.; Angell, C. A. Solvent-Free Electrolytes with Aqueous Solution-Like Conductivities. *Science* **2003**, *302*, 422–425.

(9) Menne, S.; Pires, J.; Anouti, M.; Balducci, A. Protic Ionic Liquids as Electrolytes for Lithium-Ion Batteries. *Electrochemistry Communications* **2013,** *31,* 39-41.

(10) Greaves, T. L.; Drummond, C. J. Protic Ionic Liquids: Properties and Applications. *Chem. Rev.* **2008**, *108*, 206–237.

(11) Yoshizawa, M.; Xu, W.; Angell, C. A. Ionic Liquids by Proton Transfer: Vapor Pressure, Conductivity, and the Relevance of Δp Kafrom Aqueous Solutions. *J. Am. Chem. Soc.* **2003**, *125*, 15411–15419.

(12) Macfarlane, D. R.; Forsyth, M.; Izgorodina, E. I.; Abbott, A. P.; Annat, G.; Fraser, K. On the Concept of Ionicity in Ionic Liquids. *Phys. Chem. Chem. Phys.* **2009**, *11*, 4962–4967.

(13) Burrell, G. L.; Burgar, I. M.; Separovic, F.; Dunlop, N. F. Preparation of Protic Ionic Liquids with Minimal Water Content and (15)N NMR Study of Proton Transfer. *Phys. Chem. Chem. Phys.* **2010**, *12*, 1571–1577.

(14) Sarmini, K.; Kenndler, E. Ionization Constants of Weak Acids and Bases in Organic Solvents. *Journal of Biochemical and Biophysical Methods* **1999**, *38*, 123–137.

(15) Bordwell, F. G. Equilibrium Acidities in Dimethyl Sulfoxide Solution. *Acc. Chem. Res.* **1988**, *21*, 456–463.

(16) Belieres, J.-P.; Angell, C. A. Protic Ionic Liquids: Preparation, Characterization, and Proton Free Energy Level Representation. *J. Phys. Chem. B* **2007**, *111*, 4926–4937.

(17) Noda, A.; Susan, M. A. B. H.; Kudo, K.; Mitsushima, S.; Hayamizu, K.; Watanabe, M. Brønsted Acid−Base Ionic Liquids as Proton-Conducting Nonaqueous Electrolytes. *J. Phys. Chem. B* **2003**, *107*, 4024–4033.

(18) Nuthakki, B.; Greaves, T. L.; Krodkiewska, I.; Weerawardena, A.; Burgar, M. I.; Mulder, R. J.; Drummond, C. J. Protic Ionic Liquids and Ionicity. *Australian Journal of Chemistry* **2007**, *60*, 21–28.

(19) Blanchard, J. W.; Belieres, J.-P.; Alam, T. M.; Yarger, J. L.; Holland, G. P. NMR Determination of the Diffusion Mechanisms in Triethylamine-Based Protic Ionic Liquids. *J. Phys. Chem. Lett.* **2011**, *2*, 1077–1081.

(20) Judeinstein, P.; Iojoiu, C.; Sanchez, J.-Y.; Ancian, B. Proton Conducting Ionic Liquid Organization as Probed by NMR: Self-Diffusion Coefficients and Heteronuclear Correlations. *J. Phys. Chem. B* **2008**, *112*, 3680–3683.

(21) Iojoiu, C.; Judeinstein, P.; Sanchez, J. Y. Ion Transport in CLIP: Investigation Through Conductivity and NMR Measurements. *Electrochimica Acta* **2007** *53*, 1395-1403.

(22) Iojoiu, C.; Martinez, M.; Hanna, M.; Molmeret, Y.; Cointeaux, L.; Leprêtre, J.-C.; Kissi, N. E.; Guindet, J.; Judeinstein, P.; Sanchez, J.-Y. PILs-Based Nafion Membranes: a Route to High-Temperature PEFMCs Dedicated to Electric and Hybrid Vehicles. **2008**, *19*, 1406–1414.

(23) Mori, K.; Hashimoto, S.; Yuzuri, T.; Sakakibara, K. Structural and Spectroscopic Characteristics of a Proton-Conductive Ionic Liquid Diethylmethylammonium Trifluoromethanesulfonate [Dema][TfOH]. **2010**, *83*, 328–334.

(24) Mori, K.; Kobayashi, T.; Sakakibara, K.; Ueda, K. Experimental and Theoretical Investigation of Proton Exchange Reaction Between Protic Ionic Liquid Diethylmethylammonium Trifluoromethanesulfonate and H_2O. *Chem. Phys. Lett.* **2012,** *552,* 58-63.

(25) Römich, C.; Merkel, N. C.; Valbonesi, A.; Schaber, K.; Sauer, S.; Schubert, T. J. S. Thermodynamic Properties of Binary Mixtures of Water and Room-Temperature Ionic Liquids: Vapor Pressures, Heat Capacities, Densities, and Viscosities of Water + 1-Ethyl-3-Methylimidazolium Acetate and Water + Diethylmethylammonium Methane Sulfonate. **2012**, *57*, 2258–2264.

(26) Wu, D. H.; Chen, A. D.; Johnson, C. S. An Improved Diffusion-Ordered Spectroscopy Experiment Incorporating Bipolar-Gradient Pulses. *J. Magn. Reson., Ser A* **1995**, *115*, 260–264.

(27) Frisch, M. J.; Trucks, G. W.; Schlegel, H. B.; Scuseria, G. E.; Robb, M. A.; Cheeseman, J. R.; Scalmani, G.; Barone, V.; Mennucci, B.; Petersson, G. A.; et al. Guassian 09.

(28) Miran, M. S.; Kinoshita, H.; Yasuda, T.; Susan, M. A. B. H.; Watanabe, M. Hydrogen Bonds in Protic Ionic Liquids and Their Correlation with Physicochemical Properties. *Chem. Commun.* **2011**, *47*, 12676–12678.

(29) Denisov, G. S.; Gindin, V. A.; Golubev, N. S.; Ligay, S. S.; Shchepkin, D. N.; Smimov, S. N. NMR Study of Proton Location in Strongly Hydrogen Bonded Complexes of Pyridine as Influenced by Solvent Polarity. *J. Mol. Liq.* **1995**, *67*, 217–234.

(30) Kütt, A.; Rodima, T.; Saame, J.; Raamat, E.; Mäemets, V.; Kaljurand, I.; Koppel, I. A.; Garlyauskayte, R. Y.; Yagupolskii, Y. L.; Yagupolskii, L. M.; et al. Equilibrium Acidities of Superacids. *J. Org. Chem.* **2011**, *76*, 391–395.

(31) Raamat, E.; Kaupmees, K.; Ovsjannikov, G.; Trummal, A.; Kütt, A.; Saame, J.; Koppel, I.; Kaljurand, I.; Lipping, L.; Rodima, T.; et al. Acidities of Strong Neutral Brønsted Acids in Different Media. *J. Phys. Org. Chem.* **2012**, *26*, 162–170.

(32) Gutowski, K. E.; Dixon, D. A. Ab Initio Prediction of the Gas- and Solution-Phase Acidities of Strong Brønsted Acids: the Calculation of pKa Values Less Than −10. *J. Phys. Chem. A* **2006,** 12044-12054.

(33) Zhang, M.; Sonoda, T.; Mishima, M.; Honda, T.; Leito, I.; Koppel, I. A.; Bonrath, W.; Netscher, T. Gas-Phase Acidity of Bis[(Perfluoroalkyl)Sulfonyl]Imides. Effects of the Perfluoroalkyl Group on the Acidity. *J. Phys. Org. Chem.* **2014**, *27*, 676–679.

(34) Zheng, A.; Liu, S.-B.; Deng, F. Acidity Characterization of Heterogeneous Catalysts by Solid-State NMR Spectroscopy Using Probe Molecules. *Solid-State Nucl. Magn. Reson.* **2013**, *55-56*, 12–27.

(35) Yi, D.; Zhang, H.; Deng, Z. 1H and 15N Chemical Shifts of Adsorbed Acetonitrile as Measures to Probe the Brønsted Acid Strength of Solid Acids: a DFT Study. *Journal of Molecular Catalysis A: Chemical* **2010**.

(36) Chen, T.-H.; Wouters, B. H.; Grobet, P. J. Enhanced Resolution of Aluminum and Proton Sites in the Molecular Sieve SAPO-37 by 27Al Multiple Quantum Magic Angle Spinning and 1H Spin Echo Editing NMR. *J. Phys. Chem. B* **1999**, *103*, 6179–6184.

(37) Ross, B. D.; True, N. S. Gas-Phase Carbon-13 NMR Spectra and Exchange Kinetics of N,N-Dimethylformamide - Journal of the American Chemical Society (ACS Publications). *J. Am. Chem. Soc.* **1984**.

(38) Angell, C. A.; Byrne, N.; Belieres, J.-P. Parallel Developments in Aprotic and Protic Ionic Liquids: Physical Chemistry and Applications. *Acc. Chem. Res.* **2007**, *40*, 1228–1236.

(39) Burrell, G. L.; Burgar, I. M.; Gong, Q.; Dunlop, N. F.; Separovic, F. NMR Relaxation and Self-Diffusion Study at High and Low Magnetic Fields of Ionic Association in Protic Ionic Liquids. *J. Phys. Chem. B* **2010**, *114*, 11436–11443.

(40) Tanner, J. E. Pulsed Field Gradients for NMR Spin-Echo Diffusion Measurements. *Rev. Sci. Instrum.* **1965**, *36*, 1086–1087.

(41) Stejskal, E. O.; Tanner, J. E. Browse - Journal of Chemical Physics. *J. Chem. Phys.* **1965**, *42*, 288–292.

(42) Tanner, J. E.; Stejskal, E. O. Restricted Self‐Diffusion of Protons in Colloidal Systems by the Pulsed‐Gradient, Spin‐Echo Method | Browse - Journal of Chemical Physics. *J. Chem. Phys.* **1968**, *49*, 1768–1777.

(43) Ueno, K.; Tokuda, H.; Watanabe, M. Ionicity in Ionic Liquids: Correlation with Ionic Structure and Physicochemical Properties. *Phys. Chem. Chem. Phys.* **2010**, *12*, 1649.

(44) Berne, B.; Rice, S. A. On the Kinetic Theory of Dense Fluids. XVI. The Ideal Ionic melt. *J. Chem. Phys.* **1964,** *40,* 1347-1362.

(1) Krishnan, V. V. Determination of Oligomeric State of Proteins in Solution From Pulsed-Field-Gradient Self-Diffusion Coefficient Measurements. a Comparison of Experimental, Theoretical, and Hard-Sphere Approximated Values. *J. Magn. Reson.* **1997**, *124*, 468–473.

(2) Chen, A.; Wu, D.; Johnson, C. S. Determination of Molecular Weight Distributions for Polymers by Diffusion-Ordered NMR. *J. Am. Chem. Soc.* **1995**, *117*, 7965–7970.

(3) Li, W.; Kagan, G.; Hopson, R.; Williard, P. G. Measurement of Solution Viscosity via Diffusion-Ordered NMR Spectroscopy (DOSY). *J. Chem. Educ.* **2011**, *88*, 1331–1335.

(4) Tanner, J. E. Pulsed Field Gradients for NMR Spin-Echo Diffusion Measurements. *Rev. Sci. Instrum.* **1965**, *36*, 1086–1087.

(5) Tanner, J. E.; Stejskal, E. O. Restricted Self‐Diffusion of Protons in Colloidal Systems by the Pulsed‐Gradient, Spin‐Echo Method | Browse - Journal of Chemical Physics. *J. Chem. Phys.* **1968**, *49*, 1768–1777.

(6) Kuchel, P. W.; Pagès, G.; Nagashima, K.; Velan, S.; Vijayaragavan, V.; Nagarajan, V.; Chuang, K. H. Stejskal-Tanner Equation Derived in Full. *Concepts Magn. Reson.* **2012**, *40A*, 205–214.

(7) Wu, D. H.; Chen, A. D.; Johnson, C. S. An Improved Diffusion-Ordered Spectroscopy Experiment Incorporating Bipolar-Gradient Pulses. *J. Magn. Reson., Ser A* **1995**, *115*, 260–264.

(8) Adcock, S. A.; McCammon, J. A. Molecular Dynamics: Survey of Methods for Simulating the Activity of Proteins. *Chem. Rev.* **2006**, *106*, 1589–1615.

(9) Wang, J.; Wolf, R. M.; Caldwell, J. W.; Kollman, P. A.; Case, D. A. Development and Testing of a General Amber Force Field. *J Comput Chem* **2004**, *25*, 1157–1174.

(10) Verlet, L. Computer "Experiments" on Classical Fluids. I. Thermodynamical Properties of Lennard-Jones Molecules. *Phys. Rev.* **1967**, *159*, 99–103.

(11) Swope, W. C.; Anderson, H. C.; Berens, P. H.; Wilson, K. R. A Computer Simulation Method for the Calculation of Equilibrium Constants for the Formation of Physical Clusters of Molecules: Application to Small Water Clusters. *J. Chem. Phys.* **1982**, *76*, 637–649.

(12) Wang, J.; Hou, T. Application of Molecular Dynamics Simulations in Molecular Property Prediction II: Diffusion Coefficient. *J Comput Chem* **2011**, *32*, 3505–3519.

(13) Holz, M.; Weingartner, H. Calibration in Accurate Spin-Echo Self-Diffusion Measurements Using 1 H and Less-Common Nuclei. *J. Magn. Reson.* **1991**, *92*, 115–125.

(14) Phillips, J. C.; Braun, R.; Wang, W.; Gumbart, J.; Tajkhorshid, E.; Villa, E.; Chipot, C.; Skeel, R. D.; Kalé, L.; Schulten, K. Scalable Molecular Dynamics with NAMD. *J Comput Chem* **2005**, *26*, 1781–1802.

(15) Humphrey, W.; Dalke, A.; Schulten, K. VMD: Visual Molecular Dynamics. *J Mol Graph* **1996**, *14*, 33–38.

(16) Jorgensen, W. L.; Chandrasekhar, J.; Madura, J. D.; Impey, R. W.; Klein, M. L. Comparison of Simple Potential Functions for Simulating Liquid Water. *J. Chem. Phys.* **1983**, *79*, 926.

(17) Uberuaga, B. P.; Anghel, M.; Voter, A. F. Synchronization of Trajectories in Canonical Molecular-Dynamics Simulations: Observation, Explanation, and Exploitation. *J. Chem. Phys.* **2004**, *120*, 6363–6374.

(18) Feller, S. E.; Zhang, Y.; Pastor, R. W.; Brooks, B. R. Constant Pressure Molecular Dynamics Simulation: the Langevin Piston Method. *J. Chem. Phys.* **1995**, *103*, 4613–4621.

(19) Vanommeslaeghe, K.; Hatcher, E.; Acharya, C.; Kundu, S.; Zhong, S.; Shim, J.; Darian, E.; Guvench, O.; Lopes, P.; Vorobyov, I.; et al. CHARMM General Force Field: a Force Field for Drug-Like Molecules Compatible with the CHARMM All-Atom Additive Biological Force Fields. *J Comput Chem* **2010**, *31*, 671–690.

(20) Yu, W.; He, X.; Vanommeslaeghe, K.; MacKerell, A. D. Extension of the CHARMM General Force Field to Sulfonyl-Containing Compounds and Its Utility in Biomolecular Simulations. *J Comput Chem* **2012**, *33*, 2451–2468.